CRANFIELD UNIVERSITY

Sulei Chen

Robotic polishing of large optical components

MSc Thesis

MSc by Research

Academic year: 2013 - 2014

Supervisors: Dr Xavier Tonnellier

Dr Paul Comley

August 2014

CRANFIELD UNIVERSITY

MSc by Research Thesis

Academic Year: 2013 - 2014

Sulei Chen

Robotic polishing of large optical components

Supervisors: Dr Xavier Tonnellier

Dr Paul Comley

August 2014

ABSTRACT

Lightweight space mirrors have been widely used in earth observation and astronomy applications. Many organizations and companies, such as NASA in America, ESA in Europe, SSTL in UK as well as CASC in China, have spent a lot of money and effort on researching new materials for larger size space mirrors to meet both the payload weight constraints of launch and the increased advanced manufacturing process demanded for higher observations quality.

This project is aimed at robot neutral polishing of lapped, ground and polished optical substrates using an industrial FANUC robot system. The project focused on three main fields which were: robot polishing with polyurethane tool and cerium oxide, pitch polishing with pitch tool and cerium oxide, as well as polishing of a 400mm ULE component. The polishing process targets were to achieve: 1) a surface roughness (R_a) of 10 nm and a surface profile (P_t) of 6 μm and 2 μm on lapped and ground substrates respectively with polyurethane based tools and 2) a surface roughness (R_a) of 2nm with a surface profile (P_t) unchanged on robot neutral polished substrates using pitch based tools.

This thesis comprises four main sections: a literature review, an experimental implementation, metrology and analysis, and the final conclusions. The experiment results measured with the metrology equipment selected were analysed. Conclusions of the relationship between the polishing performance of a specific sample and the selected polishing tool, polishing slurry, tool pressure, polishing time and other parameters were drawn.

Results obtained from robot neutral polishing were surface roughness (R_a) of 8-10nm and surface profile (P_t) of 6 μm for 100mm square lapped and ground parts. The process scalability was demonstrated from robot neutral polishing in 45 hours, a 400mm square ground component from a surface roughness (R_a) of 200nm to 10nm.

There is additional work to be implemented in the future, such as the development of robot pitch polishing of robot neutral polished parts to achieve 2nm R_a.

Key words: polyurethane polishing, ULE, fused silica, pitch, spot, groove, cerium oxide

ACKNOWLEDGEMENTS

I would like to express my gratitude to my supervisor, Dr Xavier Tonnellier, for his guidance during the whole year which makes the project possible.

Then special thanks to Mr John Hedge, a technician retired in June 2014, who helped me a lot solve the problems occurred during making the polishing tools and tool moulds and Mr Alan Heaume who taught me how to use the metrology equipment which started the beginning of the project.

I would also like to thank my subject advisor Professor Paul Shore and my associate supervisor Dr Paul Comley for their instructions of the project.

I am very grateful to all the technical staff of the Precision Engineering Institute for their help during the whole project.

I would also express my thanks to my company, COMAC, for giving the opportunity to study in Cranfield University for advanced manufacturing technology and learn different culture. Special thanks also go to the COMAC students for spending the whole year here together and we are just like a family.

Finally, I would like to thank my parents Yuhua Chen and Guanglan Shu, for the education of my whole life. My deepest gratitude goes to my deeply loved girl, Qianru Li, for her support, attention and encouragement every day which inspired me to complete the project perfectly and quickly.

TABLE OF CONTENTS

LIST OF FIGURES

LIST OF TABLES

LIST OF EQUATIONS

NOTATIONS

C_p	[J/kg/K]	Specific Heat Capacity
D	[$10^{-6}m^2/s$]	Thermal Diffusivity
D_c	[mm]	Depth of the cross section
D_f	[μm]	Removed depth
E	[Gpa]	Young's Modulus
E/ρ	[10^9Nm/kg]	Specific Stiffness
E_0	[μm]	Accuracy
f	[mm]	Feed rate
k	[W/m/K]	Thermal Conductivity
K_e	[mm^2/N]	All-purpose coefficient
K_{poly}	[m^2/N]	All-purpose coefficient of Polyurethane
L	[mm]	Length of the polishing area
L_s	[mm]	Length of the groove
MRR	[mm/s]	Material removal rate
MRR_1	[mm^3/s]	Material removal rate
MRR_{1f}	[mm^3/s]	Material removal rate of fused silica
MRR_{1U}	[mm^3/s]	Material removal rate of ULE
N_{runs}	[-]	Number of runs
P	[N/mm^2]	Downward pressure
P_t	[μm]	Surface profile – Peak to Valley
R	[mm]	Radius of polishing tool
R_a	[nm]	Arithmetic surface Roughness
S_c	[mm^2]	Size of cross section
S_f	[mm^2]	Size of the fused silica sample
S_p	[mm]	Polishing step
T_1	[h]	Polishing time of one run
t	[s]	Polishing time per run
t_f	[s]	Time of polishing fused silica
V	[mm/s]	Velocity over the workpiece surface
V_f	[mm^3]	Volume of removed fused silica
v	[-]	Poisson's Ratio
V_p	[mm/s]	Polishing speed
W	[mm]	Width of the polishing area
W_c	[mm]	Width of the cross section
α	[$10^{-6}K^{-1}$]	CTE
α/D	[$s/K/m^2$]	Transient Distortion

α/k	$[10^{-6}m/w]$	Steady State Distortion
ρ	$[kg/m^3]$	Density

ABBREVIATIONS

BoX	Big OptiX
CASC	China Aerospace Science and Technology Corporation
CCL	Computer Controlled Lapping
CCOS	Computer Controlled Optical Surfacing
CCP	Computer Controlled Polishing
CMM	Co-ordinate Measuring Machine
CMP	Chemical Mechanical Polishing
CNC	Computer Numerically Controlled
CNSA	China National Space Administration
CTE	Coefficient of Thermal Expansion
CVC	Chemical Vapor Composite
CVD	Chemical-Vapor-Deposited
EEM	Elastic Emission Machining
ELT	Extremely Large Telescope
ESA	European Space Agency
FWHM	Full Width Half Maximum
GMT	Giant Magellan Telescope
GPS	Global Positioning Satellites
IBF	Ion Beam Figuring
LVDT	Linear Variable Differential Transformer
MR	Magneto-Rheological
MRF	Magneto-Rheological Finishing
MRR	Material Removal Rate
NASA	National Aeronautics and Space Administration
NC	Numerically Controlled
NIF	National Ignition Facility
OCT	Opto tech Correction Technology
RAPT	Reactive Atom Plasma Technology
RMS	Root Mean Square
SiC	Silicon Carbide
SMP	Stressed Mirror Polishing
SSD	Sub-Surface Damage
SSiC	Sintered Silicon Carbide
SSTC	Surrey Satellite Technology Ltd
TIF	Tool Influence Function
ULE	Ultra-Low Expansion
VLT	Very Large Telescope

1. Introduction

1.1 Lightweight space mirrors

Lightweight space mirrors were initially applied in military parts, for example the Global Positioning Satellites (GPS), to provide the armed force with precise position information. With the development of science technology, lightweight space mirrors are used in both military and civil purposes recently for the functions of weather forecast, navigation, communications, earth observation and astronomy.

Large, lightweight and high precision mirrors are also required and critical for the application of astronomical telescopes, such as the well-known Hubble Space Telescope. The telescope observes much farther with a larger size in diameter and more precise with higher precision. The mirror would be much heavier when the size increases aimed at the given material which makes it more difficult to launch into the space. The payload of space shuttle to the geostationary transfer orbit is limited up to 3,810kg. To meet the payload weight constraints of launch, the mirror had to be very lightweight.

Therefore, many space agencies, for example NASA (National Aeronautics and Space Administration), ESA (European Space Agency) as well as CNSA (China National Space Administration), and a large number of companies, such as L-3, SSTL (Surrey Satellite Technology Ltd) as well as CASC (China Aerospace Science and Technology Corporation), have invested much time and capital in new materials and processes of lightweight space mirrors. US government agencies have designed equipment for airborne and space-based systems which will require mirrors ranging in size from 0.1 to 100 meters in diameter. Moreover, the budget of astrophysics at NASA will reach 642 million dollars in 2014 (Budget Estimates, FY2014).

The traditional materials and processes include monolithic glass mirror and metallic mirror. The new materials and processes, such as lightweight glass and silicon carbide-based mirrors, help increase the size of the mirror as well as reduce the real density compared with traditional materials. There are other new approaches that are being considered for developing space mirror, such as mirrors constructed from foams and composite mirrors (Matson and Mollenhauer, 2003).

1.2 Manufacturing process chain

Geyl and Cayrel, (1999) from Sagem and Pileri and Krabbendam, (1995) from Kodak reported similar manufacturing processes of large mirrors. Both of their approaches were composed of the following steps: the shaping process, the grinding process, the lapping process, the polishing process and the final ion beam figuring process.

The blank piece, whose substrate material is glass or ceramic, is shaped to a flat or a curved shape. Then a grinding machine is used to manufacture the workpiece to the required shape. Moreover, the workpiece is lapped and polished to obtain the right dimension and to eliminate the subsurface damage occurred during the earlier manufacturing process. Finally, a final figuring step, such as magneto-rheological finishing (MRF) or ion beam figuring (IBF) is used to manufacture the workpiece to desired accuracy (Tonnellier , 2009).

The general process chain proposed using Cranfield technologies for manufacturing lightweight space structures is shown in Figure 1.

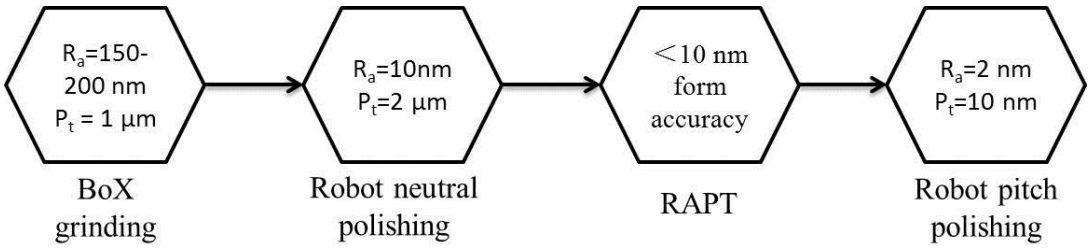

Figure 1: Process chain of manufacturing lightweight space mirror (Tonnellier et al., 2013)

First, the optical components are manufactured by the Big OptiX (BoX) grinding process which is a high precision grinding with less sub-surface damage (SSD). Then robot neutral polishing is employed to enable figure correction using Reactive Atom Plasma (RAP) efficient processing. Final, robot pitch polishing is used to obtain better surface roughness.

1.3 Overview of polishing technologies

There have been many types of polishing technologies designed depending on the mechanism of polishing process. Jairath et al., (1987) introduced that Chemical mechanical polishing (CMP) was developed as the preferred technique for meeting the global planarity requirements for sub-half micron technology. Lubliner and Nelson, (1980) presented an ultra-precision polishing method, Stressed Mirror Polishing (SMP), which applies stresses to a mirror blank to elastically deform it from a desired surface into a sphere. Sub-aperture polishing techniques, including Magneto-Rheological Finishing, Precession and other techniques, are introduced in detail in section 1.3.2 to section 1.3.4.
The mechanism of polishing process involves four components: the workpiece, the fluid, the granule, and the lap. The component itself and the interaction of the components both have an influence over the final polishing result of the workpiece. For the fluid, its physical properties, including viscosity, density and temperature conductivity, affect both fluid dynamics and material transport in polishing; while for the solid granule, its average size and size distribution have an influence of the surface quality of the polished workpiece. The interaction of fluid and granule during which the fluid pH changes the surface of granule affects the surface quality of the polished workpiece (Evans et al., 2003).

1.3.1 Preston's equation

Preston's equation (see 1.3.1.1) was initially presented for glass polishing to describe material remove after polishing process.

$$MRR=K_e P V \quad (1.3.1.1)$$

Where MRR (mm/s) is the material removal rate, K_e (mm^2/N) is an all-purpose coefficient, P (N/mm^2) is the downward pressure and V (mm/s) is the relative velocity over the workpiece surface. The equation demonstrates a linear reliance of material removal rate on the pressure and velocity (Luo, 2003).

1.3.2 Magneto-Rheological Finishing

Arrasmith et al., (1999) in University of Rochester designed a new platform of polishing spots on different optical substrates in Magneto-Rheological Finishing (MRF) which exploited a magnetic field-stiffened Magneto-Rheological (MR) fluid ribbon to create a sub-aperture lap used to manufacture on optical surface.
Evans et al., (2003) employed the MRF technology whose function is shown in Figure 2.

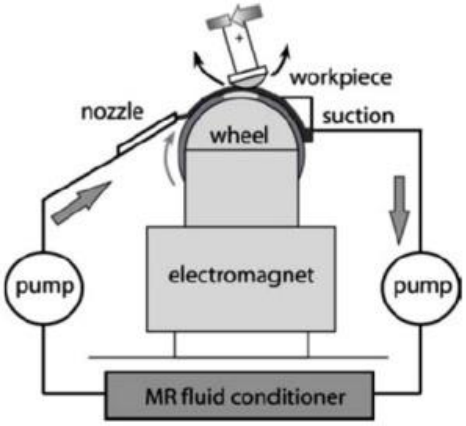

Figure 2: MRF machine schematic (Evans et al., 2003)

MRF utilizes the characteristic of MR fluids to change its stickiness taking advantage of magnetic function. The MR fluid which is comprised of deionized water, iron particles, abrasives and stabilizing agents is unceasingly kept flowing between the pumps, transforming between its solid phase where the electro-magnet affects and liquid phase everywhere else. The magneto-rheological polishing fluid is employed on the edge of a rotating wheel, which conveys the fluid to the polishing area. The workpiece to be polished is grasped in the computer-numerically controlled (CNC) machine, and immersed into the ribbon of fluid. The amount of material to be removed at a given area depends on the dwell time which is similarly to other computer controlled polishing methods.

1.3.3 Precession process

The precession process has been created to control the texture and preserve the form during polishing on flat, spherical and aspheric surfaces. Tooling for the precession process is shown in Figure 3.

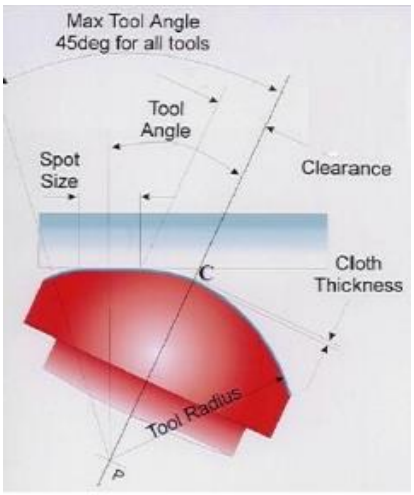

Figure 3: Precessing bonnet (Walker et al., 2003)

The tool is a bonnet which is an inflated rubber membrane of spherical form covered with a non-pitch flexible polishing surface. The membrane has the property that the polishing pressure (tool hardness) and the contact area (polishing spot size) can be changed independently by altering the internal pressure of working fluid and the axial position of the tool. A static pole-down spinning tool displays zero surface-speed at centre, rising linearly to a maximum at the periphery. The tool spins about its axis to increase surface speed and to attain a high volumetric removal rate. The tool-axis is precessed in discrete steps about the local normal to the surface of the part. The influence functions are near-Gaussian, effectively edgeless with no sharp discontinuities. The precession process is a combination of classical polishing and CNC diamond grinding which unites the flexibility of the former and the determinism of the later (Walker et al., 2003).

1.3.4 Other sub-aperture polishing techniques

Seifert (2007) from Carl Zeiss Laser Gmbh introduced a principle process chain for aspheres. The process chain starts with Computer Controlled Lapping (CCL) of aspherical surfaces with small sub-aperture tools followed by using 6-axes Computer Controlled Polishing (CCP) technology, then followed by the Ion Beam Figuring (IBF) technology to achieve a high performance.

SPK 150 CNC-HPP, a machine provided by the Opto tech Correction Technology (OCT) whose important advantage is the direct correction of the polishing tool by means of the measured surface irregularity of the workpiece, applies to spherical polishing for optics up to Ø 150mm (Opto Tech).

The robotic polishing technique, a sub-aperture polishing method and one step of the manufacturing chain: aspheric grinding followed by polishing robot followed by RAP figuring, has been applied in Cranfield University (Tonnellier et al., 2013).

1.4 Aim and objectives

This project is aimed at robot neutral polishing of lapped and ground substrates, and the improvement of the final surface roughness using pitch polishing, both using an industrial FANUC robot system. Together, these processes will promote the use of RAP as an efficient energy beam processes tool.

The process objectives of this project were:
1) To achieve, by robot neutral polishing, a surface roughness (R_a) of 10nm and profile (P_t) of 6µm on lapped optical glasses (ULE and fused silica). Figure 4 demonstrates how this relates to the Cranfield manufacturing process chain described in Figure 1.

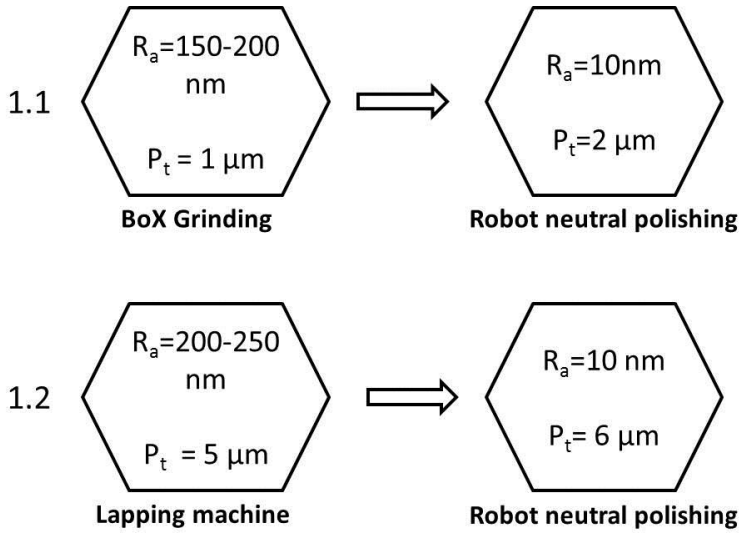

Figure 4: Objective 1 of the project

From BoX grinding to Robot neutral polishing, it was anticipated that the surface profile degrades from 1µm to 2µm (P_t) and the surface roughness improves by a factor of 15-20 from 150-200nm to 10nm (R_a) (see Objective 1.1). Considering the robot neutral polishing performance, for a lapped sample, the surface profile (P_t) and the surface roughness (R_a) that were considered achievable, were 6µm and 10nm respectively (see Objective 1.2). The polishing process has been verified on two materials ULE and fused silica. Up-scaling of the process has also been demonstrated on a 400mm square ULE substrate.

2) To achieve, using robot pitch polishing, a form accuracy < 6µm P_t and surface roughness < 2nm R_a on ULE, see Figure 5.

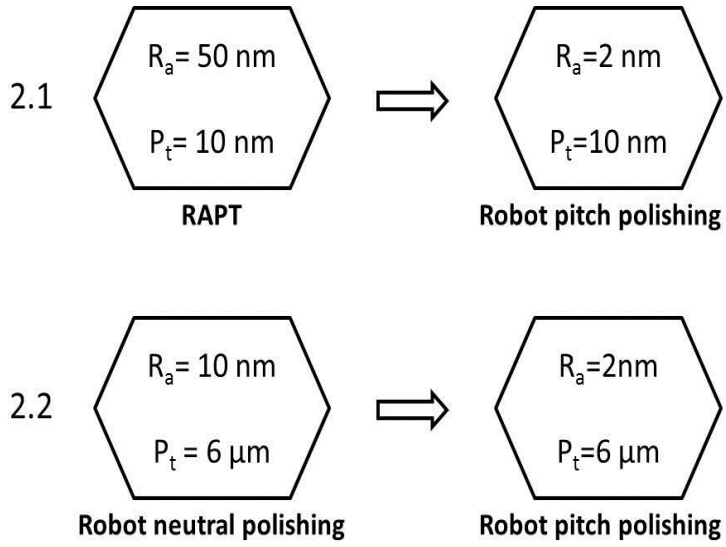

Figure 5: Objective 2 of the project

Objective 2.1 illustrates that after RAP processing, which degraded the surface roughness, the robot pitch polishing improves R_a to 2nm with a surface profile (P_t) unchanged. It can be inferred that, after robot pitch polishing a robot neutral polished sample, the surface roughness achieved should be 2nm R_a with an unchanged surface profile (see Objective 2.2). These samples were assessed to show that limited form accuracy degradation was observed.

1.5 Methodology

The methodology of this project comprises four phases: a literature review, experimental implementation, metrology and analysis, and conclusion (see Figure 6).

Papers related to this subject have been read to understand the background and master relevant knowledge during the literature review phase. The parameters, which affect the polished surface quality, have been studied, such as the substrate material, the polishing tool, the polishing spot, the polishing slurry, the robot processing and the metrology equipment. The factors during the polishing process, such as the polishing pressure and the dwell time, have also been reviewed. Moreover, the robot based polishing platform, which is comprised of robot arm, air spindle, slurry pump, polishing tray and control software, has be employed in robot neutral polishing and robot pitch polishing.

Implement experiment and metrology phases are explained in Chapter 3 (Metrology equipment and Experiment procedures) and Chapter 4 (Experiment Results). The final phase, analysis and conclusion, is to analyse the experiment results and identify further work to be carried out which are explained in Chapter 5 to Chapter 7.

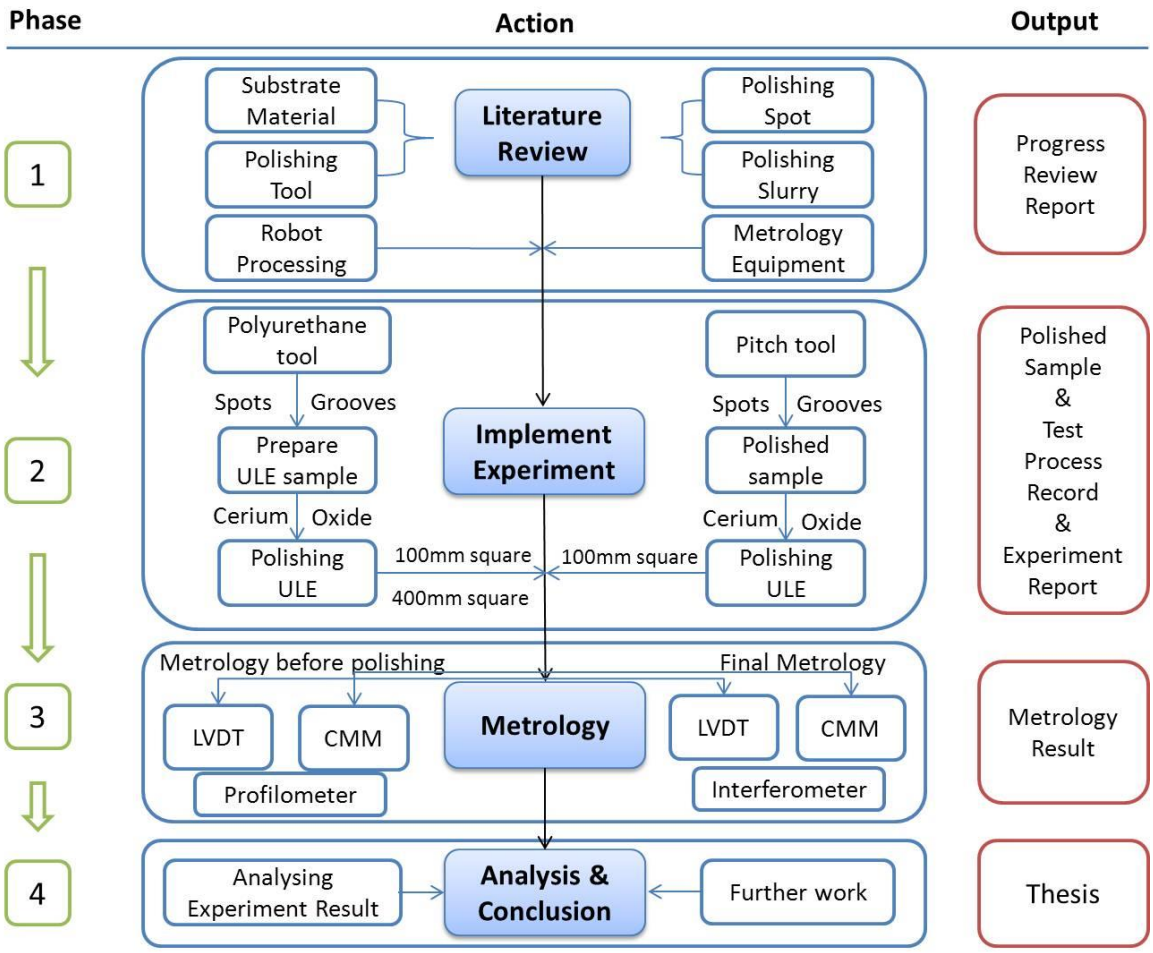

Figure 6: Methodology of the project

2. Literature review

2.1 Substrate Materials

There are four main kinds of substrate materials for optical applications. These include metals and their alloys, ceramics, glasses and semiconductors, which are manufactured to a required geometry, finish, accuracy, and surface integrity to fulfil their service requirements.

The non-metals substrates have the following characteristic: covalent (directional), or ionic bonding, low symmetry, limited or inadequate slip systems for plastic deformation, low thermal conductivity, and low fracture toughness and low breaking energy (Komanduri et al., 1997).

Carl Steinheil and Leon Foucault designed small silvered-glass telescope mirrors in the late 1850s which started the beginning research of metallised-glass reflecting telescopes (Tobin, 1987). Fabbrizzi and Mariani, (1986) introduced lightweight metal mirror for the Giotto Multicolour Camera. Hoeness et al., (1988) introduced lightweight mirror substrates manufactured from the glass ceramic Zerodur; Zhou et al., (2006) presented high precision lightweight optical application using Carbon-fiber reinforced silicon carbide (C/SiC);

Table 1: Material properties of various optical substrates
(Tsuno et al., 2005, Hobbs et al., 2003, Goela et al., 1995)

Material property	**Units**	**Fused Silica (Corning)**	**ULE**	**Zerodur (Typical)**	**SiC (Typical)**
Density (ρ)	kg/m^3	2200	2200	2530	3100
Young's Modulus (E)	GPa	73	67	91	420
Poisson's Ratio (v)	-	0.16	0.17	0.24	0.25
Ultimate Tensile Strength	MPa	-	-	57	400
CTE (α)	$10^{-6}K^{-1}$	0.52	0.03	0.10	2.2
Specific Heat Capacity (C_p)	J/kg/K	741	778	820	680
Thermal Conductivity (k)	W/m/K	1.3	1.3	3.5	140
Specific Stiffness (E/ρ)	10^9Nm/kg	0.034	0.030	0.036	0.135
Thermal Diffusivity (D=k/Cp/ρ)	$10^{-6}m^2/s$	0.75	0.8	0.8	66.4
Steady State Distortion (α/k)	10^{-6}m/w	0.038	0.023	0.028	0.016
Transient Distortion (α/D)	$s/K/m^2$	0.067	0.039	0.063	0.033

2.1.1 Glass

Fused silica, an isotropic glass substrate, is stable in dimension and capable of being finished to an extreme smooth surface with low coefficient of thermal expansion, low density and high stiffness. Table 1 shows the key properties of fused silica which is manufactured by Corning Incorporated (Hobbs et al., 2003).

Fused silica is one kind of high frequently used optical glasses in the National Ignition Facility (NIF). There are two various grades of fused silica on the NIF: one grade is

manufactured through a more typical CVD deposition process and the other improved grade is made free of re-fractory inclusions, with high optical homogeneity and in large sizes which is bigger than 400mm square. The NIF is one of the largest optical systems in the world using 7500 precision optics which included 960 fused silica aspheric lenses and other substrates (Moses et al., 2003).
Martin et al., (2006) introduced the manufacturing of 8.4m primary mirror segments for the Giant Magellan Telescope (GMT) using borosilicate glass.

2.1.2 Glass-Ceramics

Ultra-low expansion (ULE) glass has been manufactured by Corning Incorporated since the 1960's. The glass is primarily applied in telescope mirrors, for example the well-known Hubble space telescope whose maximum diameter is 4.2 meter. The low expansion characteristic helps these large mirrors to minimize distortions in the images causing by thermal changes. The main properties of ULE are summarized in Table 1.
It is defined as having a coefficient of thermal expansion (CTE) of 0±30ppb/℃ over the temperature range of 5 to 35℃. To provide perspective, this is more than an order of magnitude smaller than the coefficient of thermal expansion of fused silica, which is traditionally considered to have a small expansion (Hrdina, 1999).
Zerodur, a glass ceramic, has a good performance on primary mirrors and lightweight mirrors for its high homogeneity properties, such as extremely low CTE values and good thermal stability (see Table 1). The production of lightweight Zerodur mirror blanks is comprised of the following steps: first, direct casting of blanks followed by low temperature fusion of glassy Zerodur; then using CNC grinding to remove weight of blanks; the final step is CNC grinding and additional acid lightening (Morian and Mackh, 1998). Dierickx et al., (1990) introduced the 8.2 meter primary mirrors of the Very Large Telescope (VLT) made of Zerodur.

2.1.3 Ceramics

Silicon Carbide (SiC) is a ceramic which is a contamination free material for silicon semiconductor process and its high stability in high temperature. It is is widely used in manufacturing semiconductor equipment parts. SiC has been used as space optical substrate material in recent years owing to its remarkable property, high stiffness, high thermal conductivity, very hard and high melting point (see Table 1). In space environment, thermal stability is extreme important for optical equipment, since the thermal control of optical equipment is one of the major issues during the extreme large thermal change situation.
In addition, high specific stiffness means that the mirror could be thinner and have more precise surface figure with higher stiffness (Goela et al., 1995) making SiC a good candidate in space optical mirror application (Tsuno et al., 2005).
According to Export Regulations of International Traffic in Arms (2006), as a substrate of electronic components and deposited materials, SiC is in the list of controlled items. The companies and organizations in every country have to carry out projects of manufacturing their own large size silicon carbide substrate. The company Coorstek Optical Ceramics in America has produced SiC materials suitable for mirrors for space-based optical systems, such as UltraSiC^{TM} Single Phase Silicon Carbide (Coorstek, 2012). ECM, a company in

Germany, has developed carbon-fiber reinforced silicon carbide for GREGOR telescope (Krödel et al., 2006). Zhang et al., (2013) in Harbin Institute of Technology developed a new non-aqueous gelcasting system for casting of reaction bonded silicon carbide ceramics.

Boostec SiC material is a Sintered Silicon Carbide (SSiC) which is previously known as "SiC-100". The main key properties of "SiC-100" are the high specific stiffness and high thermal stability which make it suitable for space optics. Sein et al., (2003) presented the development of the Φ 3.5m telescope fabricated by SiC for Herschel Mission.

Chemical-vapor-deposited (CVD) SiC is notionally dense, polycrystalline material which is free from voids and micro-cracks, resulting in a substrate with superior properties for mirror application. Due to the porosity of SSiC, a thin layer of CVD SiC is deposited on substrate before final polishing. This CVD SiC has the highest values of elastic modulus, thermal distortion parameter and thermal stress parameter which makes it a good material for optics applications (Goela et al., 1995).Table 2 shows the comparison of CVD SiC with other mirror substrates.

Table 2: Comparison of CVD SiC with other mirror substrates
(Goela et al., 1995, Boostec industries, 2012, Goodman and Tanaka, 2009)

Material Property	CVD SiC	SiC-100 Boostec	Trex CVC SiC
Density, ρ (kg/m^3)	3210	3150	3200
Coefficient of thermal expansion ($10^{-6}K^{-1}$)	2.2	2.2	3.5
Specific heat, C (J /kg/K)	640	-	640
Thermal conductivity, k (W/m/K)	330	180	205-250
Elastic modulus, E (GPa)	466	420	466
Thermal distortion parameter, $k\alpha^{-1}$ ($W/m \times 10^7$)	15	8.2	-
Inertia loading parameter, $E\rho^{-1}$ ($10^9 Nm/kg$)	0.145	0.1333	-
Thermal stress parameter, $k\alpha^{-1}E^{-1}$ ($W\ m/N \times 10^{-4}$)	3.2	-	-
Poisson's Ratio	-	-	0.21

Trex Enterprises Corp. (Trex) improves the conventional CVD process to acquire its Chemical Vapor Composite SiC (CVC SiC). It has superior high temperature stability, thermal and mechanical performance and polish ability which is suitable for lightweight space and airborne telescopes, high energy laser optics and other critical optical systems (Goodman and Tanaka, 2009).

2.2 Robotic polishing technology

As mentioned in Chapter 1, various polishing technologies have been employed to produce large optical glass mirrors. These technologies are based on the similar polishing strategies and polishing motions which are introduced in this section.

2.2.1 Polishing strategies

Different kinds of process kinematics have been used for corresponding polishing methods which can be seen from Figure 7.

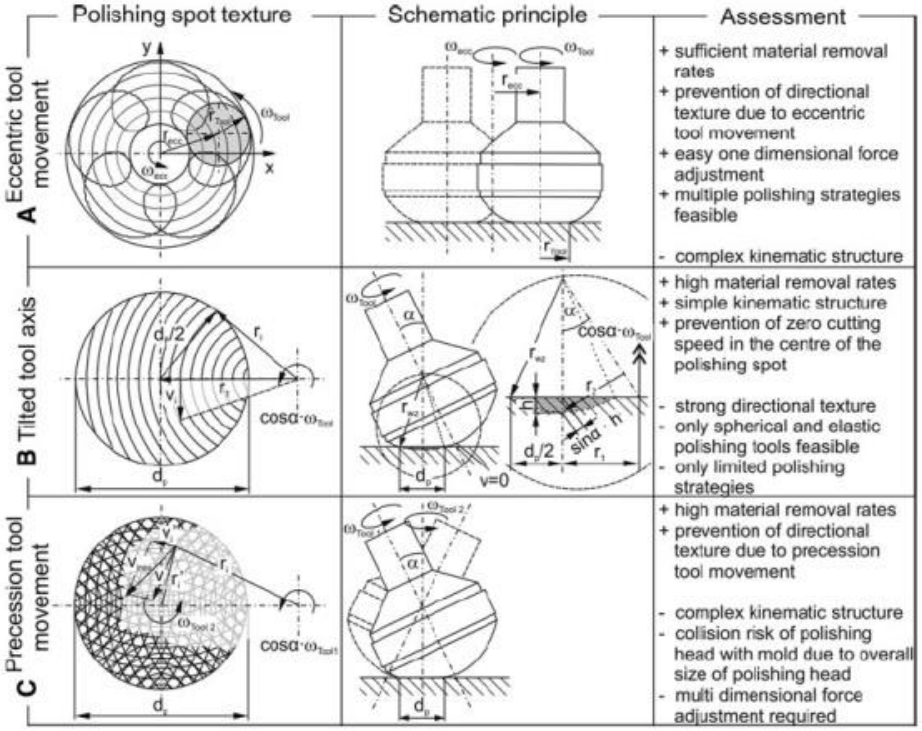

Figure 7: Different kinds of polishing process kinematics (Brecher et al., 2010)

The eccentric tool movement achieves a sufficient material removal rate and a texture free surface finish; The tilted tool axis obtains high material removal rates but strong directional textures on the surface; The precession tool movement provides the best performance which combines the high material removal rates of tilted tool movement and the texture free surface finish (Brecher et al., 2010).

2.2.2 Polishing motions

Polishing motions could be geometrically described as the tool path which is defined as a series of straight lines, curves and connecting bridges. The tool path commands the polishing tool motion along the sample surface exactly. Figure 8 shows different strategies for tool path.

The continuous raster path includes zigzag, staircase, sweep path and so on whose polishing tool travels back and forward across the sample surface with constant step size between paths. The polishing tool of the spiral path starts at the external edge of the sample and continues inwards towards the middle of the sample in spiral motion. The discontinuous raster path employs the polishing tool that moves in parallel direction for

each path along the sample surface and then moves back from the sample surface to the starting point across next path. The contour path produces a series of closed self-intersections tool path (Rososhansky and Xi, 2011).

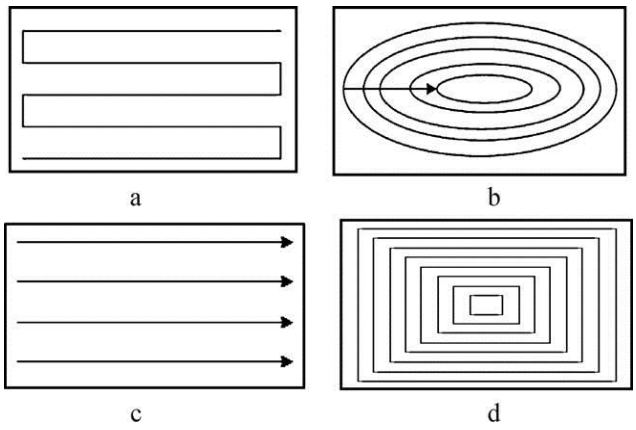

Figure 8: Tool path: a) Raster motion, b) Spiral motion, c) Discontinued raster motion and d) Contour path (Rososhansky and Xi, 2011)

Pseudo-random tool paths are developed for precession CNC polishing to eliminate the residual periodicities in a surface at the nano or sub-nano scale left by the typical paths.
The precessions process implements given polishing with the help of a dwell time map combined with a tool path. The velocity of the tool can be different along the path to generate the dwell time specified at each point on the dwell time map because the raster, spiral or random tool path never cross itself (Walker et al., 2008). Figure 9 shows the raster and random tool paths on a 35mm diameter circle.

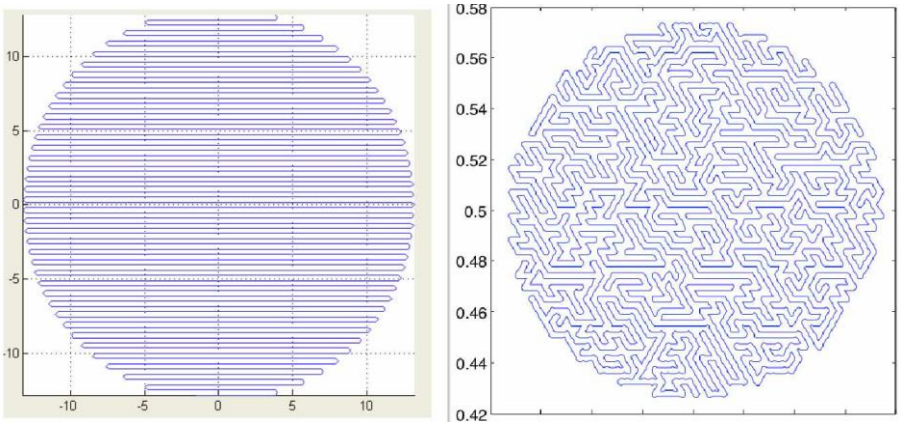

Figure 9: Raster and random tool paths on a 35mm diameter circle (Dunn and Walker, 2008)

2.2.3 Diamond turning cusp motion error

Franse (1990) introduced the function and equation of the groove's surface profile developed by diamond turning process which is shown in Figure 10 and Equation 2.2.3.1.

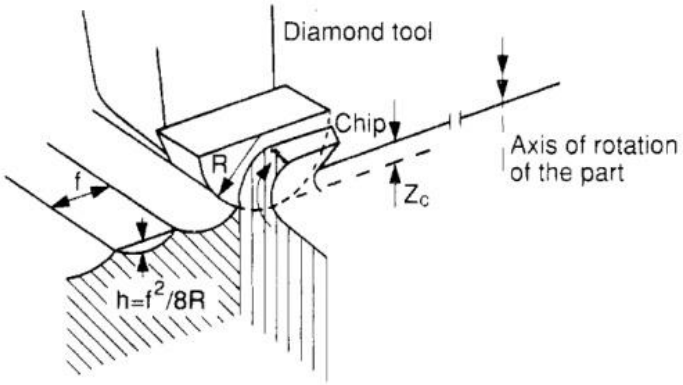

Figure 10: Surface profile of groove developed by precision-machining process (Franse, 1990)

$$P_t = f^2/8R \qquad \text{(Equation 2.2.3.1)}$$

Equation 2.2.3.1 shows the calculation of the surface profile (P_t), where f means the feed rate, R means the radius of manufacturing tool.

Franse (1990) also explained different grooves in diamond turning caused by various feed rate, overlap and vibrations which are shown in Figure 11.

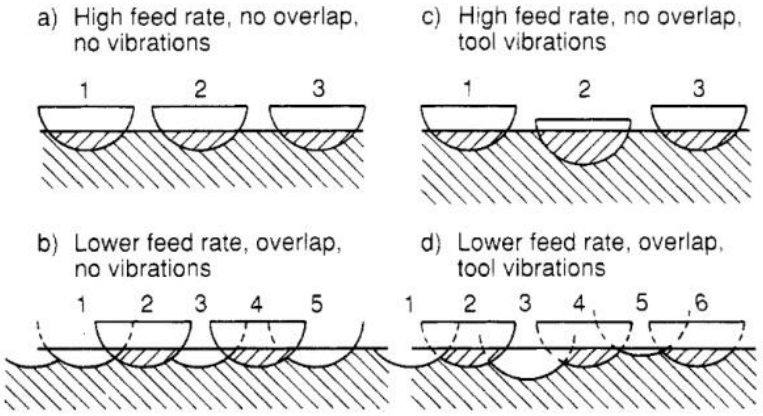

Figure 11: Surface profile - successive tool overlap (Franse, 1990)

On the BoX grinding machine, cusps on the part were generated by moving along the Y axis by the same amount of distance per revolution of the rotary table while the grinding spindle was titled at a fixed 20 degree (Tonnellier, 2009). Figure 12 shows the mode of BoX grinding machine used to prepare samples in this project.

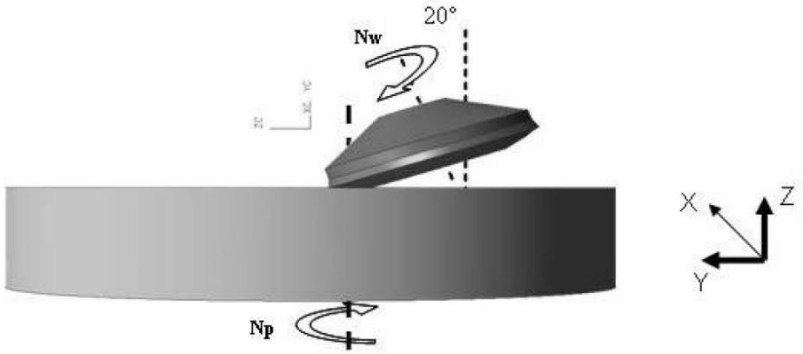

Figure 12: BoX grinding mode (Tonnellier, 2009)

2.3 Polishing tools

Various computer controlled optical surfacing (CCOS) processes have been created since the 1960s whose processes have three main components: a numerically controlled (NC) polishing machine, embedded process control intelligence and a polishing tool. The tool properties, such as pressure distribution, tool contact area shape and tool motion, affect the tool influence function since polishing tool contacts and removes materials from the workpiece directly.

2.3.1 Tool body structure

When developing a polishing tool, it has to consider both the flexibility which is required to maintain good contact with the workpiece surface and the rigidity by which to hit high portions with higher pressure on a rough surface. The schematic structures for different tool types are illustrated in Figure 13.

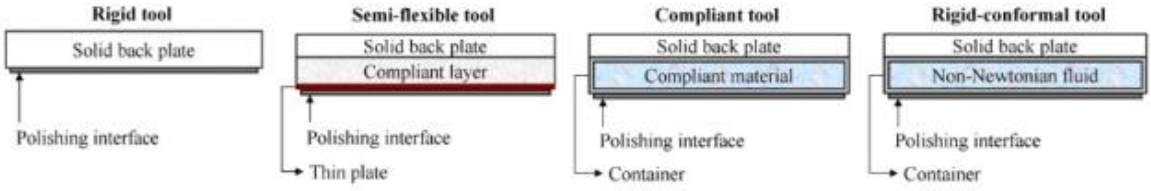

Figure 13: Schematic tool structures of four different tool types (Kim and Burge, 2010)

The rigid tools are usually constructed with a stiff material as a tool base structure covered with a polishing material, for example pith or polyurethane, as a polishing interface. The semi-flexible tool usually uses a relatively thin metal plate as a tool base covered with a polishing pad or pitch as a polishing interface. A foam layer maybe put between the thin plate and the solid thick plate. The complaint tool usually utilizes complaint materials, such as a liquid and air, which are often sealed in a container or make direct contact with the workpiece. The new rigid-flexible tool takes the advantages from both the rigid and complaint tool. It utilizes Non-Newtonian fluid which is often sealed in a container covered with a polishing interface (Kim and Burge, 2010).
Table 3 shows the general comparison between different tool types where the parameter with a superscript is usually regarded as advantage.

Table 3: General comparison between different tool types (Kim and Burge, 2010)

	Rigid tool	Semi-flexible tool	Compliant tool	Rigid conformal tool
Making large tool (e.g.＞30cm)	Easy[1]	Easy[1]	Difficult	Easy[1]
Cost (including a NC machine)	Inexpensive[1]	Medium	Expensive	Inexpensive[1]
A tool for different workpieces	No	Limited	Yes[1]	Yes[1]
Smoothing	Good[1]	Good[1]	Poor	Medium
Predictability	Low	Fair	Excellent[1]	Good[1]
Fitting to workpiece surface	Poor	Fair	Good[1]	Good[1]
Working on aspheric workpiece	Difficult	Good[1]	Easy[1]	Easy[1]
Working on freeform workpiece	Difficult	Hard	Easy[1]	Easy[1]
Working over the edge	Yes[1]	Yes[1]	No	Yes
Tool maintenance	Difficult	Easy[1]	Medium	Easy[1]

2.3.2 Polyurethane

Polyurethane is a material suitable for polishing optical parts as a result of the following reasons: First, the pores and asperities in its body and surface help to keep the slurry particle during polishing; Second, the high viscosity and relatively high soften temperature enable the high linear/angular speed; Final, the surface figure can keep quite a long time which can manufacture passels of optical parts with uniform surface form (Li et al., 2008). The polyurethane pad used in this project was LP-66 whose parameters are shown in Table 4 (Abrasifs Grains et Poudres, 2013).

Table 4: Parameters of polyurethane (Abrasifs Grains et Poudres, 2013)

Product Grade	Filler	Density (kg/m^3)	Hardness			Standard thicknesses	Standard dimensions
			Shore "A" Range	Durometer Aim	Shore "D" Range		
LP-66	Cerium Oxide	352.7-512.7	67-72	25	20-30	0.51mm; 1.27mm; 3.18mm; 6.35mm	580 mm x 1400mm
GR-35	Zirconium Oxide	561.1-673.1	85-93	35-40	33-43		

Kim and Burge, (2010) introduced the method of gluing the LP-66 polyurethane polishing pad on a machined aluminium back plate to make a rigid conformal tool.

2.3.3 Pitch

Polishing pitch has been widely used in optical application for many years. There are mainly two kinds of pitch, the synthetic pitch and the natural pitch. The basic types are wood pitch, rosin pitch, petroleum based and asphalt tar pitch. The properties of these different pitches vary because of the different material they are made from. Two important properties which affect the performance of pitch are viscosity and shear

modulus. The viscosity is generally described as the resistance of a material to flow while shear modulus reflects the elastic behaviour (Gillman and Tinker, 1999).
For example, Gugolz Polishing Pitch is made from natural wood resin and has five grades from very-soft to very-hard. It is easy to use by slicing, melting, and pouring onto a lap. The pitch carries abrasives well, such as aluminium oxide, cerium oxide, and diamond slurries, and presents them efficiently to the optic's surface for a superior finish (Meller Optics, Inc. 2013). The parameters of the pitch are shown Table 5 (Meller Optics, Inc. 2014).

Table 5: Parameters of Gugolz polishing pitch (Meller Optics, Inc. 2014)

Specifications	Melting Point	Flash Point	Burn Point	Softening Point
55-Very Soft	52℃ -55℃	246℃	278℃	63℃-64℃
64-Soft	68℃ -72℃	229℃	262℃	65℃ -68℃
73-Medium	77℃ -80℃	219℃	254℃	71℃ -74℃
82-Hard	79℃ -82℃	210℃	246℃	75℃ -77℃
91-Very Hard	84℃ -87℃	213℃	252℃	78℃

2.4 Polishing spot

Figure 14 shows the modelling of the function of polishing spot and interferometric data from polishing spot in MRF.

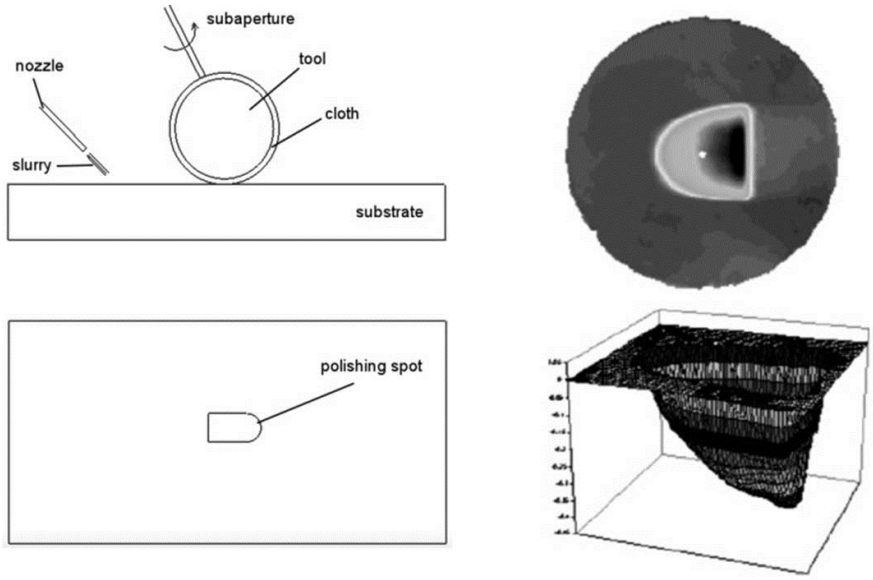

Figure 14: a) Modeling of the function of polishing spot; b) Interferometric data from polishing spot in MRF (Evans et al., 2003)

The modeling of the function of polishing spot is shown in Figure 14a. Parameters affecting the polishing spot comprise rotation speed of tool, tool pressure, dwell time and the contact extent during tool and substrate. With faster tool rotation speed, higher tool pressure and longer dwell time on the substrate, more material were removed away

because of the better contact during tool and substrate. Preston's equation explains the function of polishing spot well (see equation 1.3.1.1), the material remove rate (MRR) is in proportion to the downward pressure (P) and relative velocity (V). The removed material is in proportion to the tool pressure, rotation speed and dwell time.
Figure 14b shows the interferometric data of polishing spot in MRF which was produced by the high shear stress in the contact zone within which the material was removed away over a portion of the work piece surface (Evans et al., 2003).
The characteristic of material removal has been expressed as the influence function which was described by Walker et al. (2004) as polishing spot produced by a spinning polishing tool imposing a cutting action on a certain location of a workpiece surface (Zeng, 2012).

2.4.1 Tool angle

A polishing tool angle is required for the following reasons: First, a needed rotation speed can be achieved by defining the tool angle as the speed at the tool centre is zero. Then a polishing spot can be achieved by a proper tool angle considering the tool pressure and rotation speed. Next, a tool angle is required when polishing a freeform shape surface considering the tool position.

2.4.2 Spot size

Spot size is the dimension of the polished area generated by tool compliance and polishing pressure caused on the surface of the sample.
Johns et al., (2007) reported that extent of edge effect is proportional to spot size, but polishing time is (roughly) inversely proportional to spot size during MRF (see Figure 15).

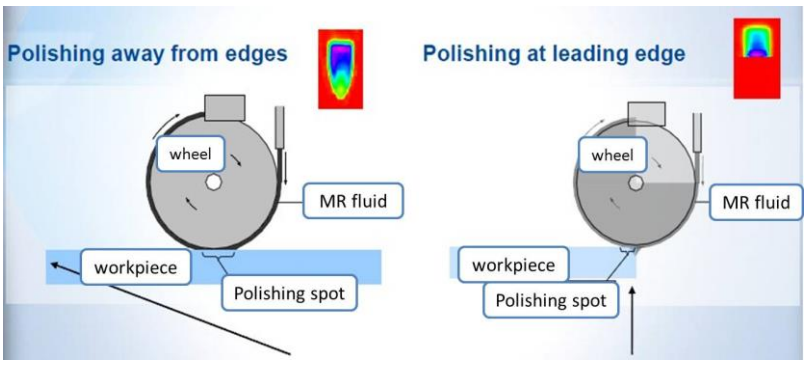

Figure 15: Different size of spots over edges and surface (Johns et al., 2007)

In order to minimize the edge effect and improve the polish rate, it is suggested to use smaller spot (lower plunge depth) near edges where edge effects are anticipated and use larger spot (higher plunge depth) away from edges to remove material quickly (see Figure 16).

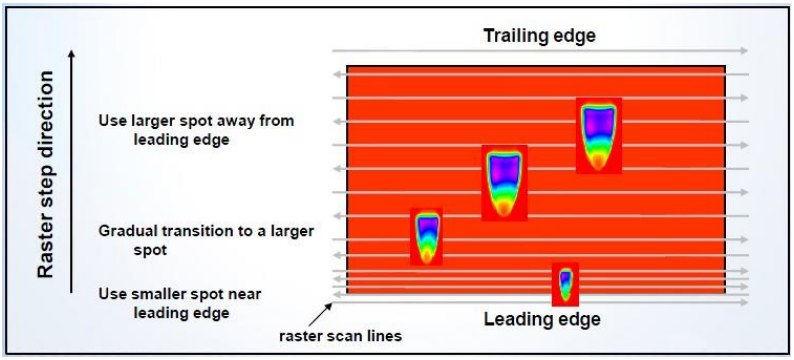

Figure 16: Using different size spots according to the location of workpiece (Johns et al., 2007)

Kim et al., (2009) designed a parametric model to predict the tool influence function (TIF) for the situations of a polishing tool on the edge of the sample. The polishing spot near the edge of the sample is very complex due to different polishing pressure, tool shape, dwell time and other parameters.

2.4.3 Polishing pressure

One of the major differences between polishing process and other machining process, for example cutting, milling and grinding, is that the former is performed by pressure control but the latter is controlled by position. The average polishing pressure is achieved by polishing force or polishing load divided by the polishing spot which is the contact area between the polishing tool and the optical component (Guo et al., 2013).

Mori et al. (1976) and Tsuwa et al. (1979) spread the concept of Elastic Emission Machining (EEM) to CNC shaping and finishing semiconductors and glass which employed 0.5 N/mm^2 polishing pressure; Walker et al. (2002) introduced the polishing pressure employed to polish the Extremely Large Telescope (ELT) segments using a Precession CNC polishing machine IRP200 with cerium oxide on polyurethane was 0.1 N/mm^2 with the average full spot size of 180mm; Guo et al. (2013) introduced the technology of ultra-precision polishing micro-optics whose polishing pressure was controlled within the range of 0-1 N/mm^2 with the polishing spot size under 0.2mm^2.

2.5 Polishing slurry

Polishing slurry is comprised of the fluid and the solid granules phase.

The fluid phase may be characterized by its chemical composition and by its physical properties. Chemical compositions include water and nonaqueous fluids like hydrocarbons and alcohols. The pH may be controlled by adding acids or bases, or using a buffer system. Physical properties, including viscosity, density and thermal conductivity, affect both fluid dynamics and material transport in polishing. There are two main sources of heat during polishing: the primary one is mechanical friction and the less important one is exothermic chemical. Several factors, such as pressure, velocity, geometry and fluid supply, will affect the overall slurry temperature.

The function of solid granules is to mechanically remove material from the surface of the workpiece. The granules themselves can be distinguished by a number of factors, such as chemical composition, size, shape and concentration. Concentrations may be defined as

weight percent or particles per volume. At very large particle concentrations, the removal rate per particle will be proportional to the penetration depth theoretically which means that removal rates will depend on particle size and concentration. At very low concentrations, the particles will be embedded that they no longer carry the whole load because load per particle is large enough (Evans et al., 2003).

2.5.1 Cerium oxide

Cerium oxide is an inorganic solid, mono-constituent, appearing under the form of a white ivory to pale beige powder. It is not categorized as harmful to human health and environment according to the current research. Cerium oxide is mainly used for industrial purpose as polishing slurry for glass products in the high precision manufacturing field (Rhodia, 2012). Table 6 shows the physical and chemical properties of cerium oxide.

Table 6: Properties of cerium oxide (Rhodia, 2012)

Property	Value
Physical state	Solid at 20℃ and atmospheric pressure
Form	Powder
Particle size (D50)	41nm to 20 μm
Colour	White ivory to creamy white-pale beige
Flammability	Non flammable
Vapour pressure	No potential for volatilisation
Water solubility	Very low water solubility

2.5.2 Diamond

The industrial diamond is commonly used in lapping and polishing processes whose characteristic influences the performance of the manufactured workpiece.
Industrial diamonds are mainly manufactured from synthetic sources into mono-crystalline diamond, polycrystalline diamond or nano-crystalline diamond. Mono-crystalline diamond is widely available while polycrystalline diamond is not but often micronized into narrow fractions as the material for lapping and polishing.
The parameters of industrial diamond, such as particle size, particle sharp and particle concentration, as well as the liquid component of the slurry affect the performance of the manufactured mirror.
Particle mean size influences material remove rate and surface roughness of the final workpiece. Choi et al., (2004) reported that the polishing rate increases in direct proportion to particle concentration and decreases with increasing particle size on the micro- and nanoscales. (See equation 2.5.2.1, where A is contact area, C_0 is particle concentration and ϕ is particle diameter).

$$A \propto C_0^{1/3} \phi^{-1/3} \tag{2.5.2.1}$$

Particle sharp affects the performance of the final workpiece as well as the ability of the particle to embed in the lapping plate. Each mono-crystalline has a few sharp edges and corners which will potentially interact with the workpiece to machine the surface. Polycrystalline diamond has a rougher surface with more cutting points which increases the possibility of interacting with the workpiece to achieve a higher material remove rate

and a lower surface roughness.

The ingredient of the polishing slurry has several effects. First, it ensures the same dispersion and controlled distribution of the diamond of the lapping plate and polishing cloth; then, the slurry acts as lubricant to stop the temperature of the workpiece from rising when interacting with abrasives; Moreover, the slurry takes away the fine debris resulting from abrasion (Ng and Dumm, 2012).

2.6 Summary

This project employed the lapping machine and the BoX grinding machine to prepare the fused silica and ULE glass samples. The robotic polishing process using an industrial FANUC robot was the research emphasis of this project. The polishing tools employed in this project were polyurethane tool and pitch polishing tool. The tool path generated was followed a raster motion. The polishing slurry selected was cerium oxide. Three different polishing methods were researched: robot polishing with polyurethane tool and cerium oxide, pitch polishing with pitch tool and cerium oxide, as well as polishing a large part ULE sample. The metrology equipment, such as LVDT, CMM, profilometer and interferometer, used to measure the surface quality before and after polishing process, are introduced in Chapter 3.

3. Experimental equipment and procedures

3.1 Metrology Equipment

3.1.1 Linear Variable Differential Transformer

A Linear Variable Differential Transformer (LVDT) is a displacement transducer which alters a linear displacement or position from a mechanical reference into a proportional electrical signal containing phase (for direction) and amplitude information (for distance). The reasons that the LVDT operation does not demand electrical contact between the moving parts and the transformer and without any built-in electronic circuitry make it widely used in aerospace applications where high reliability is required. Figure 17 shows the cross-section of both short stroke and long stroke LVDT.

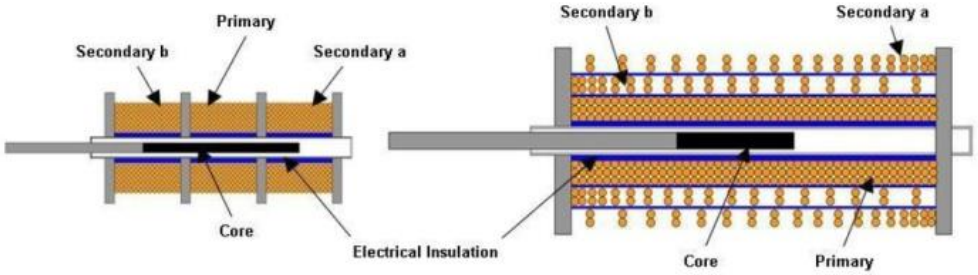

Figure 17: LVDT cross-section, short stroke (L) and long stroke (R) (Measurement Specialties, LVDT**)**

The LVDT comprises of a primary coil wound over a cylindrical non-conductive material coil form. Two secondary coils are wound and classically connected in “opposite series”. A ferromagnetic core magnetically pairs the primary to the secondary winding turns.
The LVDT probes used in this project were Inductive Probe Millimar 1301 and 1303. Table 7 shows specifications of the probes.

Table 7: Specifications of Inductive Probe Millimar (Millimar, LVDT)

Probe type	1301	1303
Measuring range	± 1.0mm	
Measuring force at the electrical zero point	0.75N ± 0.15N	
Increase in measuring force	0.4 N / mm	
Sensitivity deviation	0.5 %	
Repeatability	0.1μm	

3.1.2 Profilometer

The model of profilometer used in this project was a Form Talysurf 120L (see Figure 18). It is a surface form and texture measuring instrument equipped with a selection of stylus for form, waviness and roughness measurement (Ultra precision, Talysurf).

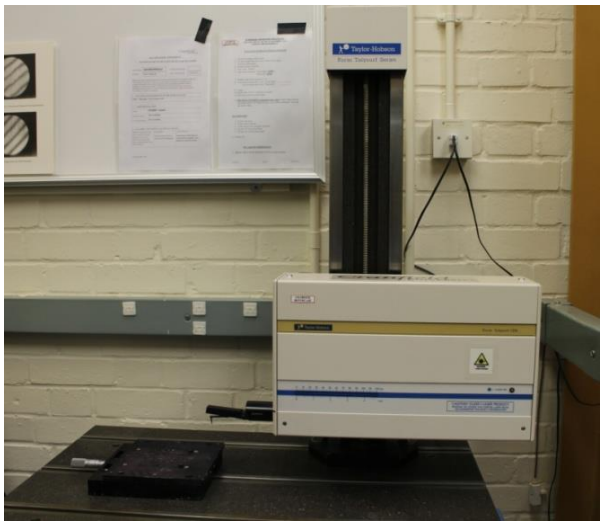

Figure 18: Form Talysurf 120L profilometer

Table 8 shows specifications of Form Talysurf 120L profilometer. The Talysurf has a nanometer resolution throughout a 10mm gauge range with interferometric gauge.

Table 8: Specifications of Form Talysurf 120L profilometer (Leuven, 2005)

Traverse Length	120mm
Traverse Speed	10mm/sec maximum
Measuring Speeds	1mm and 0.5mm/sec ±5%
Return Speed	up to 5mm/sec
Measuring Range	10mm
Gauge Type	Phase Grating Interferometer, 1mN force nominal
Resolution	12.8nm @ 10mm range
Range to Resolution Ratio	780,000:1
Straightness Accuracy	0.5 µm over 120mm traverse 0.2 µm over any 20mm traverse
Data Resolution	0.25 µm

3.1.3 Co-ordinate Measuring Machine

The Co-ordinate Measuring Machine (CMM) used in this project was a Leitz PMMF302010 (see Figure 19).

Figure 19: Leitz PMM-F measuring machine (Hexagon metrology, 2014)

The Leitz PMM-F measuring machine is equipped with an integrated active vibration damping system and kept with temperature and humidity control systems. It is a high-accuracy monolithic gantry measuring machine for large workpieces. Table 9 shows the specifications of Leitz CMM, including the stroke and accuracy.

Table 9: Specifications of Leitz CMM (Hexagon metrology, 2014)

Temperature range	X stroke [mm]	Y stroke [mm]	Z stroke [mm]	Accuracy [μm]
18 ℃ – 22 ℃	3000	2000	1000	$E_0 = 1.7 + L/400$
18 ℃ – 24 ℃	3000	2000	1000	$E_0 = 1.7 + L/300$

It can achieve a traceable accuracy of 5.7 μm for a 1.5m component (Ultra precision, Leitz CMM).

3.1.4 Interferometer

For the 100mm square sample, the model of interferometer used in this project was a Fisba Zygo Optik Microphase 2 OT Interferometer (see Figure 20) which is comprised of table stand (a), lenses (b), interferometer uPhase^{R} 2 SR/HR (c), PC (d), software uShape^{TM} (e), dongle (f) and light source (g) (Fisba Optik, 2004).

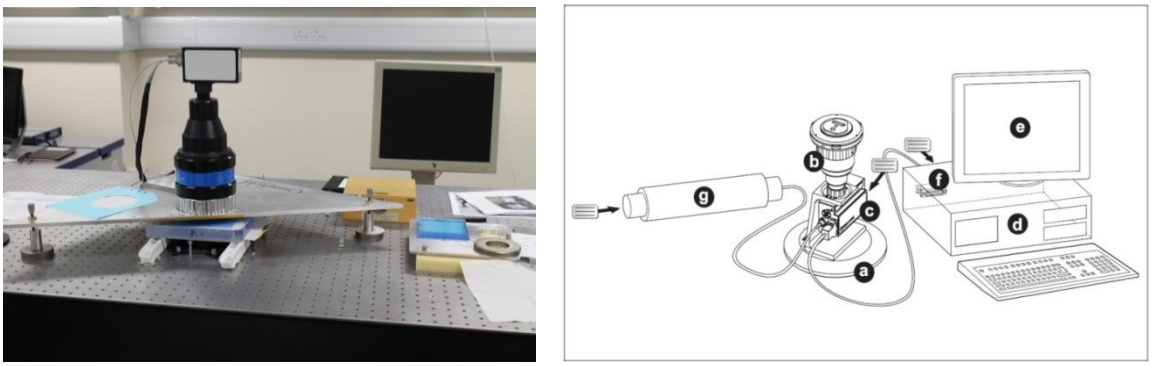

Figure 20: Picture and components of the Fisba Zygo interferometer (Fisba Optik, 2004)

Microphase interferometers are widely used for measuring the surface and wavefront of

components made of glass, plastic, metal or ceramic objectively and precisely. One outstanding advantage of the measurement is the non-contact measurement method which prevents damage to the sample under test and gives the most exact evaluation of the entire surface or wavefront (Ultra precision, Microphase interferometer).
The Fisba Zygo can measure sample up to 100mm. Table 10 shows the specifications of Fisba Zygo interferometer.

Table 10: Specifications of Fisba Zygo interferometer (Fisba Optik, 2004)

Camera resolution	[pixel]	512x512
Usable resolution	[pixel]	Ø ~480
Measurement range	[mm]	1-5
Measurement wavelength	[nm]	632.8
Reference temperature	[℃]	21
Search area	[℉]	5
Operational temperature	[℃]	15...30
PV Accuracy of iteration	[λ]	< 1/200
RMS Accuracy of iteration	[λ]	< 1/1’000
Illumination diameter	[mm]	5

For the 400mm square mirror, the model of interferometer selected was a Zygo Laser Interferometer Dynafiz (see Figure 21).

Figure 21: Zygo Laser Interferometer (DynaFiz, 2013)

The Zygo DynaFiz™ dynamic laser interferometer is designed particularly for implementing accurate metrology of optics in the company of air turbulence and extreme vibrations. The merits of the system, such as the high light efficiency of the optical system and the long life, high power, HeNe laser source, enables operation at high camera shutter speeds that “freeze” vibration. This dynamic capability provides reliable metrology in environments that are too violent for traditional temporal phase shifting techniques (Ultra precision, Dynafiz). Table 11 shows the specifications of Zygo Laser Interferometer.

Table 11: Specifications of Zygo Laser Interferometer (DynaFiz, 2013)

System overview	Measurement Capability	Measures surface form of reflective materials and optics, and transmitted wavefront of transparent optics
	Test Beam Diameter	4 inch (102mm) or 6 inch (152mm)
	Laser Source	High power stabilized HeNe, Class IIIa
	Wavelength	632.8 nm
	Frequency	< 0.0001nm
	Camera Resolution	1200 x 1200 pixels
Performance	RMS Simple	< 0.06 nm, λ/10,000 (2 σ)
	RMS Wavefront Repeatability	Dynamic: < 1.0nm, λ /600 (mean + 2 σ) PSI: < 0.25nm, λ /2500 (mean + 2 σ)
	Fringe Resolution	Dynamic: 250 fringes (all magnifications) PSI: 500 fringes (all magnifications)

3.2 Experiment procedures

The experiment procedures are comprised of the following steps: robot based polishing platform, polishing slurry preparation, polishing tool preparation, samples preparation and various polishing methods which include robot polishing with polyurethane tool and cerium oxide, pitch polishing with pitch tool and cerium oxide as well as polishing large ULE part.

3.2.1 Robot based polishing platform

The robot based polishing platform in Cranfield University is composed of an industrial robot, a high precision air bearing spindle as well as a commercial slurry system, which was designed to remove subsurface damage and mid-spatial from the ground surface. Figure 22 shows the layout of the platform.

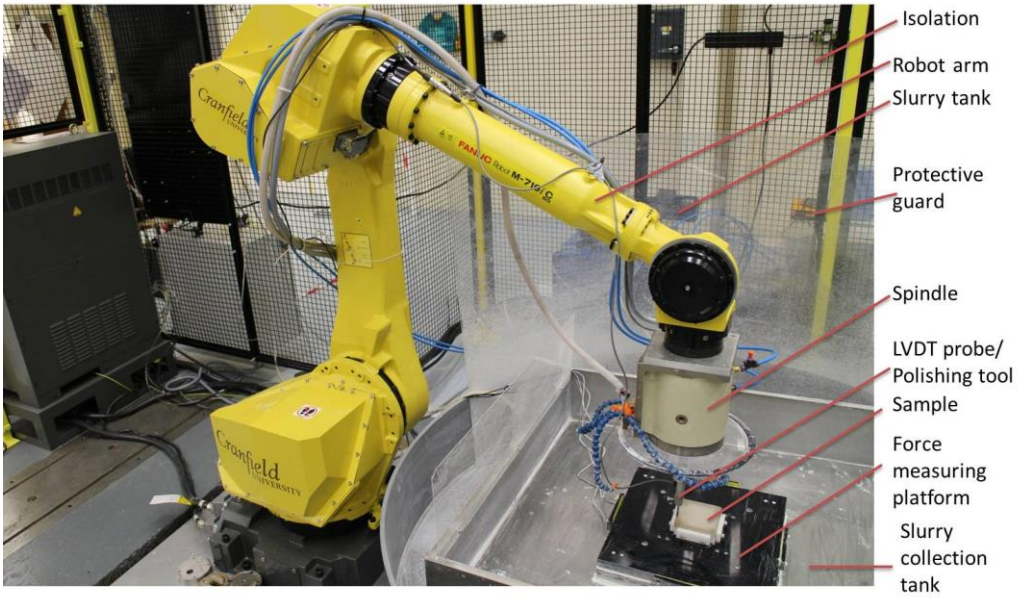

Figure 22: Industrial robot based polishing system

The industrial robot is a six axis Fanuc M710ic/50 with a working envelope which makes it suitable for polishing optics up to 1.5 meters. The PI air bearing spindle utilizes the compressed air to rotate the polishing tool fixed on the spindle to polish the surface. The slurry system was developed to circulate cerium oxide and diamond slurries between the slurry pump and the polishing area (Tonnellier et al., 2013).
The Fanuc controller is a deadman enabling manual and automatic control of the robot. Pressure measuring platform was built via 4 button load cells connected to a PC with Labview program. The complex tool path programming was carried out using a bespoke Matlab program and the simple one was done through Fanuc's own software, namely Roboguide.

3.2.2 Polishing slurry preparation

The polishing slurry, cerium oxide, for polishing ULE and fused silica samples was prepared according to the procedure in Table 12.

Table 12: Polishing slurry mixing procedure

Step	Item
1	2.5 L of EverFlo in a jug;
2	Slowly mix cerium oxide into jug;
3	3.5 L of water in mixing tank (room temperature);
4	Add slowly into mixing tank;
5	Circulate and mix for 2 hours; Check specific gravity among 1.02-1.03 g/cm^3;
6	Add 25L of water;
7	Mix for 1 hour;
Note	EQ #1 (Everflo) = Total tank volume x 0.05 EQ #2 (Amount of cerium oxide) = 2.25 kg for 50L

Additive, Everflo, was added to the slurry mixing tank to reduce the agglomeration of cerium oxide slurry particles.

Figure 23 shows the polishing slurry tank used in polishing slurry preparation process.

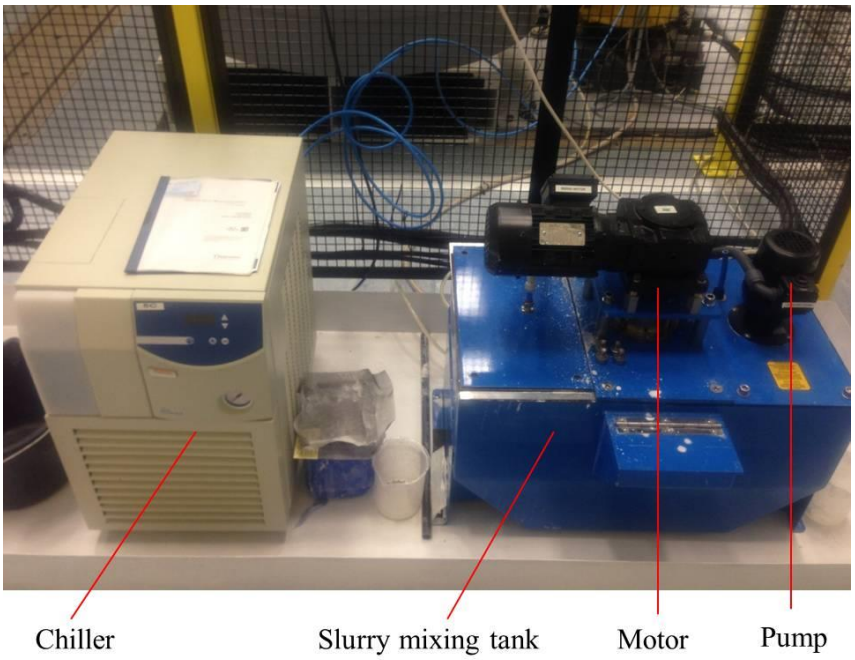

Figure 23: Polishing slurry tank and chiller

The chiller was employed to keep the temperature at a constant 20 degree to prevent the working temperature of the spindle from rising when it rotated for quite a long time. The mixing tank was used to provide a container to mix the polishing slurry. The motor was employed to stir the polishing slurry and the air pump was used to circulate the polishing slurry from the polishing zone to the mixing tank.

3.2.3 Polishing tool preparation

3.2.3.1 Polyurethane tool preparation

The polyurethane used in this project was LP-66. Table 13 shows the procedure employed to make the polyurethane polishing tool whose components are shown in Figure 24.

Table 13: Polyurethane polishing tool making procedure

Step	Item
1	Mix polyurethane substrate part A and part B into the tool mould according to the prescription;
2	Modify the substrate surface to the required curve;
3	Cut the polyurethane pad to round piece whose diameter is the same as the substrate and glue it on the surface of the polyurethane substrate.

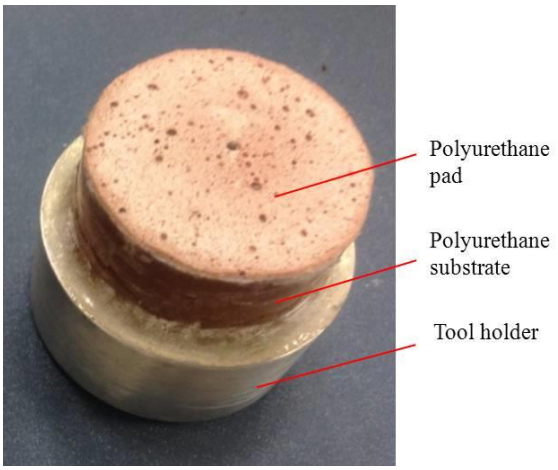

Figure 24: Polyurethane polishing tool

3.2.3.2 Pitch tool preparation

The pitch used in this project was Gugolz polishing pitch (N0. 73). Table 14 shows the procedure employed to make the pitch polishing tool whose components are displayed in Figure 25.

Table 14: Pitch polishing tool making procedure

Step	Item
1	Mould was greased with Silicone Grease on faces which were wanted to be released;
2	Fill assembled moulds with a controlled amount of pitch;
3	Put the mould and pitch into oven: set the temperature at 120℃ for 20 minutes;
4	Take out the mould from the oven, cool down the pitch to soft and modify the shape of the tool surface with cold top mould;
5	Remove the pitch tool from the mould;
6	Heat up the top mould to 75℃ and modify the tool surface, use abrasive paper to modify the tool edge;
7	Measure and modify the roundness of the pitch tool.

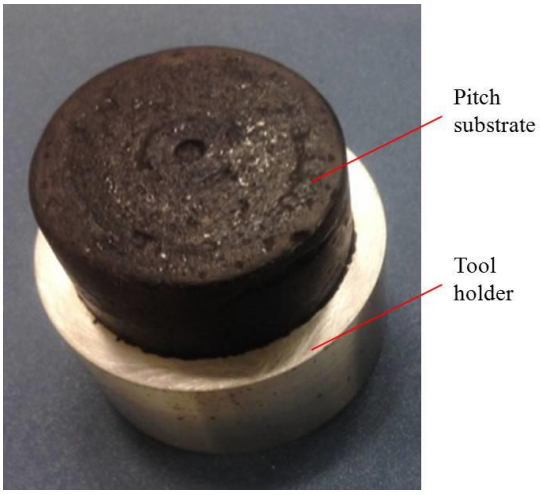

Figure 25: Pitch polishing tool

3.2.4 Samples preparation

3.2.4.1 Lapped 100mm square ULE sample

Figure 26 shows the lapping process of 100mm square ULE sample.

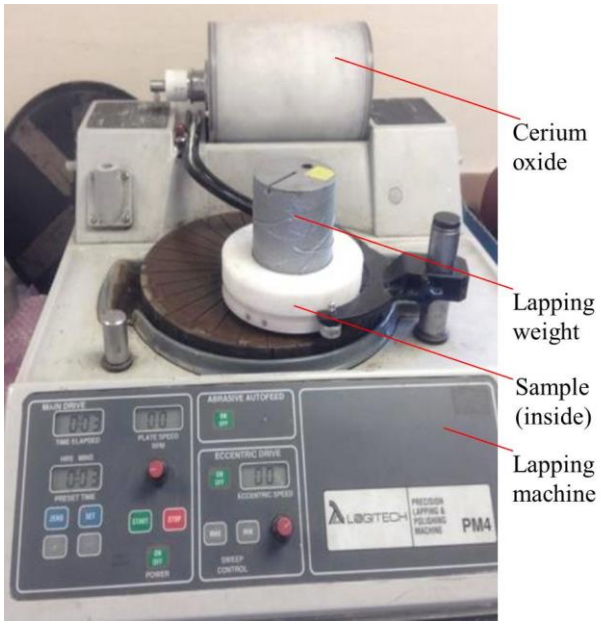

Figure 26: Lapping 100mm square ULE sample

The parameters of lapping process are displayed in Table 15.

Table 15: Parameters of lapping 100mm square ULE sample

Item	Parameter
Diameter of cerium oxide	9 μm
Lapping time	60 minutes
Lapping weight	5kg
Rotation speed of lapping plate	60 rpm

The form accuracy and roughness of the sample were measured using the Talysurf profilometer following the method highlighted in Figure 27. The measurement directions were 1, 2, 3 and 4.

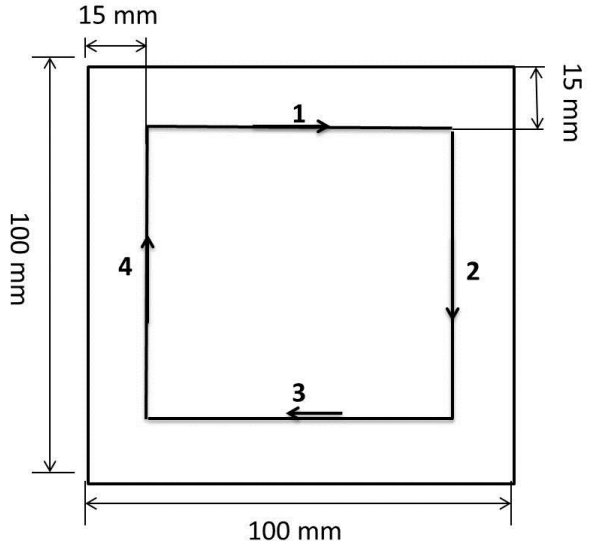

Figure 27: Measurement method of the 100mm square lapped ULE sample

3.2.4.2 Ground 100mm square fused silica sample

Table 16 shows the parameters of grinding 100mm fused silica sample process.

Table 16: Parameters of grinding 100mm square fused silica sample

Item	Parameter
Grit Size	25 µm
Depth of Cut	50 µm
Feed rate	1.5 mm/rev
Surface Speed	25 mm/s
Cutting Speed	30 m/s

The form accuracy and roughness of the sample, after the grinding process, were measured using the Talysurf profilometer following the method described in Figure 28. The curved lines represent the cusps generated by the grinding process. The measurement directions were 1, 2, 3, 4, 5 and 6.

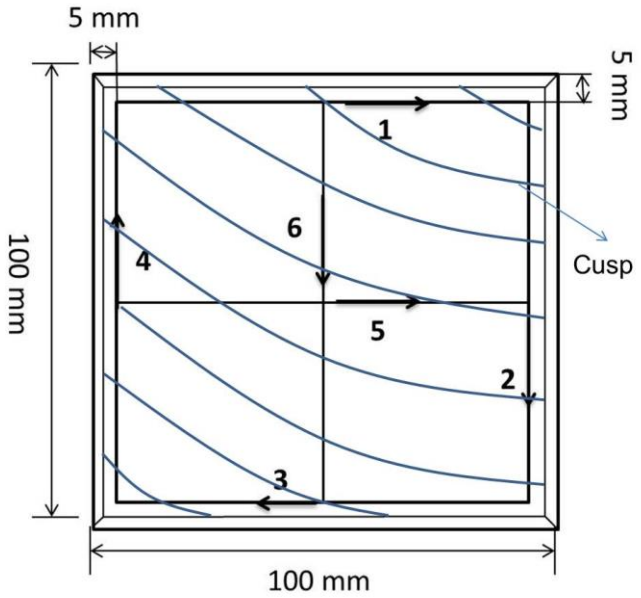

Figure 28: Measurement method of the 100mm square ground fused silica sample

3.2.4.3 Ground 400mm square ULE sample

Table 17 shows the parameters of grinding of the 400mm square ULE sample.

Table 17: Parameters of grinding 400mm square ULE sample

Item	Parameter
Grit Size	46 µm
Depth of Cut	50 µm
Feed rate	1.5 mm/rev
Surface Speed	25 mm/s
Cutting Speed	30 m/s

The form accuracy of the sample after the grinding process was measured using the CMM. The roughness, edge effect and the cusp condition were measured using the Talysurf profilometer following the method demonstrated in Figure 29.

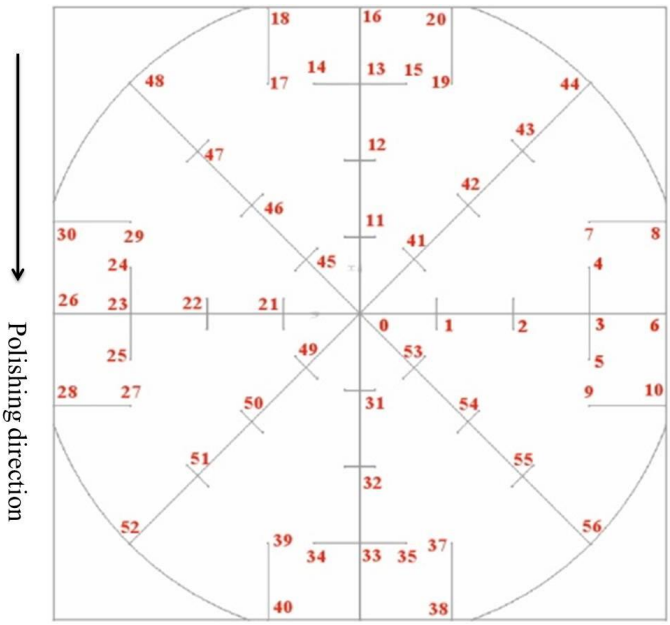

Figure 29: Roughness, edge effect and cusp condition measurement method of large ULE sample

The dimensions of the sample are 400mm square. The diameter of the ground region is 425.7mm. The surface roughness, edge effect and cusp condition were measured between the following points with a radius of curvature sphere of 3000mm: F0-2, F1-3, F2-6, F4-5, F7-8, F9-10, F0-42, F41-43 and F42-44. Each measurement length was 100mm. Each measurement can be used to analyse the cusp condition and the surface roughness after grinding. The measurement of F2-6, F7-8, F9-10 and F42-44 before and after polishing can be used to analyse the edge effect of polishing. The above measurement procedure was carried out for the other three similar regions of the sample.

3.2.5 Measurement procedure of 100mm square sample

Each 100mm square part was probed using the LVDT probe to generate data for polishing. The probing method was to measure a point every 7mm from 5mm to 96mm in X coordinate and every 30mm from 5mm to 95mm in Y coordinate. Figure 30 shows the flow chart of the probing method.

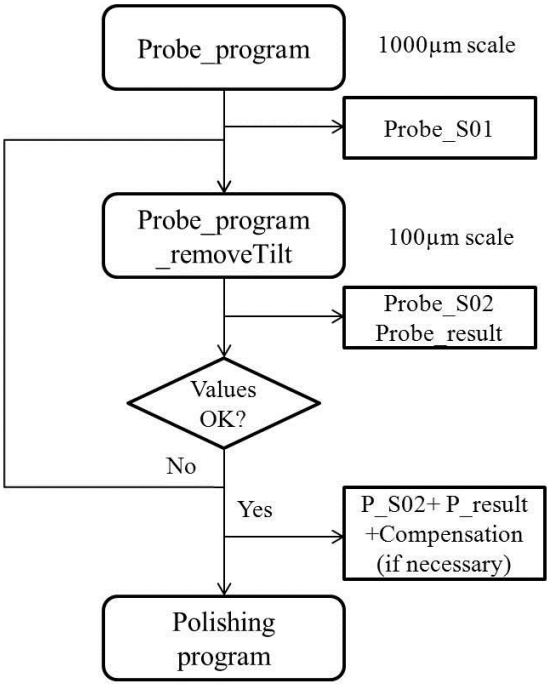

Figure 30: Probe method of measuring 100mm square ULE sample

The Probe_program was used to measure the form accuracy of the part; then the tilt obtained was removed (Probe_S01) to probe the part more accurately. The measurement result (Probe_result) was generated from the program Probe_S02. By adding the values of Probe_S02, Probe_result and the compensation, the result was used to generate the polishing program. The steps motioned above were repeated if the measurement error was over 1000 μm.

3.2.6 Robot polishing with polyurethane tool and cerium oxide

Table 18 shows the parameters of robot polishing with polyurethane tool and cerium oxide.

Table 18: Parameters of robot polishing with polyurethane tool and cerium oxide

Item	Parameter
Polishing pressure	100N
Polishing speed	5 mm/s
Polishing step	1mm
Tool angle	3.5 degree
Tool rotation speed	1000 rpm
Diameter of cerium oxide	9 μm

There are two sets of 100mm square samples, lapped ULE and ground fused silica, to be robot polished. Figure 31 shows the procedure before robot polishing.

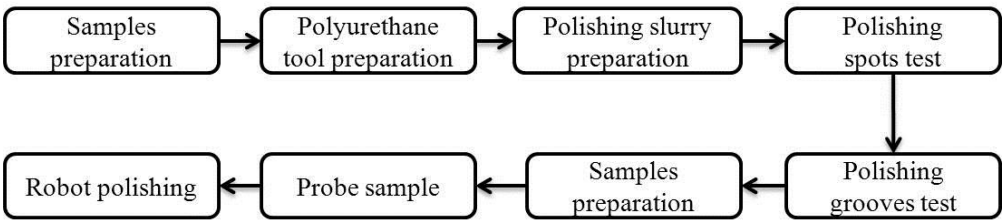

Figure 31: Procedure before robot polishing

First, samples were prepared in accordance with samples preparation in section 3.2.4. Next, the polyurethane polishing tool was made according to polyurethane polishing tool preparation in section 3.2.3.1. The cerium oxide polishing slurry was mixed on the basis of polishing slurry preparation in section 3.2.2. This was followed by polishing spots and polishing grooves tests to investigate the influence of different tool angles, polishing pressures and polishing times. Then the samples were prepared again. Finally, the sample was fixed on the pressure measurement platform to probe it with linear variable differential transformer (LVDT) and robot neutral polishing was implemented. Figure 32 shows the process of robot neutral polishing.

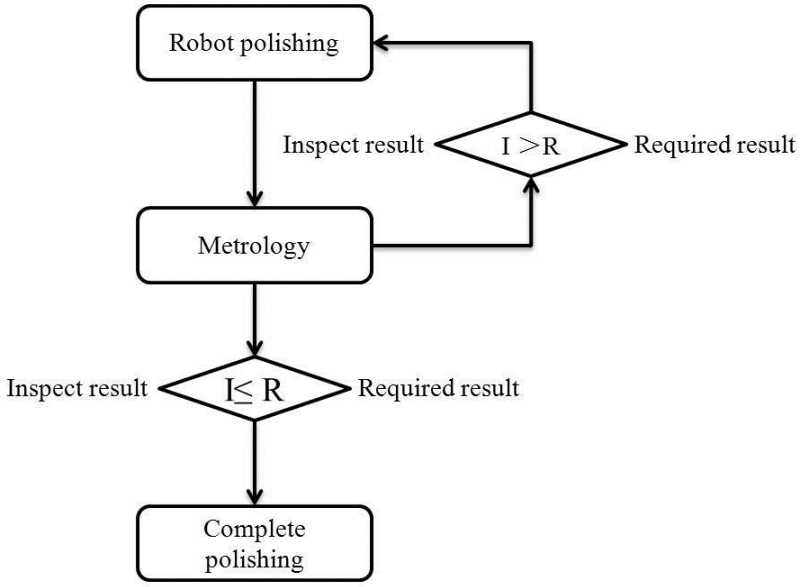

Figure 32: Robot neutral polishing process

Before each robot neutral polishing operation, the LVDT probe was used to measure the part tilt and the robot motion error data which were used to generate polishing program with the bespoke Matlab software. Before and after each polishing operation, the Talysurf profilometer was employed to measure the final polished surface quality. These results before and after the polishing process were compared to evaluate the improvement of surface quality. Robot neutral polishing was completed when the measured result met the requirement.

3.2.7 Pitch polishing with pitch tool and cerium oxide

Table 19 shows the parameters of robot polishing with pitch tool and cerium oxide.

Table 19: Parameters of robot polishing with pitch tool and cerium oxide

Item	Parameter
Polishing pressure	50N
Polishing speed	5 mm/s
Polishing step	1mm
Tool angle	3.5 degree
Tool rotation speed	500 rpm
Diameter of cerium oxide	9 μm

There are two sets of 100mm square robot polished samples to be pitch polished, which were: robot polished ULE sample and robot polished fused silica sample. Figure 33 shows the procedure before pitch polishing.

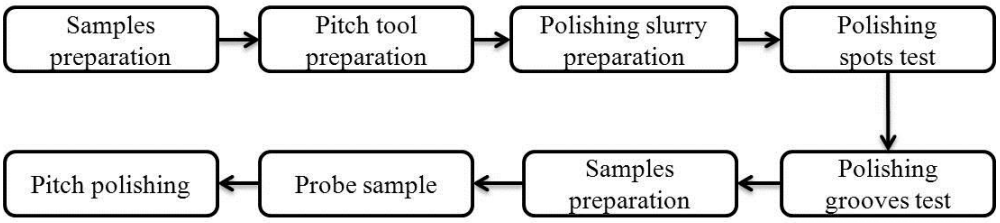

Figure 33: Procedure before pitch polishing

First, samples were robot neutral polished. Next, the pitch polishing tool was made following the pith polishing tool preparation procedure (section 3.2.3.2). The cerium oxide polishing slurry was mixed according to the section 3.2.2. This was followed by polishing spots and polishing grooves tests to investigate the influence of different tool angles, polishing pressures and polishing times. Then the samples were robot polished again. Finally, the sample was fixed on the polishing platform measured using the LVDT probe and the robot pitch polishing was implemented. Figure 34 shows the process of robot pitch polishing.

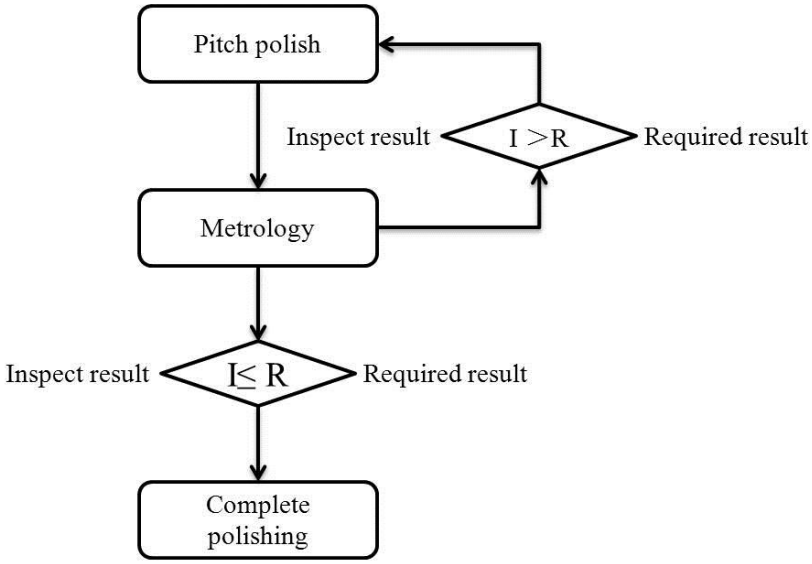

Figure 34: Pitch polishing process

Before each robot pitch polishing operation, the LVDT probe was used to measure the part tilt and the robot motion error data which were used to generate polishing program with the bespoke Matlab software. Before and after each polishing operation, the Talysurf profilometer was employed to measure the final polished surface quality. These measuring results before and after the polishing process were compared to evaluate the improvement of surface quality. Robot pitch polishing was completed when the measured result met the requirement.

3.2.8 Robot polishing 400mm square ULE component

The parameters selected to polish the 400mm square ULE part are summarized in Table 20.

Table 20: Parameters of polishing large ULE part

Item	Parameter
Polishing pressure	80N
Polishing speed	10 mm/s
Polishing step	1mm
Tool angle	3.5 degree
Tool rotation speed	1000 rpm
Diameter of cerium oxide	9μm

The ULE part was polished according to the procedure in Figure 35.

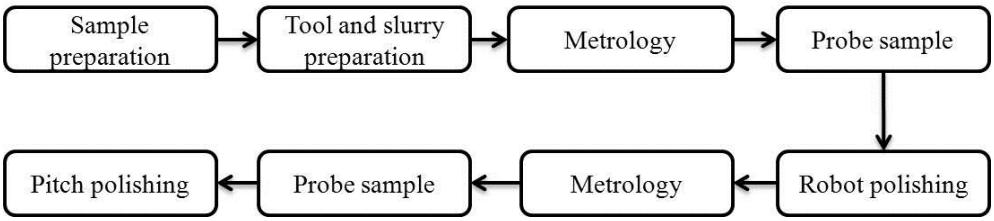

Figure 35: Procedure of polishing large ULE sample

First, sample was ground in accordance with sample preparation in section 3.2.4.3. Next, the polyurethane tool and the pitch tool were made according to polishing tool preparation in section 3.2.3. Then, the cerium oxide polishing slurry was mixed following the polishing slurry preparation in section 3.2.2. This was followed by metrology of the ground part before polishing using CMM and Talysurf. Then the part was probed and robot neutral polished followed by metrology. Finally, the sample was fixed on the polishing platform measured using the LVDT probe again and the robot pitch polishing was implemented. Figure 36 shows the process of polishing 400mm square ULE part.

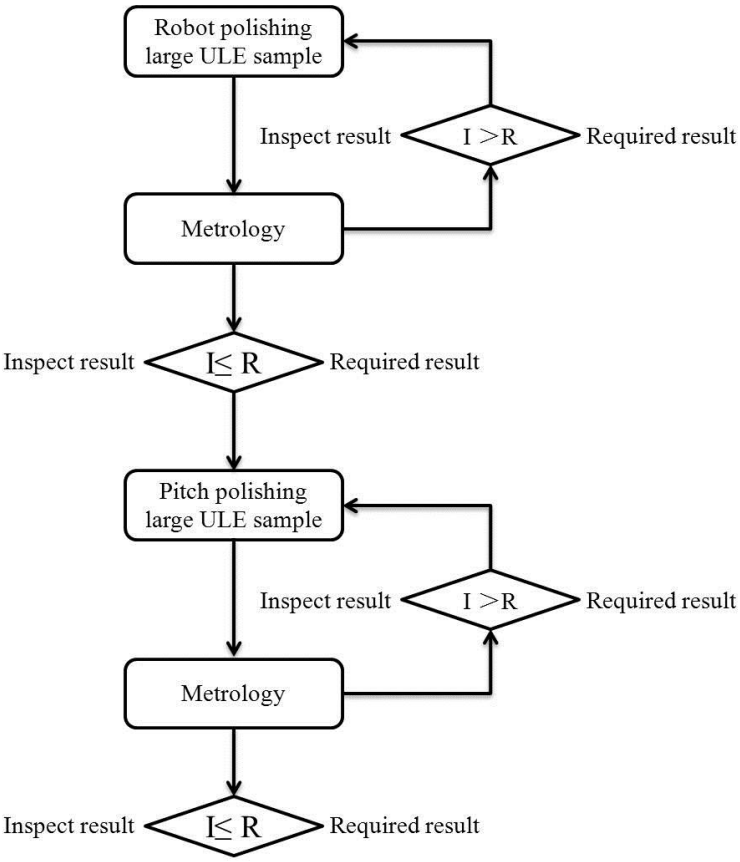

Figure 36: Polishing 400mm square ULE component

Before robot neutral polishing, Leitz CMM and Talysurf profilometer were used to measure the surface quality of the part. After the robot neutral polishing operation, Talysurf profilometer, Leitz CMM and the Zygo laser interferometer with 3m optical tower were employed to measure the surface quality. For the metrology process, CMM was employed to measure the form accuracy of the part, Talysurf was used to measure the

edges, grinding cusps, polishing centre defect and roughness of the part, Interferometer was selected to check the reflectivity and measure the form accuracy of the part. These measuring results before and after robot neutral polishing were compared to see the development of polishing results and the removed condition of cusps. Polishing process was completed when the measured result met the requirement.

3.2.9 Validation

The reasons of polishing the smaller size sample (100mm square) included the following two aspects: 1) the dimension of the sample was big enough to limit the edge effect area affecting the polished surface quality, and 2) the parameters that may affect polishing the larger size sample were tested by polishing the same sample to test the influence of the polishing tool wearing out.

The edge effect would affect the quality of polished surface edge. Therefore, the polished quality of the central area of the surface should be better than the edge area. The solution was to use smaller size polishing spot near the edge to eliminate the edge effect and use a bigger size polishing spot away from edge to increase the polishing rate.

The polishing tool may wear out through polishing for a long period of time. The failure modes monitored mainly included the change of cloth thickness, cloth glazing and the change of cloth structure. The polishing pressure may get smaller when the cloth thickness gets thinner followed by a smaller polishing spot and a lower polishing rate. The cloth glazing leads to a less friction between the sample and polishing tool which would cause a lower polishing efficient. The change of cloth structure reduces the ability of containing the polishing slurry. There are two methods to solve the problem of the tool wearing up: increase the polishing pressure to a proper degree continuously or change to a new polishing tool when necessary according to measured tool pressure or based on the metrology results.

4. Experiment Results

4.1 Calibration of the force measurement platform

The calibration of sensors fixed under the force measuring platform was carried out before polishing process to make sure that the record of polishing pressure was correct and accurate. Figure 37 shows the setup for the calibration of the force measurement platform.

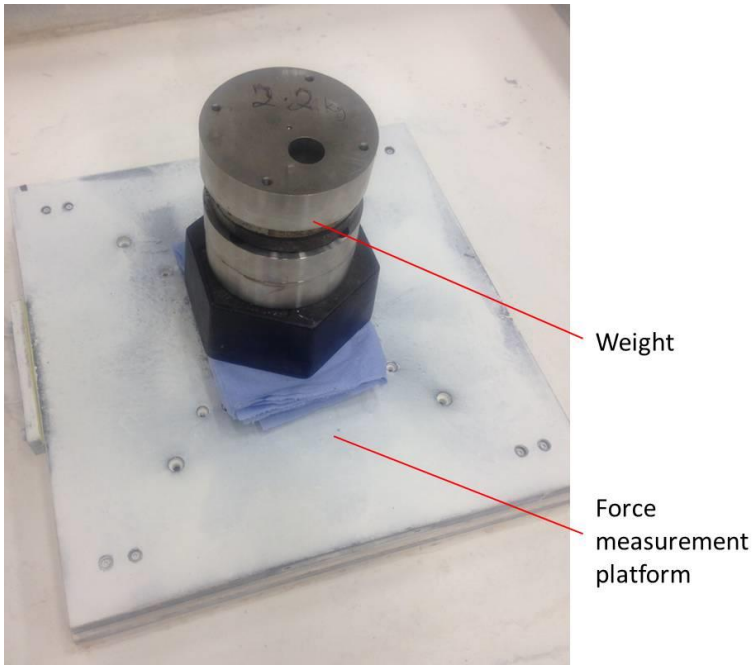

Figure 37: Calibration of force measurement

From the experimental procedure, the maximum polishing force employed was 100N. Five runs of loading from 0N to 139.2N and unloading from 139.2N to 0N were carried out to calibrate the sensors which covered the range of the polishing pressure expected shown in Figure 38 (and the section of A9.1).

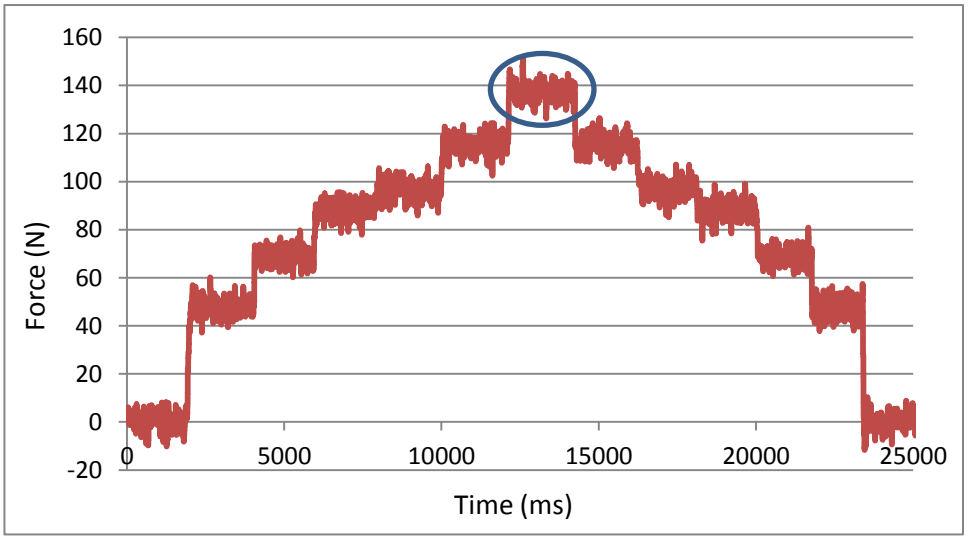

Figure 38: Loading and unloading for force measurement calibration-first run

Table 21 shows the weight selected for the loading and unloading process and the respective recorded force measurement for each run.

Table 21: The record of force measurement validation

Force(N) / Weight(N)	run1	run2	run3	run4	run5
0	-2 ±8	0 ±8	0 ±8	0 ±8	2 ±8
49	48 ±8	48 ±8	48 ±8	48 ±8	48 ±10
68.6	68 ±8	68 ±8	68 ±8	68 ±10	68 ±8
88.2	86 ±8	86 ±8	88 ±8	88 ±8	86 ±8
98	96 ±8	96 ±8	98 ±8	96 ±8	96 ±8
117.6	114 ±8	114 ±8	116 ±8	116 ±8	114 ±8
139.2	136 ±8	134 ±8	136 ±8	136 ±8	134 ±8
117.6	114 ±8	114 ±8	114 ±8	114 ±8	114 ±8
98	98 ±8	98 ±8	96 ±8	98 ±8	96 ±8
88.2	88 ±8	86 ±8	88 ±8	86 ±8	88 ±8
68.6	68 ±8	68 ±8	68 ±8	68 ±8	68 ±8
49	46 ±8	46 ±8	48 ±8	48 ±8	48 ±10
0	0 ±8	0 ±8	0 ±8	0 ±8	2 ±8

It can be seen from the charts and the calibration in Table 21 that the average repeatability of the sensor was within ±8 N. This was due to signal noise effect from sensors employed as shown in Figure 38.

Figure 39 shows the pressure measurement during one polishing run to highlight the factors which affected the force measurement.

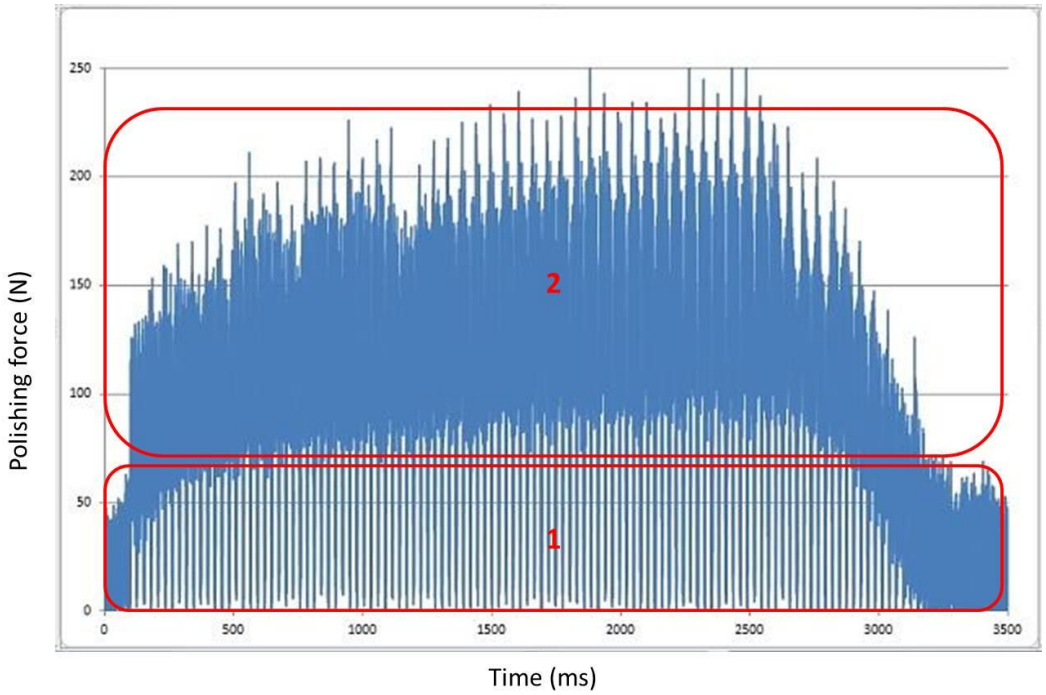

Figure 39: Factors affect the polishing pressure measurement

The first region (1) corresponded to the effect of the polishing slurry being on and the spindle rotating prior to any contact with the part. The second region (2) corresponded to the polishing tool force on the sample surface with the polishing slurry on and spindle rotating. As can be seen the first region, the average effect of the noise and the polishing slurry were 30N. It can be seen from the second region that the average polishing force was 110N eliminating the influence of the noise, the polishing slurry and the tool rotation.

4.2 Calibration of Probing technique

Previous experiments carried out using the robot LVDT probe (Cranfield internal reports, 2012) highlighted a possible effect in measuring repeatability depending on the probe position. The influence of the probe length on the measurement result was checked by probing the form accuracy of a tilt part with different probe lengths. Three different probe lengths were tested and measurement was repeated three times (see Figure 40).

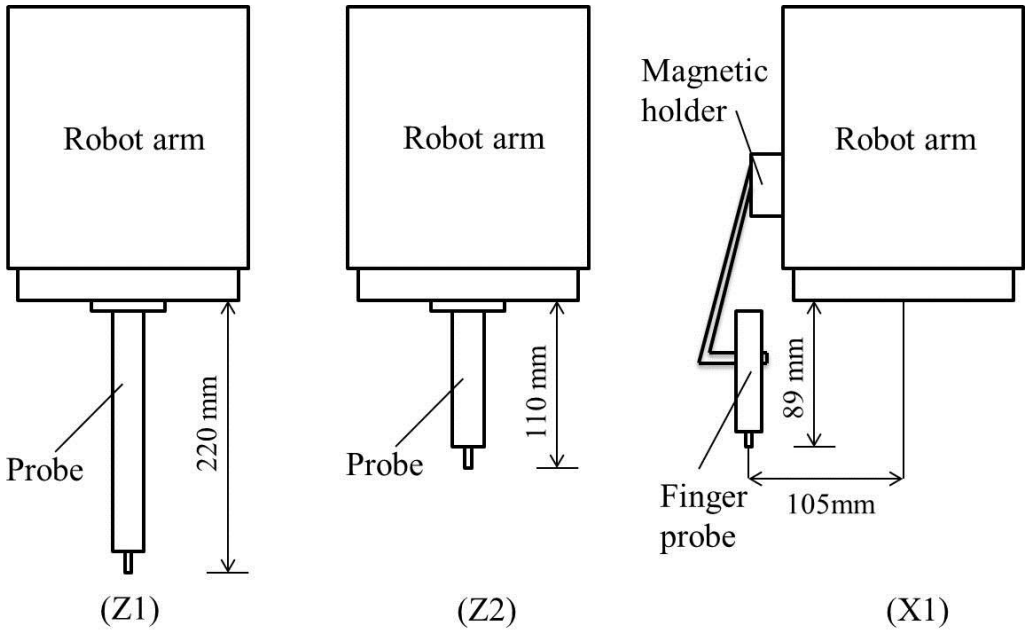

Figure 40: Probes with different lengths

The lengths selected were a Z1 of 220mm and a Z2 of 110mm. The position X effect was also tested with by setting the length of X at 105mm and Z at 89mm with the help of a magnetic holder and a finger probe. Figure 41 combines the probing results.

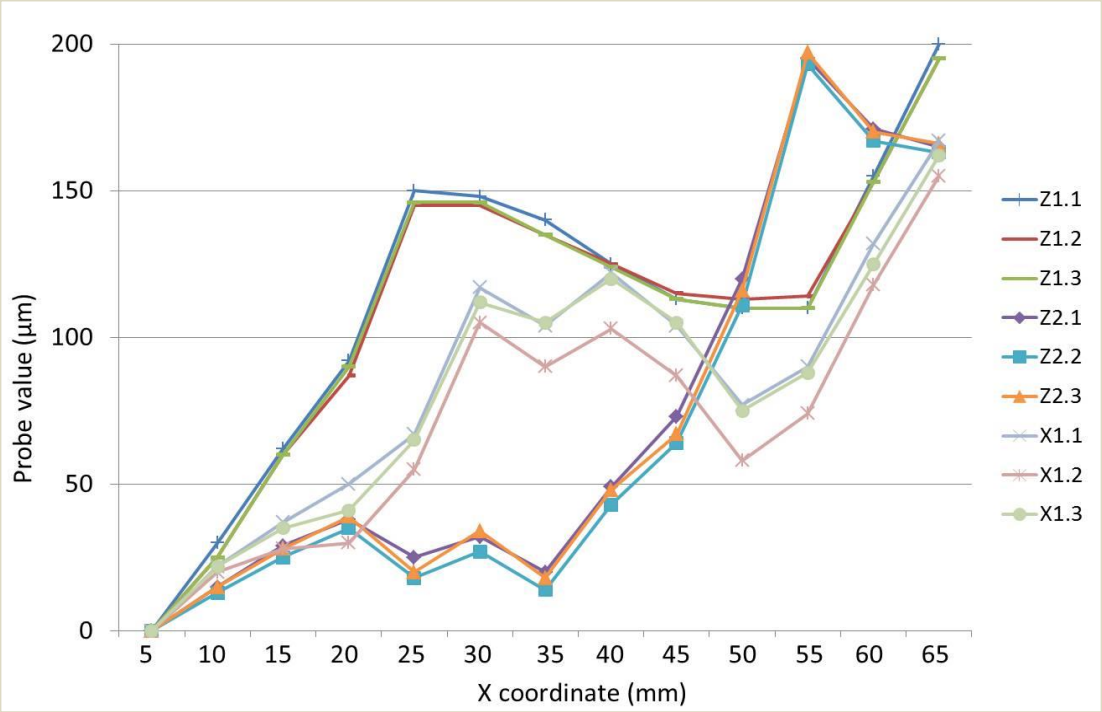

Figure 41: Probing result with different probe lengths

For a given probe length, the results were extremely repeatable. However, the values varied by over 50µm for different position in X and Z coordinates. Therefore, it is important to keep the same length between the probe and the tool so that the robot position error remains the same between metrology and polishing stages. The measurement results also highlighted the positioning errors of robot as the part measured was tilted but the flatness was 5µm.

4.3 Manufacturing polishing tool

Figure 42 shows the polyurethane tool and pitch tool which were manufactured according to the experiment procedure of section 3.2.3.

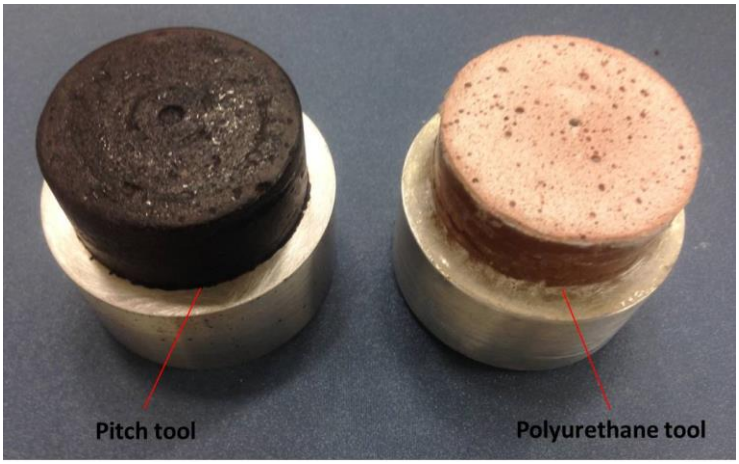

Figure 42: Polyurethane tool and pitch tool

The polyurethane tool was selected based on the previous work carried out at Cranfield

University (Tonnellier et al., 2013). As a pitch tool was never used at Cranfield University, a lot of work had to be carried out on making and testing it which is reported in detail in section 4.3.2.

4.3.1 Polyurethane tool compliance

Several tests were implemented to obtain the relationship between the polyurethane tool depth and the polishing pressure which is required to maintain the correct polishing depth for a constant polishing pressure. Figure 43 shows the connection between the Z position below touch point and the force of the polyurethane tool.

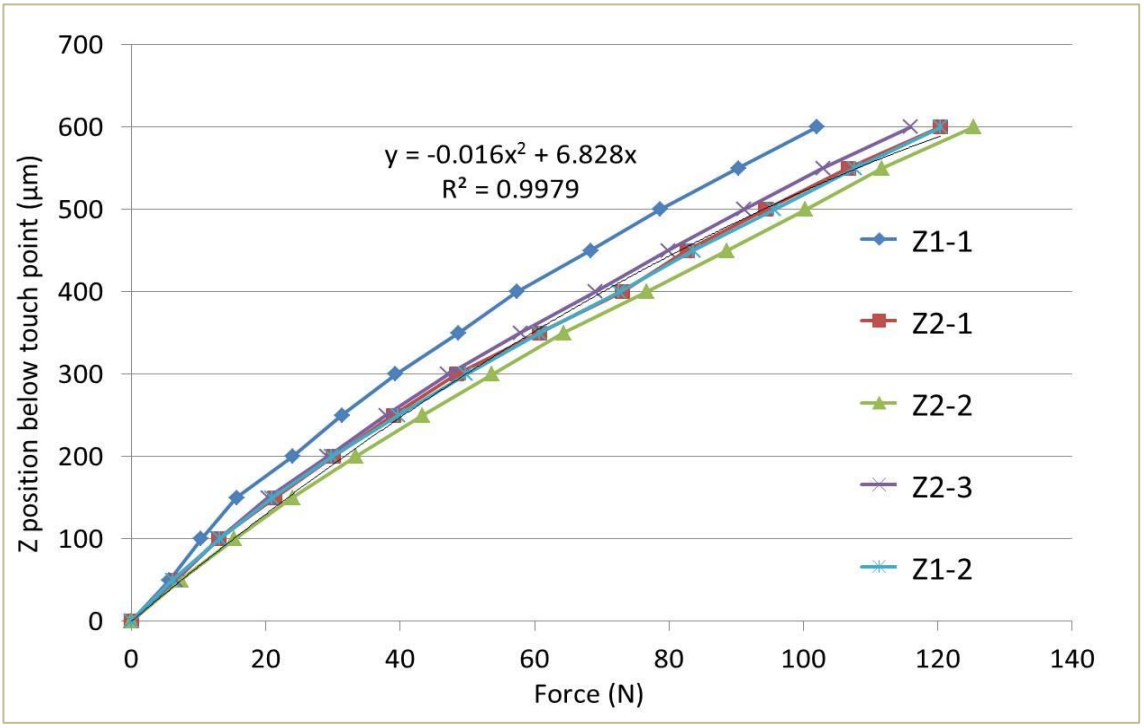

Figure 43: Connection between Z position below touch point and force of polyurethane tool

The tool angle used for these tests was 3.5 degree. This corresponded to the tool angle leading to a more symmetric spot geometry as shown in section 4.4.1. The variation of the Z position below touch point was ±20 µm at the force of 100N. The results of the tests were recorded in section of A9.2.

The equation of the relationship between the Z position below touch point and the force could be reached according to the tendency line (see equation 4.3.1.1), where Y means the Z position below touch point and X means the polishing force.

$$Y=-0.016X^2+6.828X \qquad \text{(Equation 4.3.1.1)}$$

Table 22: Connection between Z position below touch point and force of polyurethane tool

Force(N)	0	10	20	30	40	50	60	70	80	90	100	110	120
Depth(µm)	0	-67	-130	-190	-248	-301	-352	-400	-444	-485	-523	-557	-589

As can be seen from Table 22, -400 µm, -445 µm, -485 µm and -520 µm mean 70N, 80N, 90N and 100N respectively for the 3.5 degree polyurethane polishing tool.

4.3.2 Pitch tool manufacturing

Figure 44 to Figure 47 show the manufacturing process of pitch polishing tool according to the experiment procedure of section 3.2.3.2 “Pitch tool preparation”.

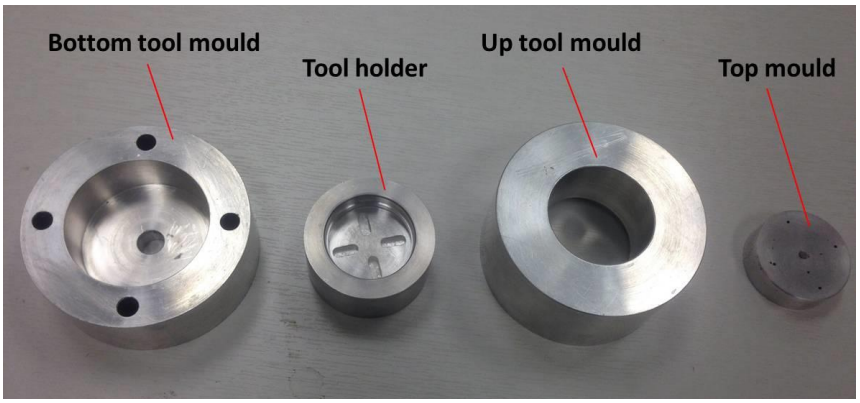

Figure 44: Moulds for making polishing tool

Figure 45: Melt the pitch filled in the moulds with oven closed

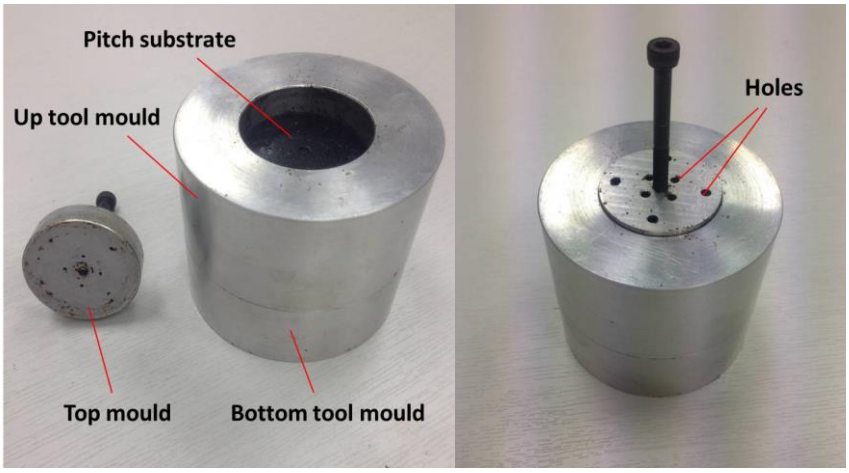

Figure 46: Modify the shape of the tool surface with cold top mould

Several issues had to be addressed to obtain a suitable pitch tool. There were large hollows on the pitch tool surface caused by air bubbles. These were produced by the hot top mould. Four holes were blocked when the pitch melted. The solutions were to use a cold top mould to modify the pitch substrate surface when it was still soft and increased the number of holes on the top mould (see Figure 46).

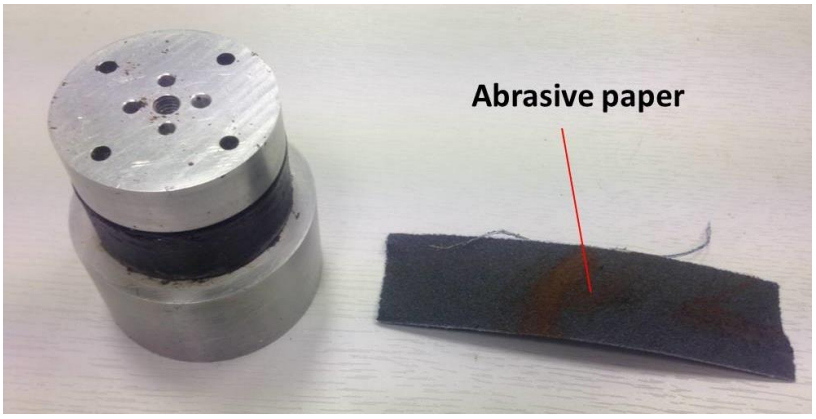

Figure 47: Modify the surface and edge of the pitch tool with hot mould and abrasive paper

The other problems occurred during the initial process of making and testing the pitch tool which were solved by the corresponding treatment methods. First, the pitch substrate was hard to be removed from the moulds and the shape obtained was wrong. The solution selected was to grease silicone grease on mould faces to facilitate release. Second, the pitch tool shook badly due to lack of the concentricity and due to the precision of the tool positioning inside the mould. The treatment method was to modify the design of the mould by machining a step to hold the tool holder precisely so that the tool concentricity improved. Finally, the tool broke during polishing tests as shown in Figure 48.

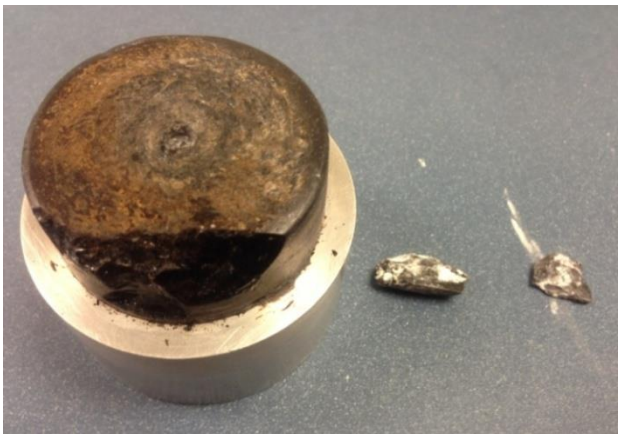

Figure 48: Pitch tool broke during polishing tests

The reasons of the tool breakage include: 1) the temperature increased with the polishing time leading to softening of the pitch; 2) the pitch tool substrate was brittle as the length of tool substrate was long; 3) the polishing pressure selected was too high; 4) the edge of the tool was sharp; 5) the tool angle was too big leading to reduce contact area and increase polishing pressure. The solutions selected were: to chamfer the edge of the tool with the abrasive paper (see Figure 47), decrease the tool length by half and compensate the length with spacer (see Figure 49), and to reduce tool angle and polishing pressure.

Figure 49 shows the final design of the pitch tool.

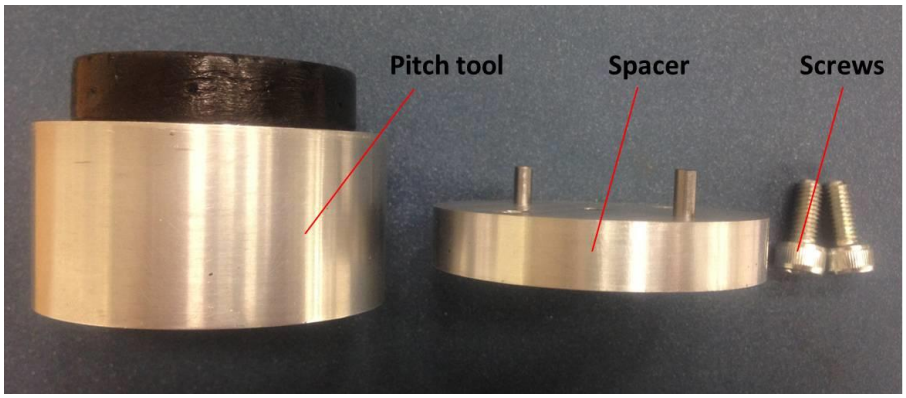

Figure 49: Final pitch tool design

4.3.3 Shaping the pitch tool

The pitch tool was shaped to a radius of 200mm using top mould. However, the spot polishing tests highlighted high vibration level. Therefore, additional shaping process of tool was necessary. Due to the pitch brittleness, chipping of edges occurred when modifying the pitch tool surface on a curved tool mould with the pitch tool rotating. Therefore, the technique selected was shown in Figure 50.

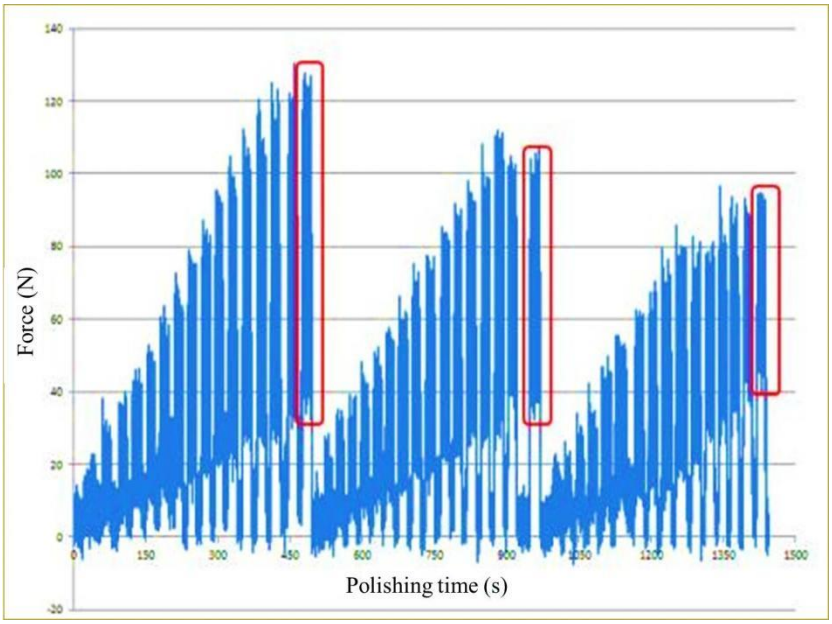

Figure 50: Shaping of the pitch tool

Shaping the pitch tool was carried out with the spindle rotating and the polishing slurry on. The pitch tool rotating speed selected was 500rpm and the tool angle was 3.5 degree. The procedure was: 1) find the touch point; 2) jog the pitch tool to -10 µm in Z direction for 20 seconds and then jog it higher than the touch point; 3) jog the pitch tool to the position 10 µm lower than the previous one for 20 seconds and then move to the position higher than the touch point; 4) the deepest position was -160 µm; 5) repeat the procedure 1 to 4 until the recorded forces are constant.

Figure 51 shows the result of a constant polishing force which could be used to calculate the relationship between the Z position below touch point and pressure of the pitch tool. The polishing slurry effect was about 10 N.

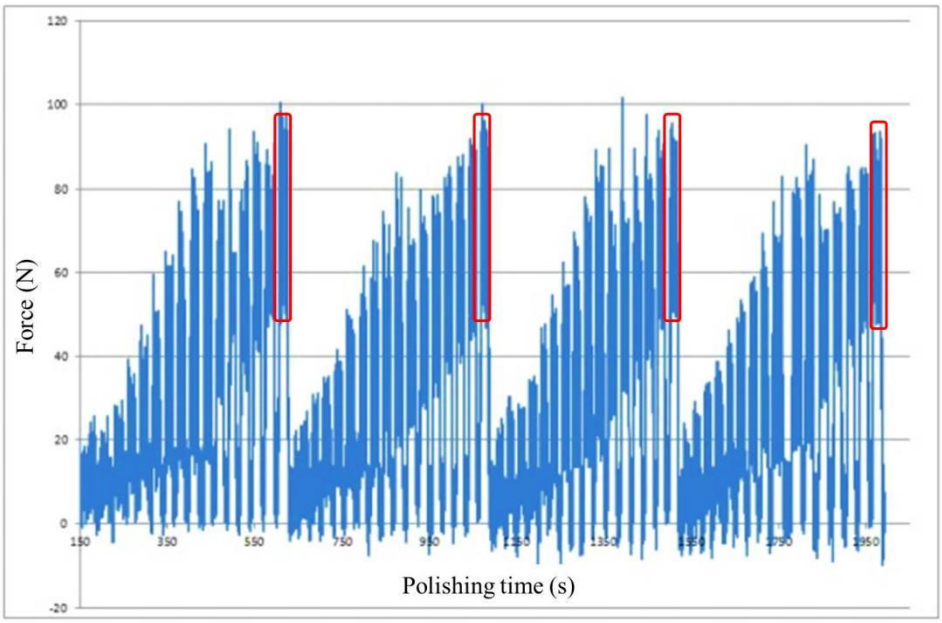

Figure 51: Obtain the constant pitch tool compliance

4.3.4 Pitch tool compliance

As can be seen from Figure 51, the difference of force between each 10 μm displacement in Z direction was 5N. The equation of the pitch tool compliance was summarised in 4.3.4.1.

$$Y=-2X-30 \qquad \text{(Equation 4.3.4.1)}$$

Y means the Z position below touch point and X means polishing force.
The connection between Z position below touch point and force of pitch tool obtained from equation 4.3.4.1 was shown in Table 23.

Table 23: Connection between Z position below touch point and force of pitch tool

Force(N)	0	20	25	30	35	40	45	50	55	60	65
Depth(μm)	0	-70	-80	-90	-100	-110	-120	-130	-140	-150	-160

4.4 Polishing spots

4.4.1 Polyurethane tool

The original polishing process carried out at Cranfield University employed a tool angle of 3 degree. Spots with different tool angles were tested to obtain a more symmetric spot geometry.
For the first experiment, four different angles from 3 degree to 6 degree with the same polishing time (30s) and the same polishing force (80N) were tested. Figure 52 shows the polished spot size obtained with different angles.

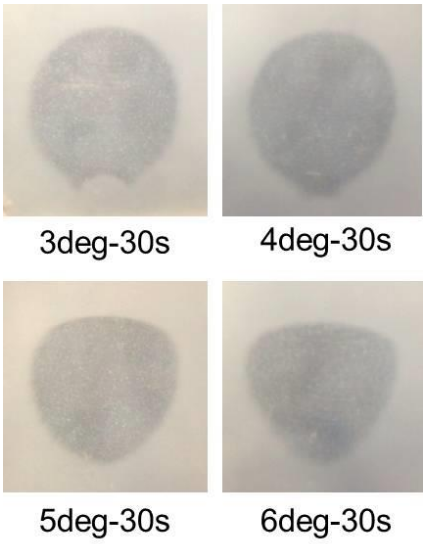

Figure 52: Polishing spots with various angles and the same polishing time - Polyurethane tool

The results show that the polishing angle needed to be set at 3.5 degree to obtain a more symmetric spot.

For the second experiment, two groups of 3.5 degree polishing spots were tested (see Figure 53).

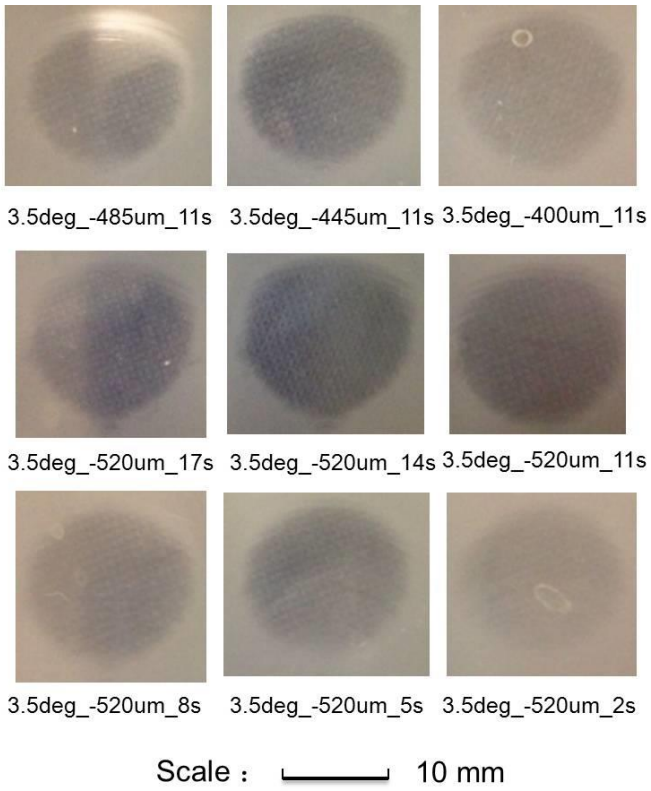

Figure 53: 3.5 degree polishing spots with different force and times-polyurethane tool

One group of polishing spots employed the same polishing time (11s), but different polishing force from 70N to 100N. The other group utilized constant polishing force (100N), but various polishing time from 2 seconds to 17 seconds.

4.4.2 Pitch tool

Figure 54 shows the polished spots generated with the same tool angle and polishing depth but different polishing times.

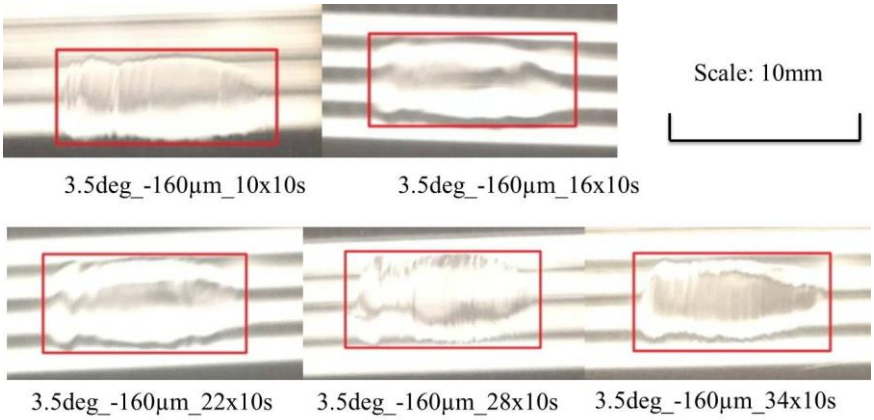

Figure 54: 3.5 degree polishing spots with different polishing times-pitch tool

Table 24 shows the form accuracy (P_t) of the middle of the polished spots.

Table 24: Parameters and form accuracy of polishing spots - Pitch tool

Spot number	Tool angle (degree)	Polishing depth (µm)	Polishing time (s)	P_t (µm)
1	3.5	-160 µm	10 x 10	5.2
2	3.5	-160 µm	16 x 10	7.3
3	3.5	-160 µm	22 x 10	9.1
4	3.5	-160 µm	28 x 10	7.6
5	3.5	-160 µm	34 x 10	6.3

From the 1st to the 3rd spots, the depths of the spots increased with the increasing of polishing time. After the 4th spot, the depths decreased showing a potential tool wear.

Figure 55 shows the form accuracy of each polishing spot.

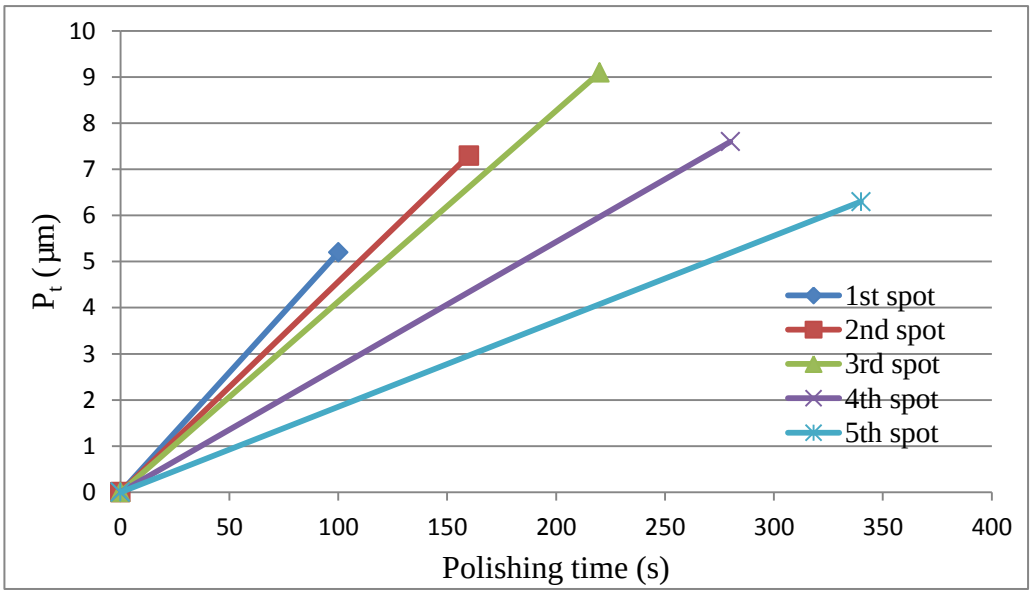

Figure 55: Form accuracy of each polishing spot

The total pitch polishing time before the tool wore out was about 220s. The material remove rate decreased because the tool wore out and became flat from the 4th spot. The polishing force recorded did not reduce when polishing the 4th and the 5th spots. Therefore, this could not be selected as a parameter to judge the condition of the tool wear. Figure 56 shows the surface of pitch tool after polishing spots.

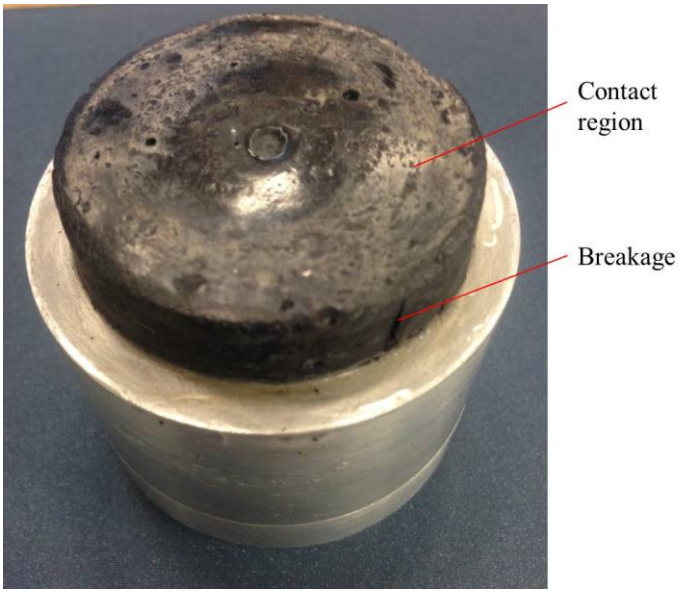

Figure 56: Pitch tool after spots polishing

The tool became flat and wore out near the edge which caused the breakage of the tool. Therefore, a smaller tool angle, 3 degree was selected to polish grooves.

4.5 Grooves polished by polyurethane tool

Grooves were polished on lapped sample to measure the depth of polishing which is a mean calculation of the material remove rate and the Preston coefficient. Three grooves (10 runs, 15 runs and 20 runs of polishing) were manufactured using a 3.5 degree tool angle, 100N polishing force and 5 mm/s polishing speed (see Figure 57).

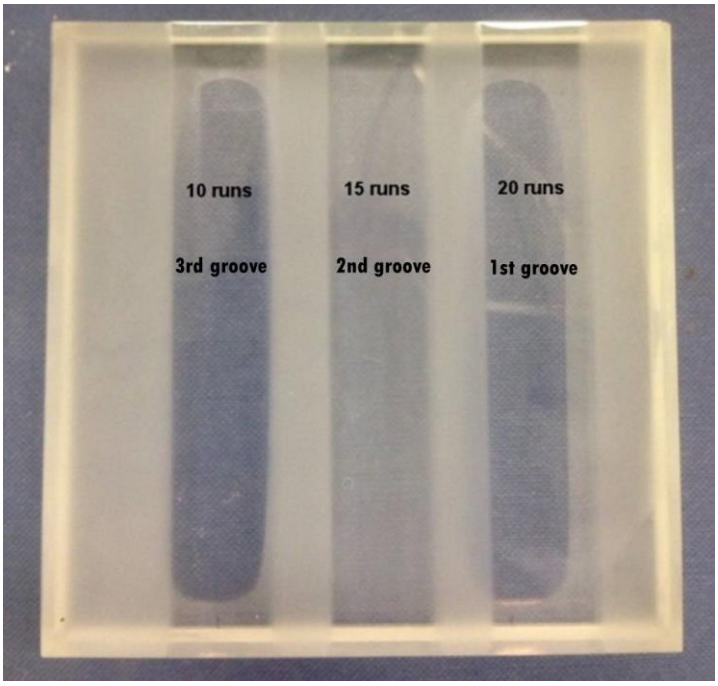

Figure 57: Polished grooves after different number of runs

4.5.1 Polishing force

The polishing force was recorded during the 1st, 5th, 11th, 16th and 20th run (see Figure 58 and the section of A9.4). Figure 58 shows the polishing force of the first run.

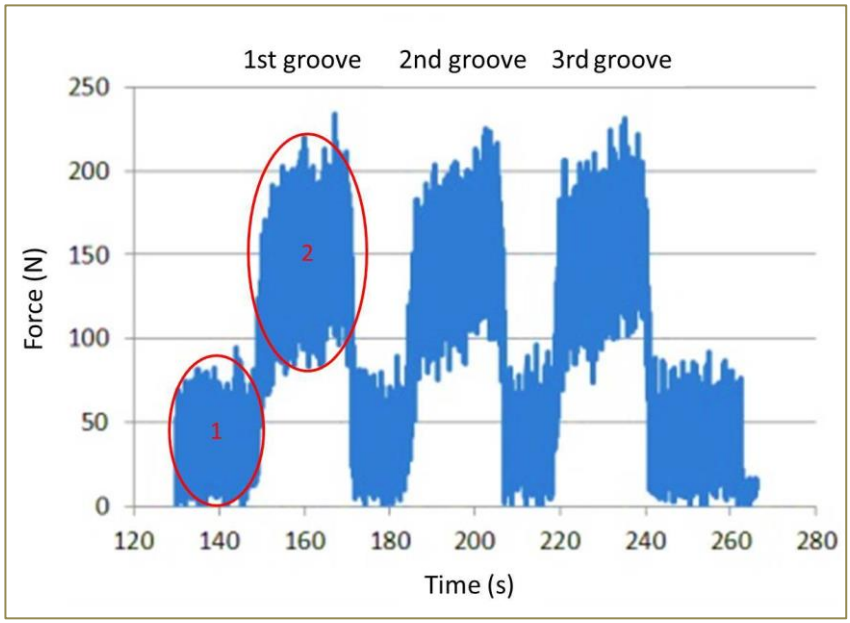

Figure 58: Polishing force - 3 grooves - the 1st run

From the first region, when there was no contact between the tool and the part, the influence of the polishing slurry and the tool rotation was on average 40N. For the second region, the average polishing force was about 110N eliminating the influence of the polishing slurry and the tool rotation.
Figure 59 shows the record of polishing force from the 1st run to the 20th run.

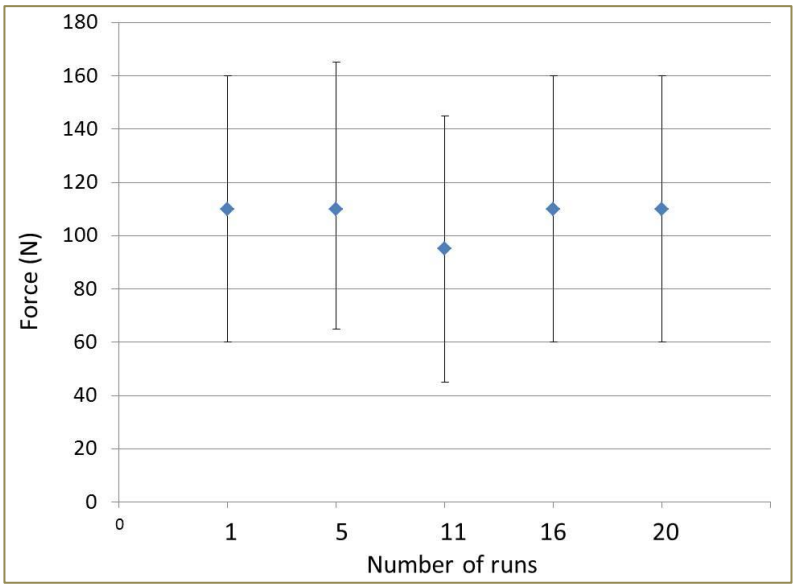

Figure 59: Polishing force after different number of runs

The polishing force was constant except for the 11th run where the force was about 15N lower than the others. This means that the tool does not wear out during a short time polishing.

4.5.2 Cross sections of grooves

The cross sections of the middle of the grooves were measured using the Talysurf profilometer to calculate the material remove rate and the Preston coefficient. Figure 60 shows the measurement results of cross sections.

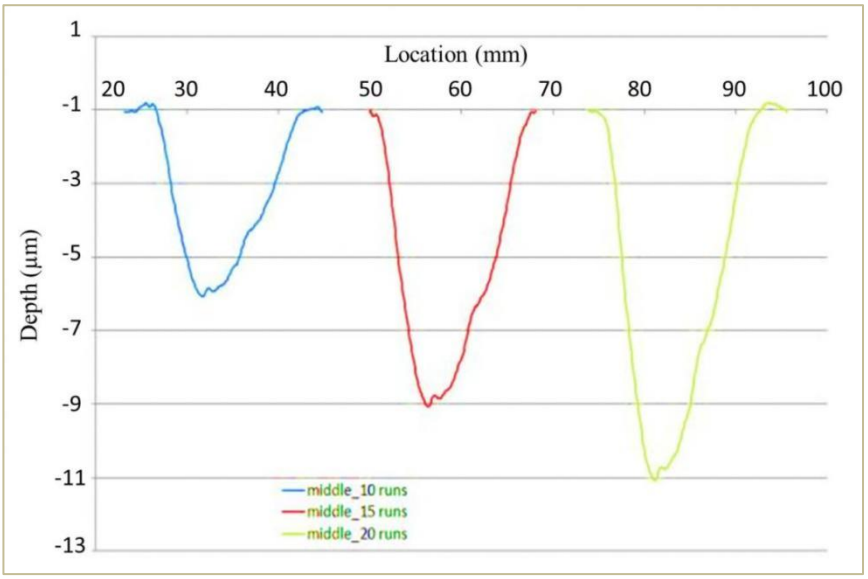

Figure 60: Cross sections through the middle of the grooves

4.5.3 Material Remove Rate

The method of Full Width Half Maximum (FWHM) was employed to calculate the size of the cross section. Equation 4.5.3.1 shows the calculation of the size, where S_c means the size of cross section, D_c means the depth of the cross section and the W_c means the width of the cross section.

$$S_c = D_c * W_c / 2 \quad \text{(Equation 4.5.3.1)}$$

Equation 4.5.3.2 illustrates the calculation of material remove rate, where MRR_{1U} means the material remove rate of ULE, S_c means the size of cross section, L_s means the length of the groove, t means polishing time per run and N_{runs} means the number of runs.

$$MRR_{1U} = S_c * L_s / t / N_{runs} \quad \text{(Equation 4.5.3.2)}$$

Table 25 shows the results of the size of cross sections and the material remove rate of robot polishing grooves.

Table 25: Material remove rate and Preston coefficient of robot polishing grooves

N_{runs}	$S_c(mm^2)$	MRR_{1U} (mm^3/s)	Preston coefficient (m^2/N)
10 runs	3.83×10^{-2}	1.91×10^{-3}	3.03×10^{-13}
15 runs	6.40×10^{-2}	2.13×10^{-3}	3.38×10^{-13}
20 runs	7.50×10^{-2}	1.88×10^{-3}	2.98×10^{-13}

It can be calculated from the table that the average material removal rate of ULE was 1.97×10^{-3} mm^3/s.

4.5.4 Preston coefficient

According to the Preston equation (see Equation 1.3.1.1), $K_e = MRR/P/V$, Where K_e (mm^2/N) is an all-purpose coefficient, MRR (mm/s) is the material removal rate, P (N/mm^2) is the downward pressure and V (mm/s) is the relative velocity over the workpiece surface.

For the 2nd groove after 15 runs polishing, with $MRR = MRR_1/S = 2.13 \times 10^{-3}$ mm^3/s/ (8mm x 10mm) = 2.66×10^{-5} mm/s, P=110N/ (3.14×8^2) mm^2=0.55 N/mm^2, V= 5mm/s.

Then, $K_{poly} = 0.97 \times 10^{-13}$ m^2/N.

4.5.5 Edge effects

The form accuracy (P_t) of the grooves was measured to analyse the edge effects of polishing (The measurement result were recorded in the section of A9.5). Figure 61 shows the tendency line of different grooves' form accuracy.

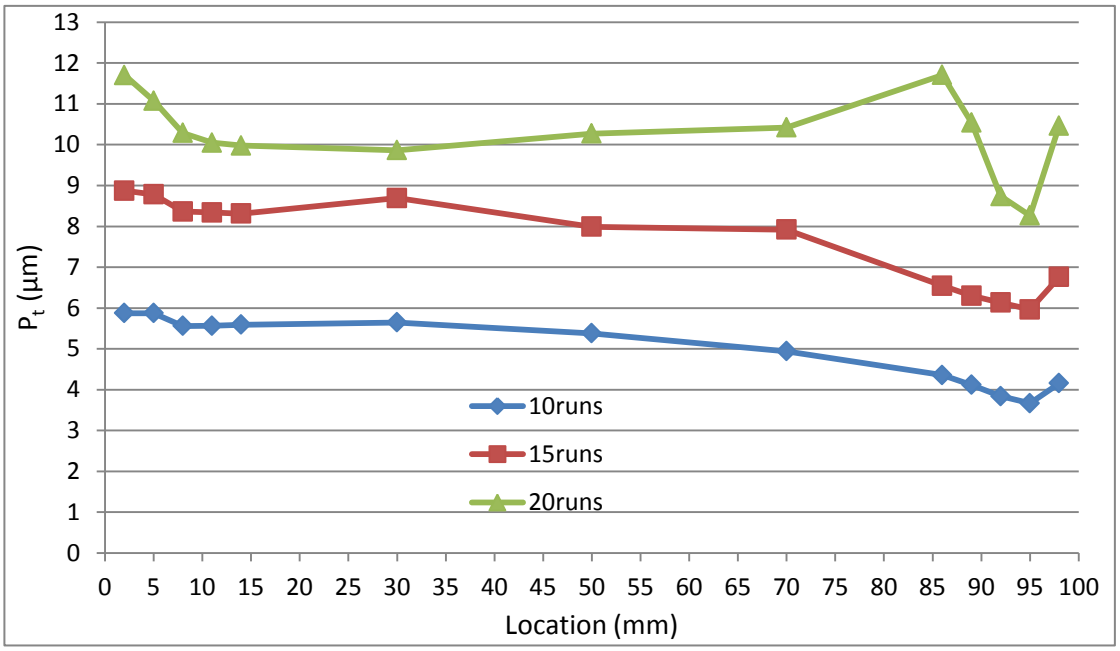

Figure 61: Tendency line of different grooves' form accuracy

From the edge (70mm to 95mm) of the 2nd groove (after 15 runs of polishing), less material was removed away than in other area. Table 26 shows the edge's Z position of the 2nd groove.

Table 26: Edge effect of 2nd groove after 15 runs of polishing

Location(mm)	P_t (µm)	Z position (µm)
70	8	-500
95	6	-375

Table 27 shows the compensation data which was used for the raster polishing process of 100mm square part.

Table 27: Compensation of the tool effect

Location (mm)	68	75	82	89	96
Z position (µm)	-500	-468	-437	-406	-375
Compensation (µm)	0	-31	-62	-93	-124

4.6 Robot polishing 100mm square sample

4.6.1 Robot Polishing of lapped ULE sample

4.6.1.1Form accuracy and roughness measurement before polishing

One 100mm square ULE sample was lapped following samples preparation methodology (section 3.2.4.1) to prepare for robot polishing. The form accuracy and roughness which were measured according to the method in Figure 27 after lapping process were recorded in the section of A9.6. The form accuracy (P_t) ranged from 2.2µm to 2.6µm and the surface roughness (R_a) was 230- 240nm.

4.6.1.2 Polishing force

Figure 62 illustrates the force of the second run during robot polishing the 100mm square lapped sample.

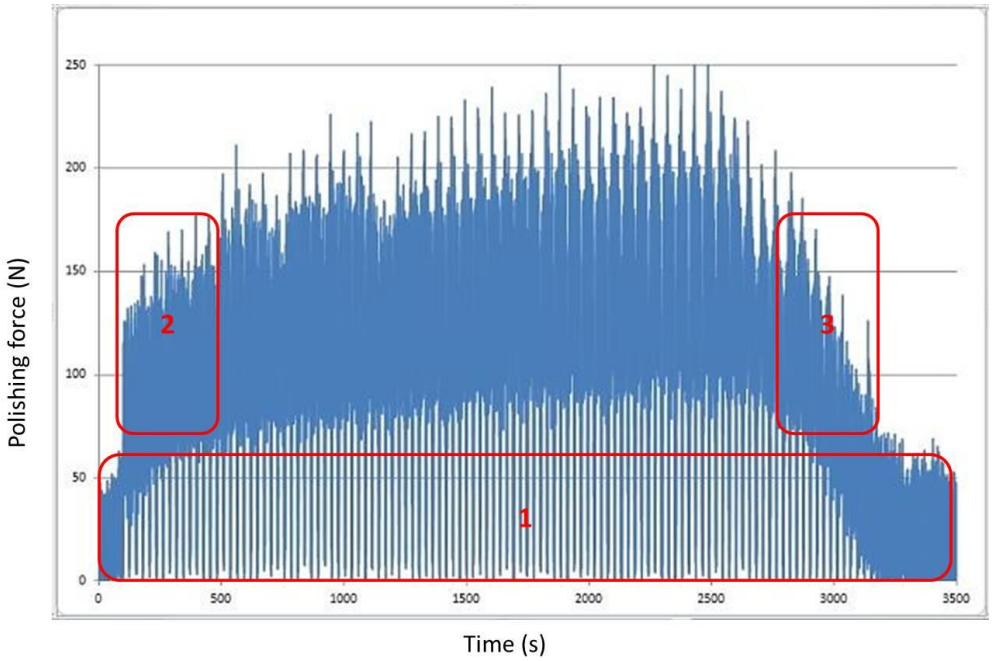

Figure 62： Robot polishing force - 100 mm square lapped sample- 2nd run

The first area shows that the average influences of polishing slurry and tool rotation was about 30N. The increase and the decrease of forces in the second and the third areas show the interaction between the tool and the sample from no contact to full contact and vice versa. The average polishing force remained at about 100N when subtracting the influence of the polishing slurry and tool rotation.

4.6.1.3 Form accuracy and roughness measurement after robot polishing

Figure 63 shows the measurement method of lapped sample after robot polishing where the 1, 2, 3, 4, 5, 6 and 7 mean the measurement direction comparing to the polishing direction and the raster direction. The measurement result of form accuracy and roughness after robot polishing is recorded in the section of A9.6.

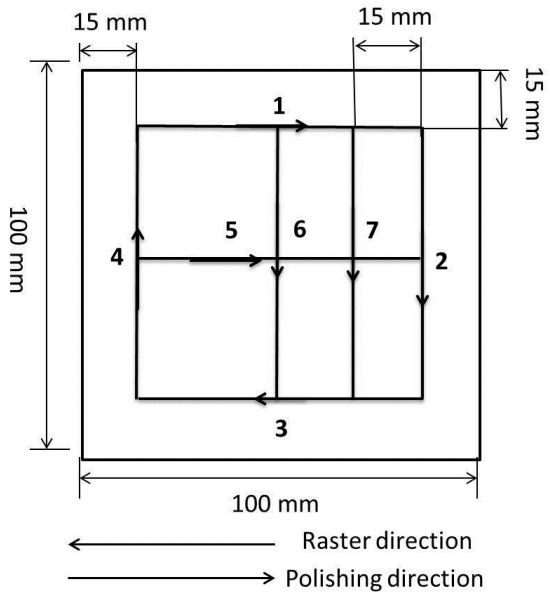

Figure 63: Measurement method of 100mm square lapped sample after robot polishing

Figure 64 illustrates the development of form accuracy from the result of lapped surface to the result after 1 and 7 robot polishing runs.

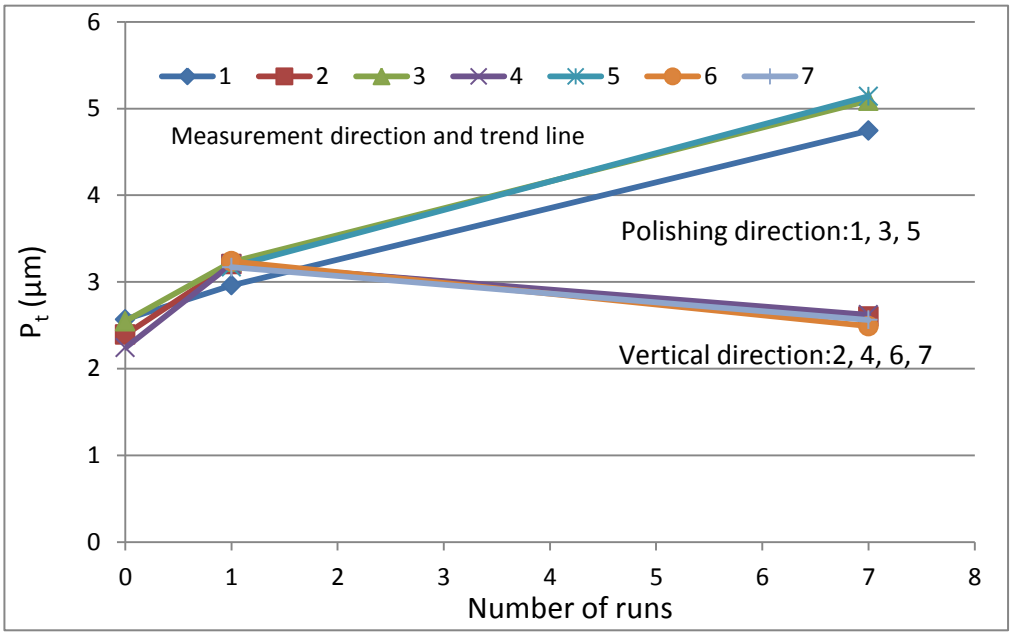

Figure 64: Development of form accuracy from lapping to robot polishing

The form accuracy decreased after one polishing run in both polishing and vertical directions. After 7 runs, it worsened in the polishing direction while improving in the vertical direction.

Figure 65 illustrates the surface roughness results before polishing and after 1 and 7 robot polishing runs.

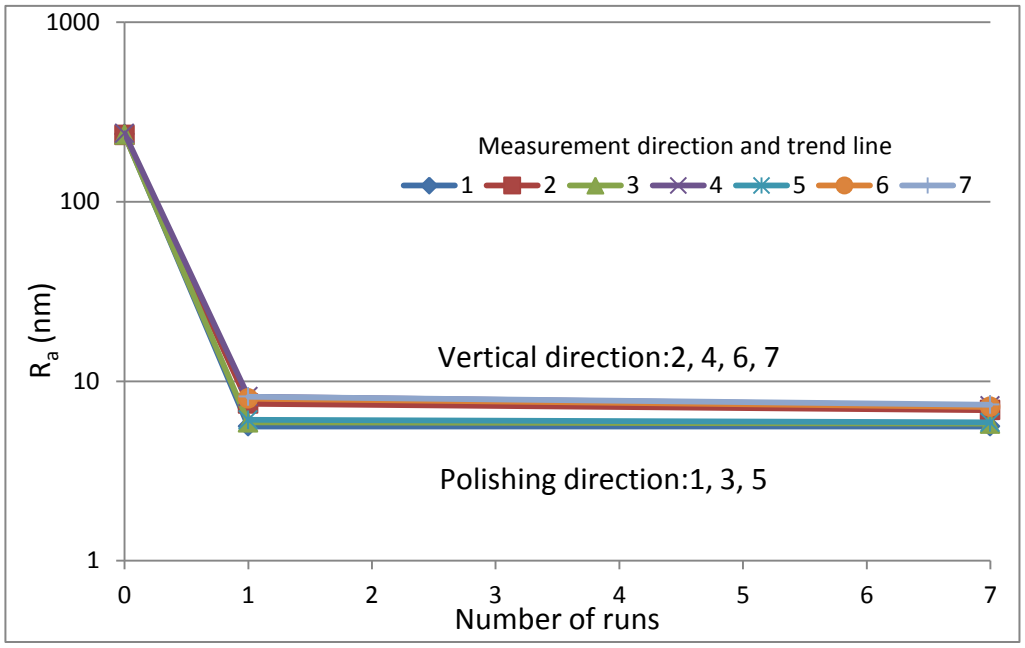

Figure 65: Improvement of roughness during robot polishing for lapped sample

Surface roughness (R_a) improved significantly after one polishing run by a factor of 30. After 7 polishing runs, in the polishing direction, the R_a improved by less than 0.2nm to within 6nm. The surface roughness, in the vertical direction, improved more (about 0.8nm) to within 7.5 nm but remained worse than in the polishing direction.

4.6.1.4 Edge effect

Figure 66 shows the edge effect of the part after 7 robot polishing runs.

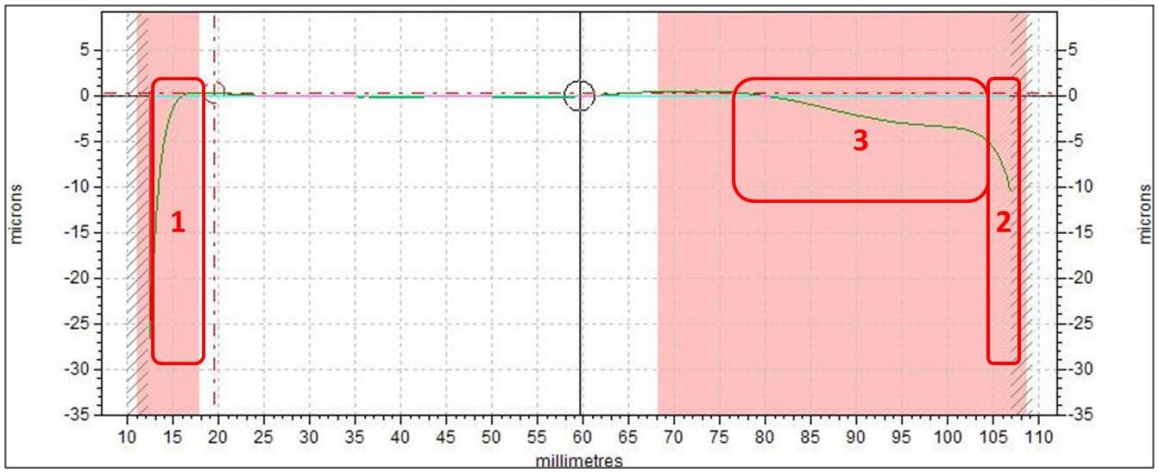

Figure 66: Form accuracy after 7 robot polishing runs -measurement direction 3

The first and the second area show the edge roll-off after 7 robot polishing runs. The third area (68mm to 96mm on the part), much more material was removed than anticipated, it was decided that values used for compensating the edge effect highlighted would be divided by two. Table 28 illustrates the modified compensation of the tool effect.

Table 28: Modified compensation of the tool effect

Location (mm)	68	75	82	89	96
Compensation (μm)	0	-15.5	-31	-46.5	-62

4.6.2 Robot polishing of ground fused silica sample

Both sides of a fused silica sample were ground using the BoX grinding machine following procedure described in section 3.2.4.2. The form accuracy and roughness after the grinding process, which were measured according to the method in Figure 28, were recorded in the section of A9.7. The surface qualities of ground side1 were: The form accuracy (P_t) ranged from 1.4μm to 3.0μm and the roughness (R_a) ranged from 73nm to 115nm. The surface qualities of ground side2 were: the form accuracy (P_t) ranged from 0.8μm to 1.3μm and the roughness (R_a) ranged from 56nm to 75nm.

4.6.2.1 Polishing half part of the ground sample

Figure 67 show the result of polishing half part of ground sample to calculate the material removed after 6 robot neutral polishing runs.

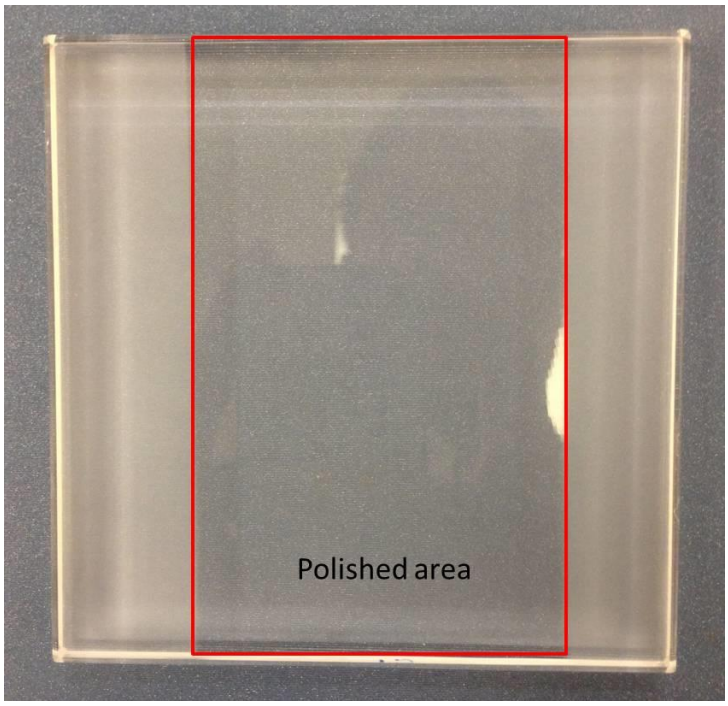

Figure 67： Polishing half part of the ground sample

Figure 68 show the form accuracy of polished groove. The surface profile (P_t) of the polished groove was 21.5μm.

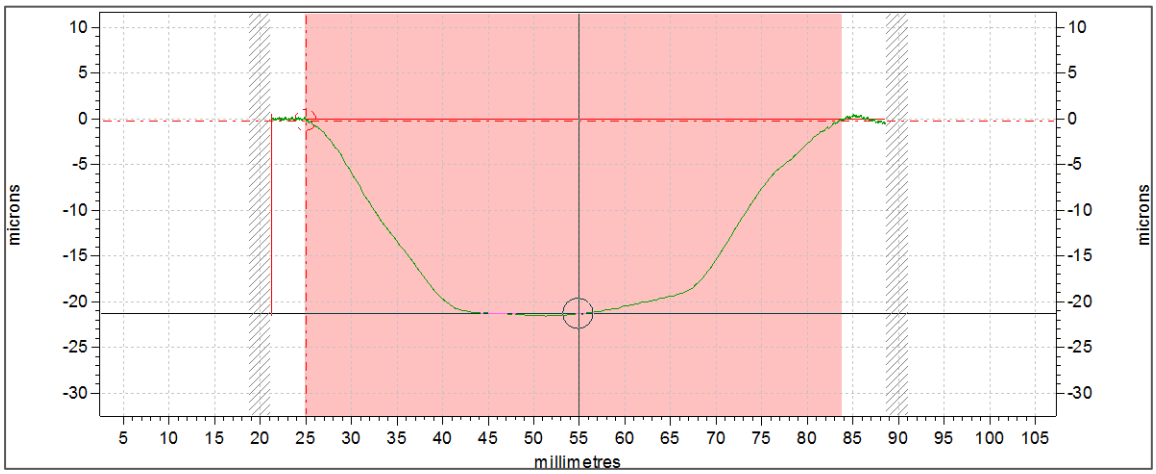

Figure 68: Form accuracy of the polished groove

The polished area was from 20mm to 80mm in the Y coordinate. The width for a constant groove was 20mm which was used to calculate the full polishing length in Y coordinate when programming to polish the full sample.

4.6.2.2 Polishing along the direction of grinding cusps

Figure 69 shows the measurement method after robot polishing along grinding cusp (side 1) where 1, 2, 3, 4, 5 and 6 mean measurement direction. The measurement results were recorded in the section of A9.7.

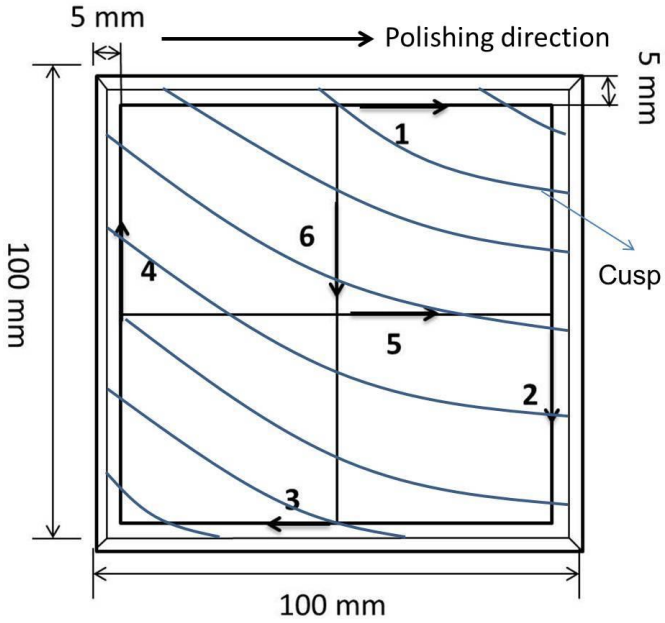

Figure 69: Measurement method of 100mm square ground sample after robot polishing - side 1

Figure 70 illustrates the development of form accuracy from the result of ground surface to the result after 6 runs robot polishing.

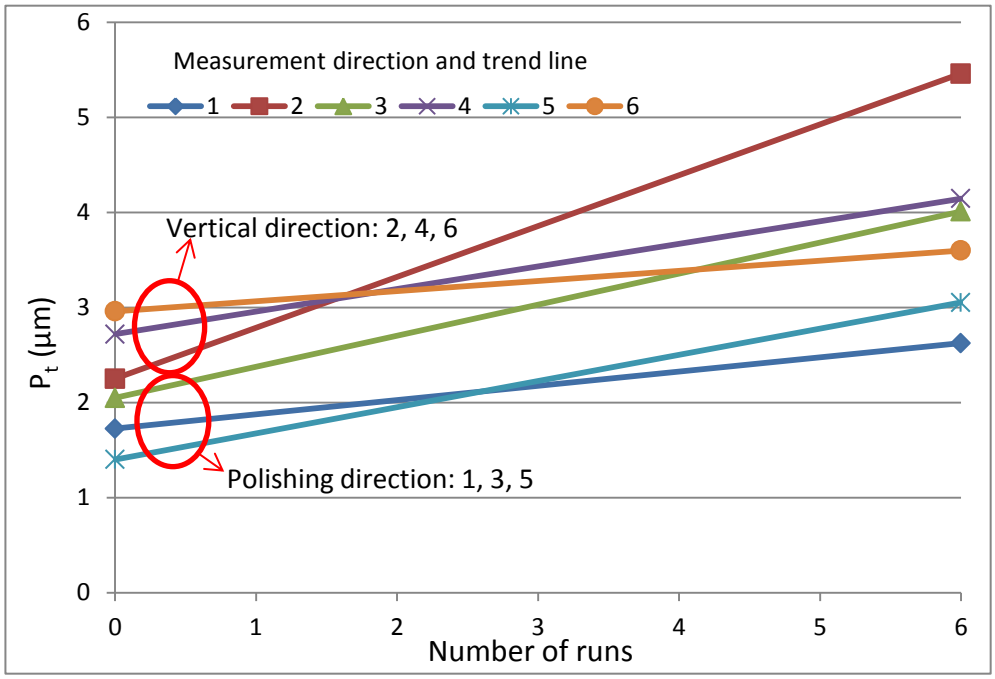

Figure 70: Development of form accuracy from grinding to robot polishing- side 1

The form accuracy decreased from the result of grinding process to robot polishing for both polishing direction and vertical direction. Before the polishing process, the form accuracy (P_t) along grinding cusps (1.4 µm-2.0 µm) was better than the value vertical to grinding cusps (2.2 µm-3.0 µm). After 6 robot polishing runs, this trend remained with P_t =2.6-4.0 µm and P_t =3.6-5.5 µm respectively except measurement direction 3.
Figure 71 illustrates the improvement of roughness before and after robot polishing.

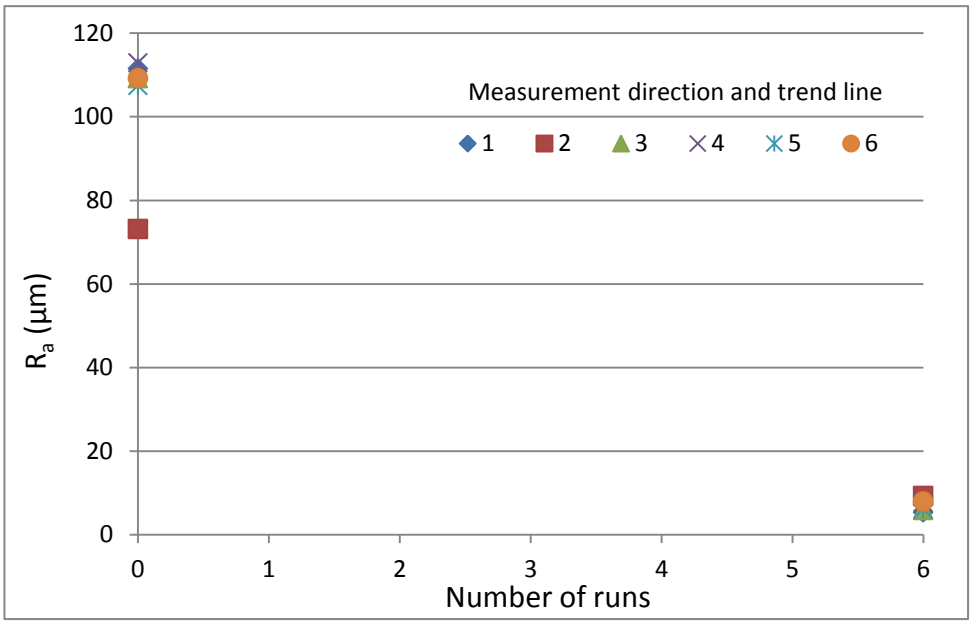

Figure 71: Improvement of roughness from grinding to robot polishing- side 1

The roughness (R_a) was improved from 73nm -115nm before polishing to less than 10nm after 6 runs robot polishing. The surface roughness parallel to polishing direction ranged

from 5.3nm to 6.1nm while the roughness vertical to polishing direction ranged from 7.7nm to 9.2nm.

Figure 72 shows the form accuracy of measurement direction 3 after 6 runs polishing.

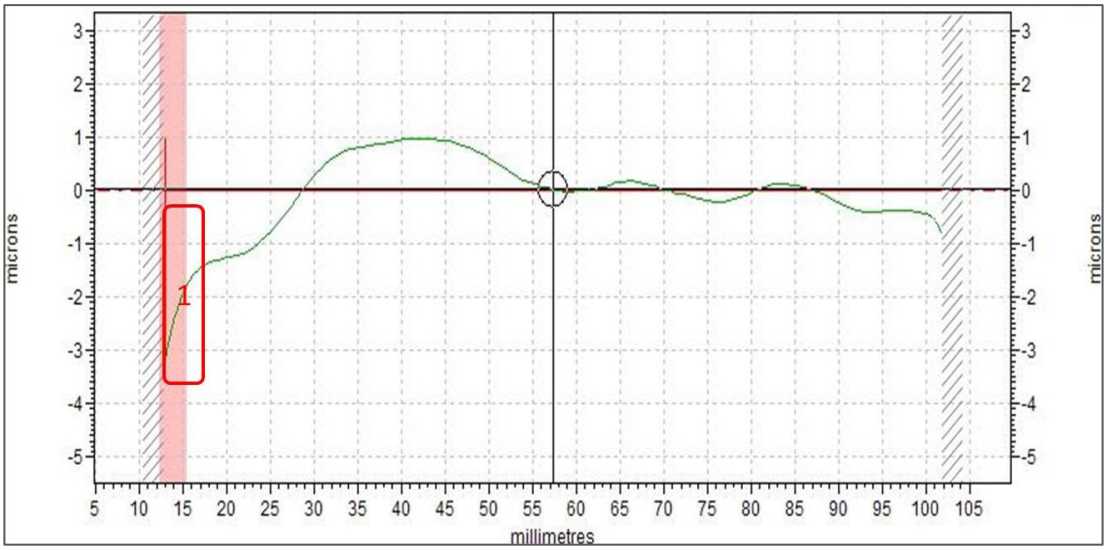

Figure 72: Form accuracy after 6 runs robot polishing-measurement direction 3

The first area of the part shows the edge roll-off. As can be seen from 72mm to 100mm of Figure 71 (68mm to 96mm on the part), the modified compensation of tool effect in Table 28 has worked which was improved by a factor of 5.

4.6.2.3 Polishing vertical to the direction of grinding cusps

Figure 73 shows the measurement method after robot polishing vertical to grinding cusp (side 2) where 1, 2, 3, 4, 5 and 6 mean measurement direction. The measurement results were recorded in the section of A9.7.

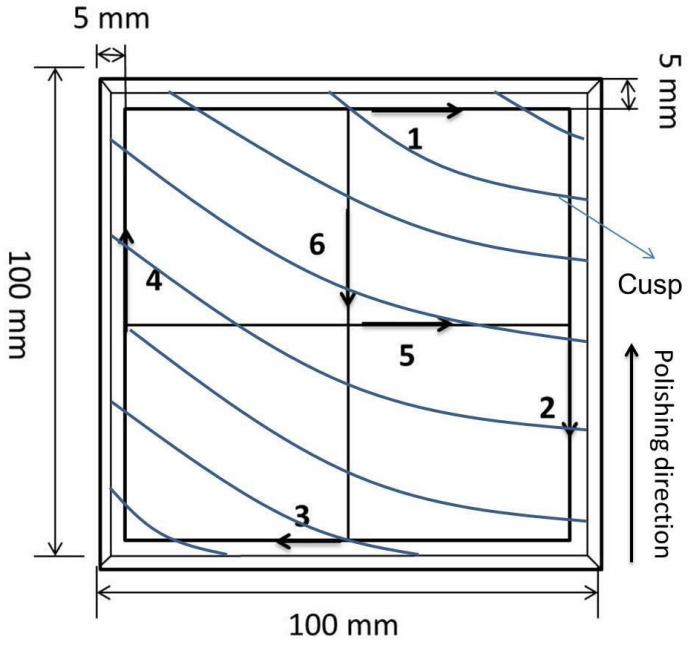

Figure 73: Measurement method of 100mm square ground sample after robot polishing - side 2

Figure 74 illustrates the development of form accuracy from the result of ground surface to the result after 6 robot polishing runs.

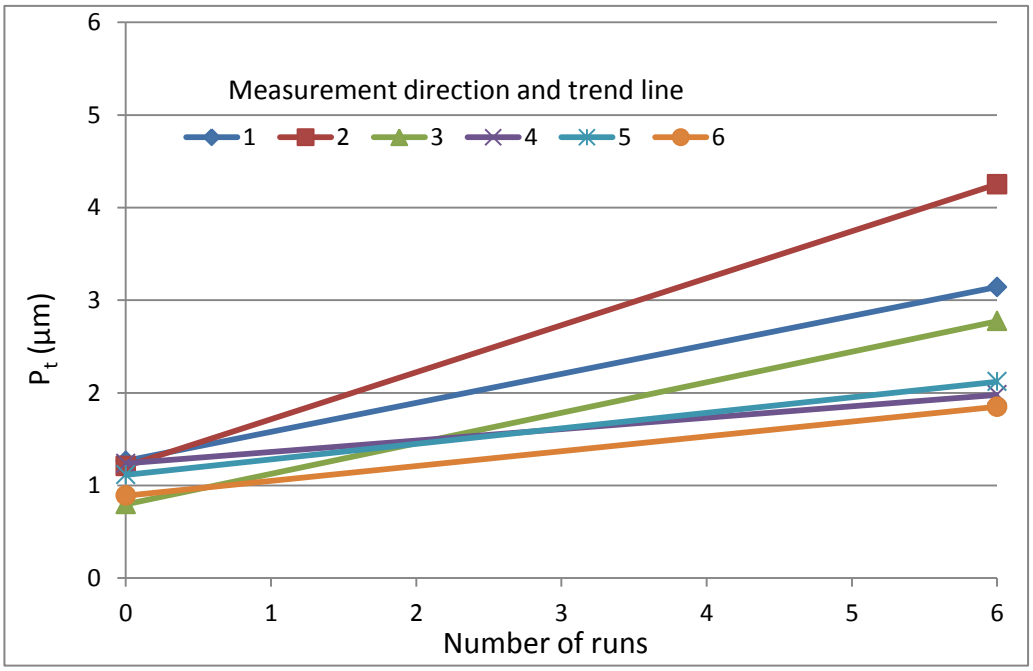

Figure 74: Development of form accuracy from grinding to robot polishing- side 2

The form accuracy (P_t) decreased from 0.8µm-1.3µm before polishing process to 1.8µm-4.3µm after 6 robot polishing runs for both polishing direction and vertical direction.

Figure 75 illustrates the improvement of roughness before and after robot polishing.

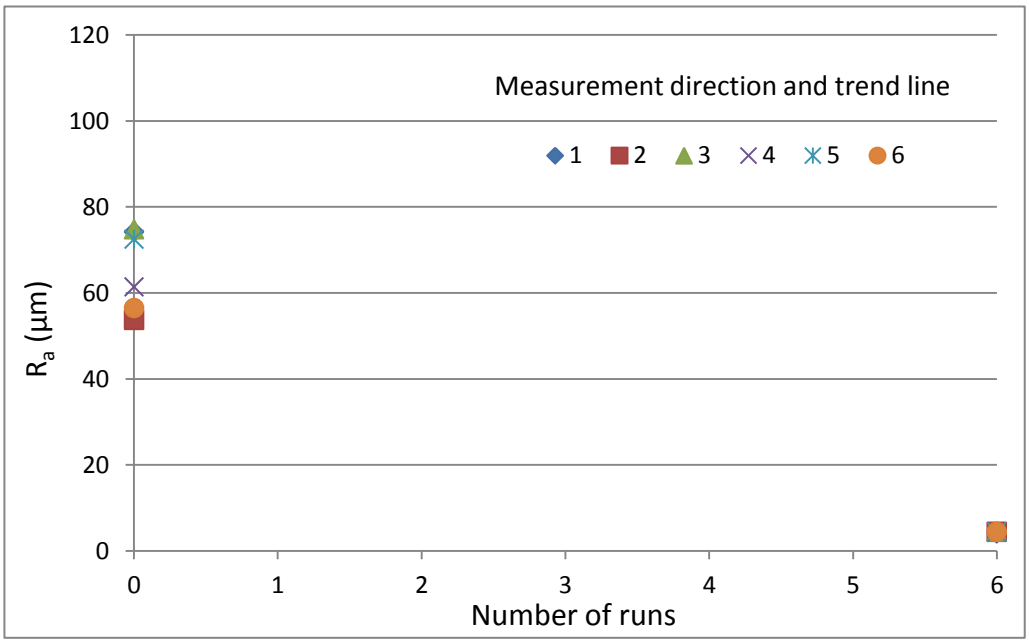

Figure 75: Improvement of roughness from grinding to robot polishing- side 2

Before polishing process, the roughness along grinding cusp (72nm-75nm) was worse than the roughness vertical grinding cusp (53nm-62nm). The roughness parallel and vertical polishing directions were improved to almost the same which were ranged from 4.0nm to 4.5nm.

4.6.3 Polishing time

The polishing time of one robot polishing run on a 100mm square part could be calculated according to the experiment procedure 3.2.6.

$$T_1=LW/ (V_p \times S_p) \qquad \text{(Equation 4.6.3.1)}$$

Equation 4.6.3.1 shows the calculation of the polishing time of one run (T_1), where L and W are the length and width of the polishing area, V_p is the polishing speed, S_p is polishing step. Then, T_1=125mm x 125mm/ (5mm/s x 1mm) = 3125s=52 minutes. The total polishing time for 6 runs robot polishing the ground part was 312 minutes.

4.7 Robot polishing 400mm square ULE component

To demonstrate the scalability of polishing process developed, a 400mm square ULE component was ground using the BoX grinding machine with 3000mm curvature sphere.

4.7.1 Measurement results before polishing

Figure 76 shows the measuring process of the 400mm square ground part according to the experiment procedure in section 3.2.4.3.

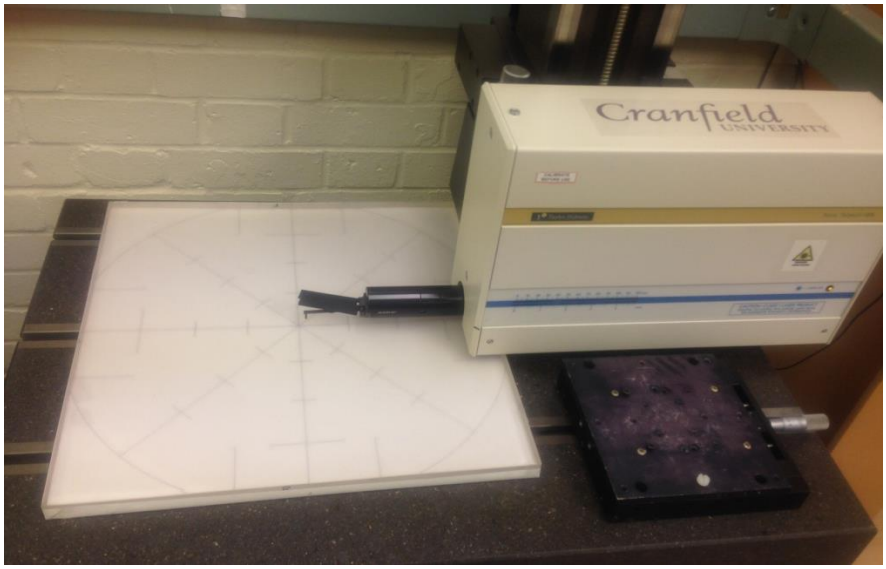

Figure 76: Measuring the 400mm square part using Talysurf profilometer

The fixed radius of the LS Arc absolute measurement was set to 3000mm which was the programmed radius of curvature of the sphere ground on the 400mm square ULE part. The form accuracy and roughness of each measurement direction were recorded in the section of A9.8.

4.7.1.1 Grinding cusp measurement

Figure 77 and Figure 78 show the cusp condition vertical and parallel polishing direction after grinding process respectively.

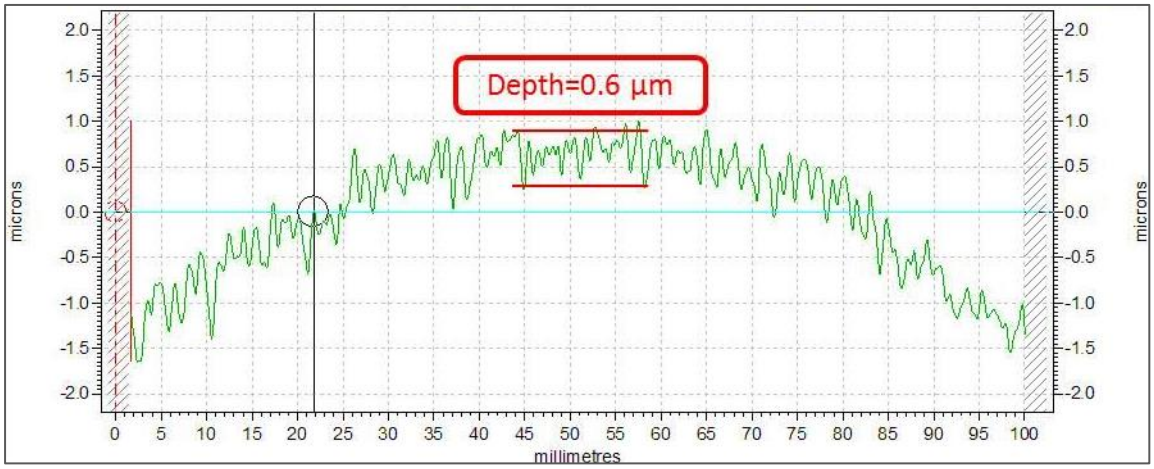

Figure 77: Cusp condition before polishing-vertical polishing direction (direction 1-3)

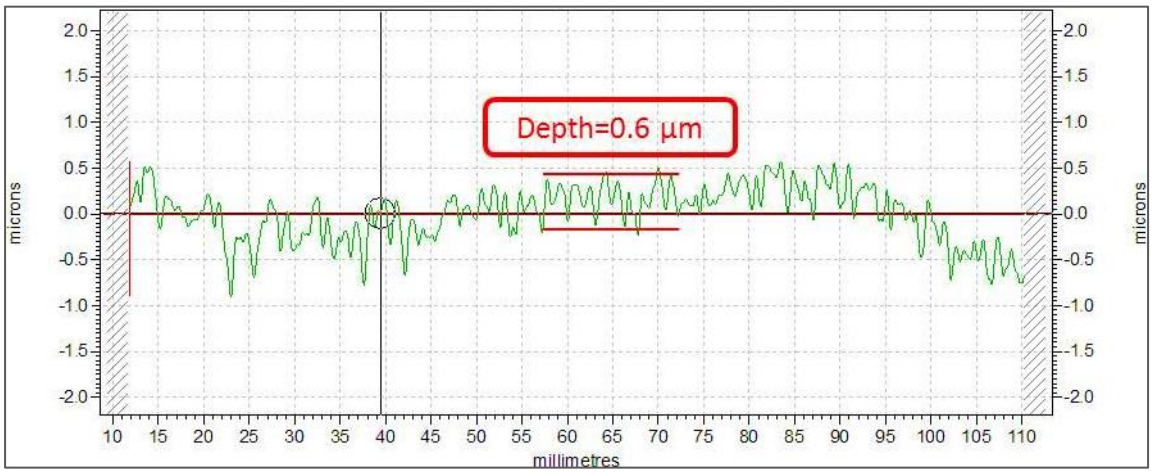

Figure 78: Cusp condition before polishing-parallel polishing direction (direction 11-13)

The depth of grinding cusp which has to be removed was 0.6 µm (P_t).

4.7.1.2 Surface roughness measurement

Figure 79 shows the different area's roughness of the 400mm square part before polishing.

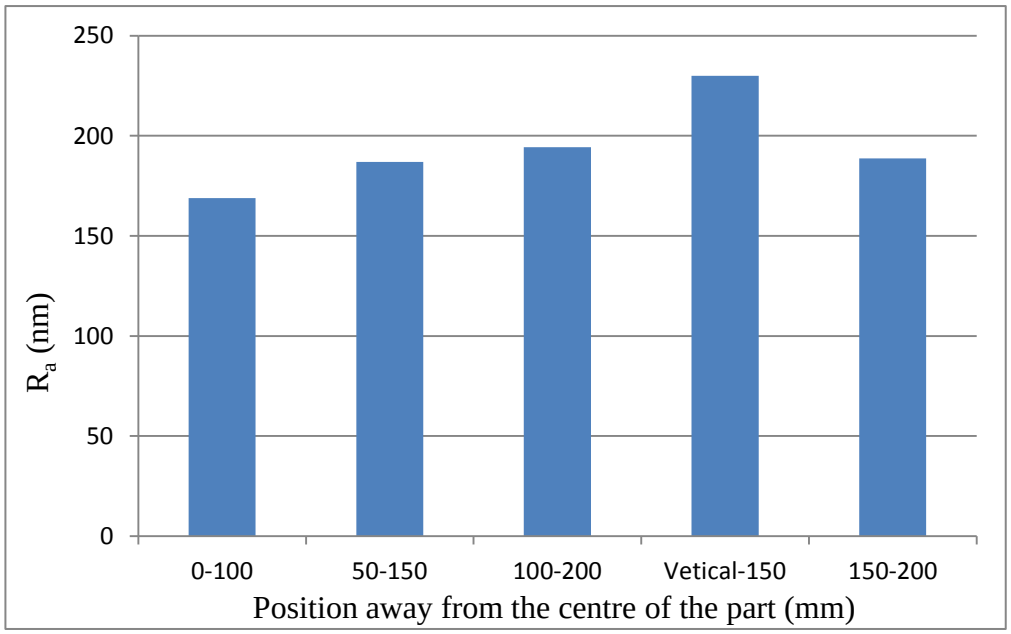

Figure 79: Roughness of the 400mm square part before robot polishing

The roughness of the ground part degraded from the position near the centre (R_a=168nm at the position 0 to 100mm near the centre) to the position near edge (R_a=194 nm at the position 100 to 200 near the centre). The area which had the worst roughness was 100 to 150mm near the centre. The roughness of the part should be improved to within 10nm (R_a) after robot neutral polishing according to the objective1 of the project.

4.7.2 Robot polishing results

Figure 80 shows the process of robot polishing the 400mm square ground ULE part using the polyurethane polishing tool and cerium oxide polishing slurry.

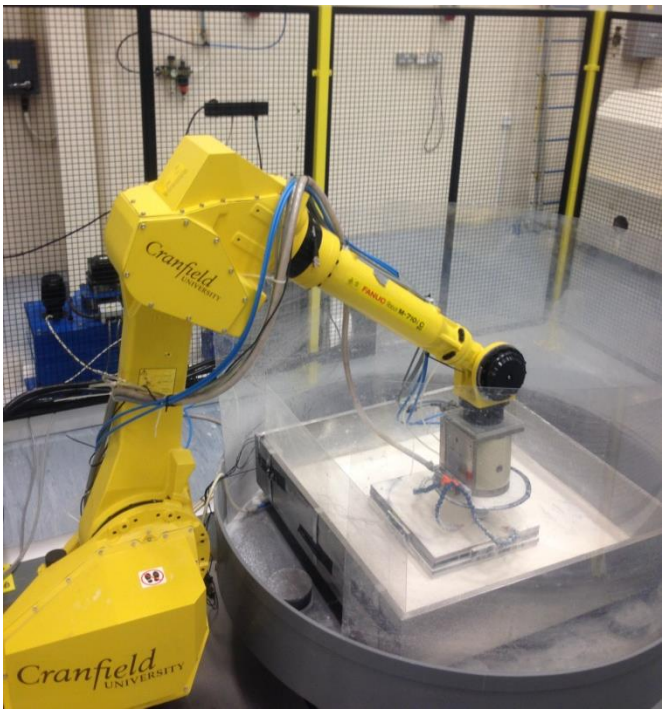

Figure 80: Robot polishing 400mm square ground ULE part

4.7.2.1 Measurement result after 4 robot polishing runs

Figure 81 shows the comparison of the 400mm square part before and after 4 robot polishing runs.

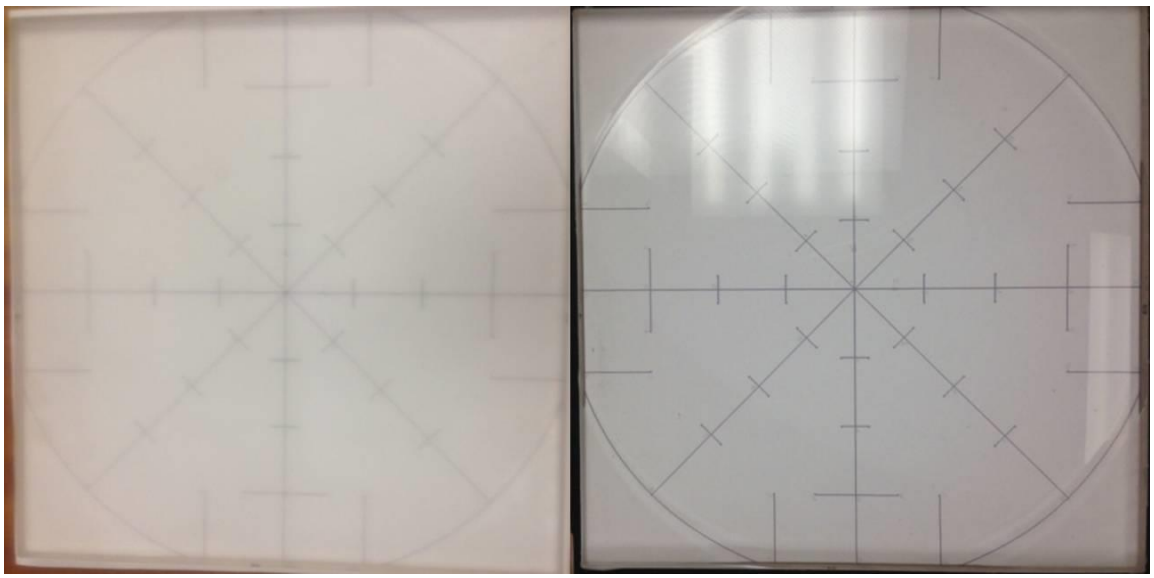

Figure 81: 400mm square part before and after 4 robot polishing runs

The form accuracy and roughness of each measurement direction after 4 robot polishing runs were recorded in the section of A9.8. Figure 82 shows the cusp condition after 4 robot polishing runs, the measurement was vertical to the polishing direction.

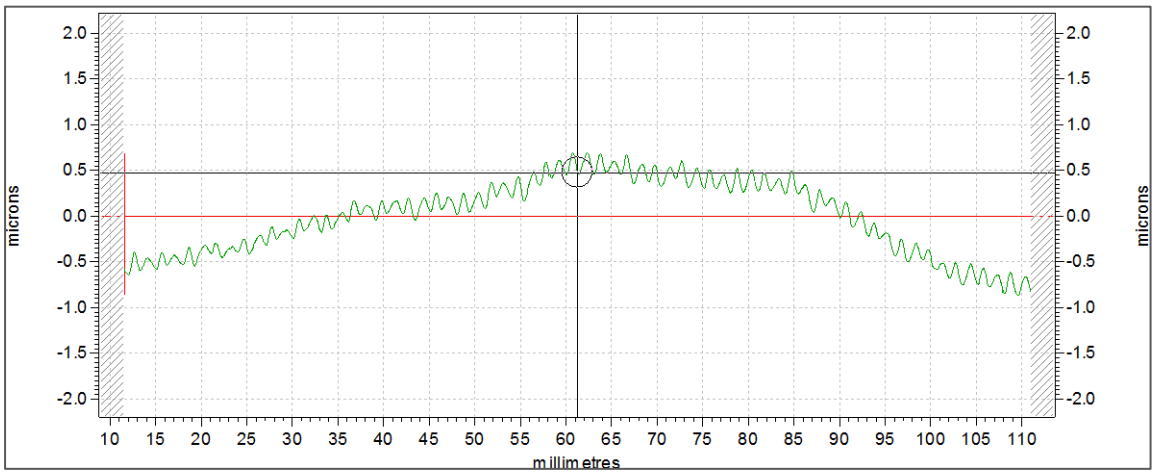

Figure 82: Cusp condition after 4 polishing runs -vertical polishing direction (direction 1-3)

Figure 83 shows the cusp condition after 4 robot polishing runs, the measurement was parallel to the polishing direction.

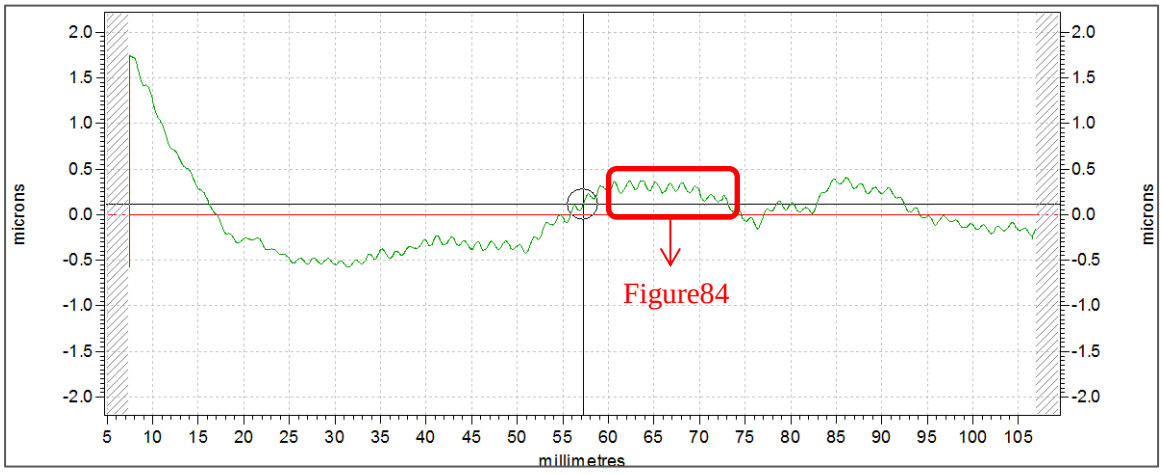

Figure 83: Cusp condition after 4 polishing runs -parallel polishing direction (direction 11-13)

Figure 84 shows the detailed information of the square area in Figure 82.

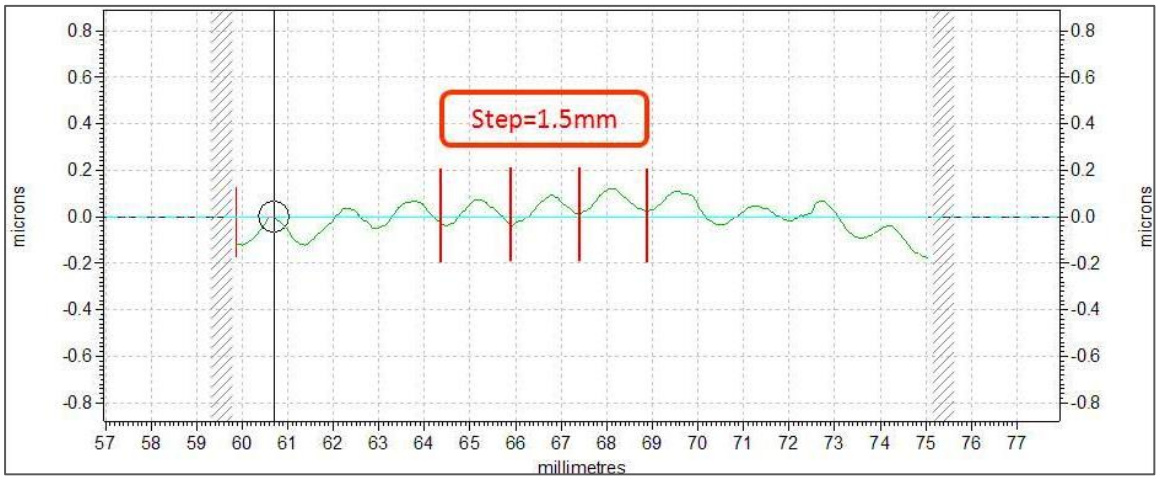

Figure 84: Step of cusp after 4 robot polishing runs (Measurement direction 11-13)

The grinding cusp still remained as the valley of the grooves was 1.5mm which was generated by the grinding process. However, they were reduced by a factor of 4. The grooves in Figure 82 were generated by the function of polishing process and grinding process together as only grinding cusps could be observed.
Figure 85 shows the roughness improvement before polishing and after 4 polishing runs at different area of the 400mm square part.

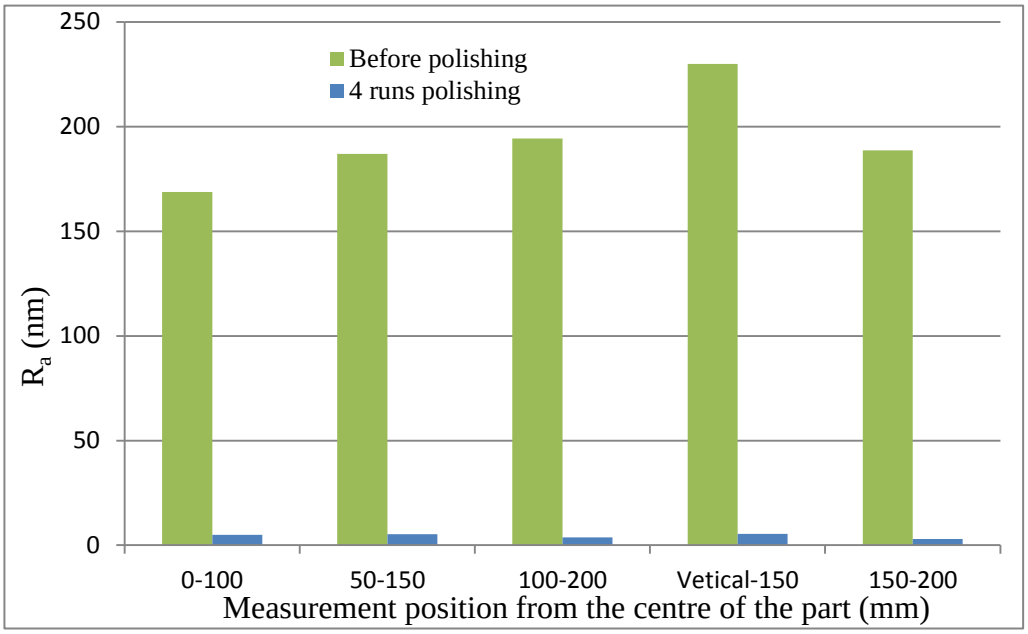

Figure 85: Roughness improvement before polishing and after 4 polishing runs

The roughness was improved by a factor of 38 to within 6nm (R_a) after 4 robot polishing runs.

4.7.2.2 Measurement result after 9 runs robot polishing
Figure 86 shows the comparison of the 400mm square part after 4 runs robot polishing and after 9 runs robot polishing.

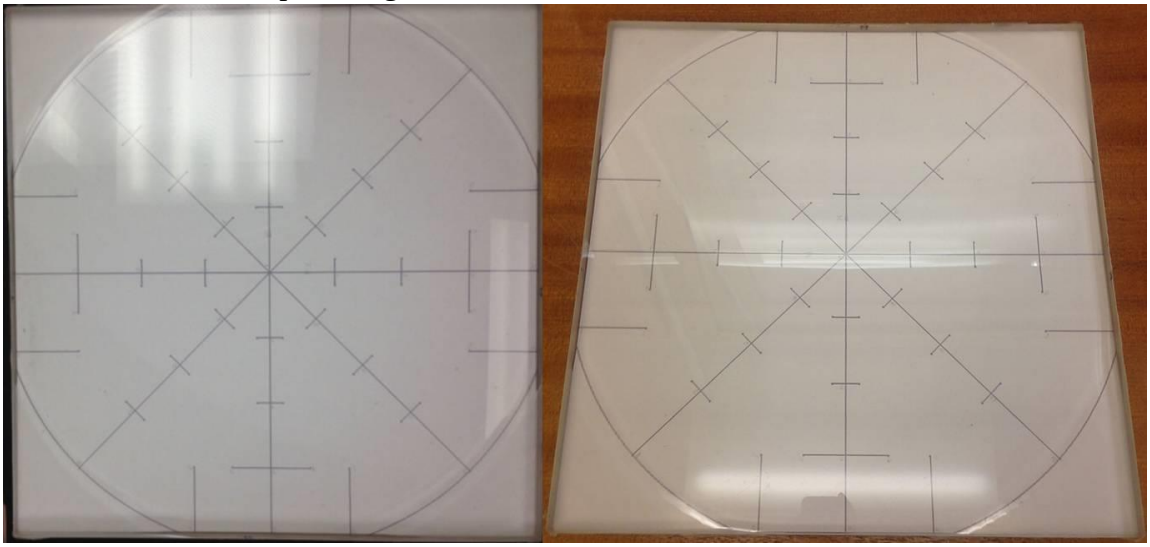

Figure 86: 400mm square part after 4 and 9 robot polishing runs

The form accuracy and roughness of each measurement direction after 9 robot polishing runs were recorded in the section of A9.8.
Figure 87 shows the cusp condition after 9 robot polishing runs. It was the measurement vertical to the polishing direction.

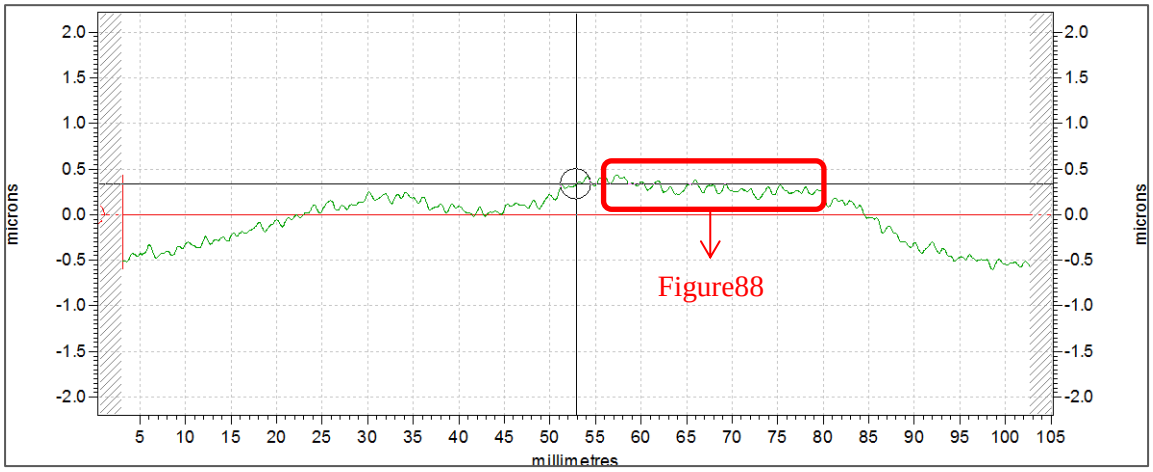

Figure 87: Cusp condition after 9 polishing runs -vertical polishing direction (direction 1-3)

Figure 88 shows the detailed information of polishing grooves.

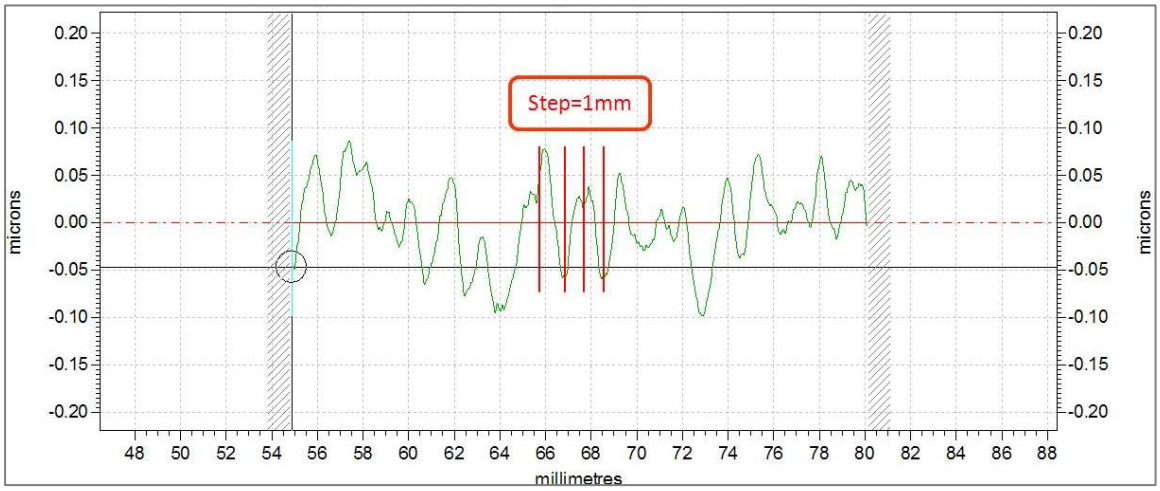

Figure 88: Step of polishing lines after 9 robot polishing runs (Measurement direction 1-3)

The grooves were only generated by the polishing process because the valley of grooves was 1mm which was produced by polishing every 1mm. The surface profile (P_t) of the polishing grooves was about 0.1 μm

Figure 89 shows the cusp condition after 9 robot polishing runs. It was the measurement along the polishing direction.

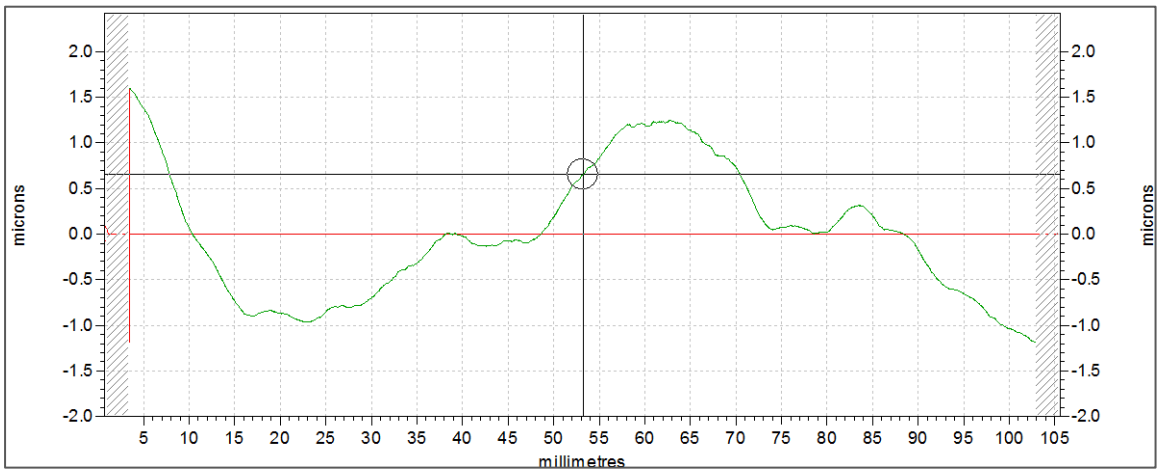

Figure 89: Cusp condition after 9 polishing runs -parallel polishing direction (direction 11-13)

The grinding cusps were removed along the polishing direction so that the robot polishing was stopped at this stage to prevent producing deeper polishing grooves. Figure 87 shows the polishing grooves left on the surface of the part.

Figure 90 shows the roughness development after 4 and 9 polishing runs at different area of the 400mm square part.

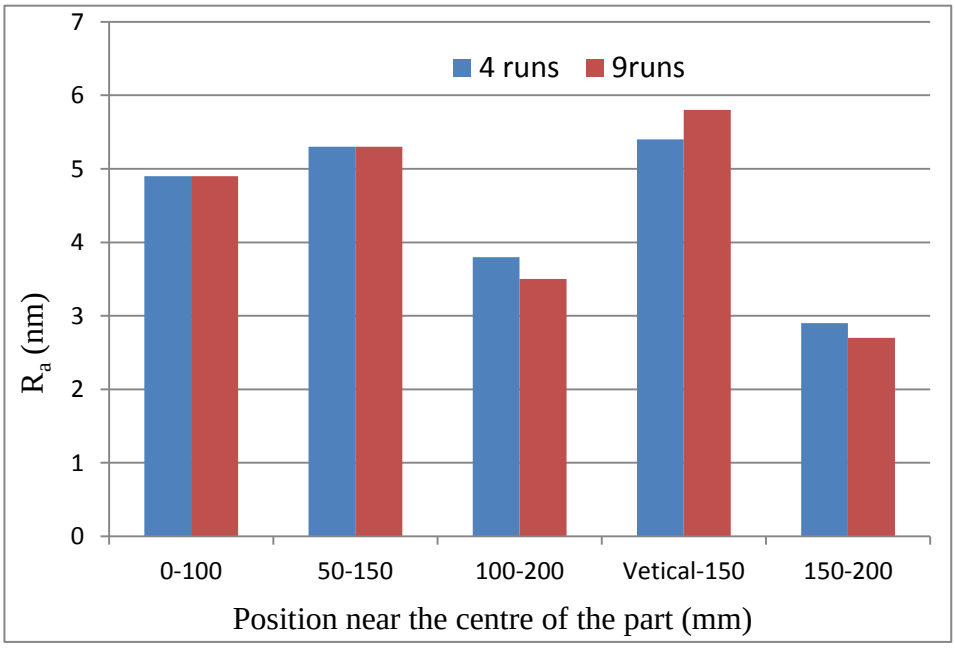

Figure 90： Roughness development after 4 and 9 polishing runs

The surface roughness did not be improved significantly but worsened at a given region from 4 to 9 robot polishing runs. The roughness was improved to within 6μm after 9 robot neutral polishing runs.

4.7.3 Polishing time

The polishing time of one run's robot polishing 400mm square part could be calculated according to "Polishing large ULE ground part" in the experiment procedure 3.2.6.

$$T_1=LW/ (V_p \times S_p) \qquad \text{(Equation 4.7.3.1)}$$

Equation 4.7.3.1 shows the calculation of the polishing time of one run (T_1), where L and W are the length and width of the polishing area, V_p is the polishing speed, S_p is polishing step. Then, T_1=425mm x425mm/ (10mm/s x 1mm) = 18062s=5h. The total polishing time for 9 runs robot polishing to remove away the grinding cusp was 45 hours.

4.7.4 CMM and Zygo interferometer measurements

The 400mm square ULE part was measured using the Leith CMM after BoX grinding and after robot neutral polishing. The region assessed was 5mm from edges of sample within an inscribed circle surface as shown in Figure 91.

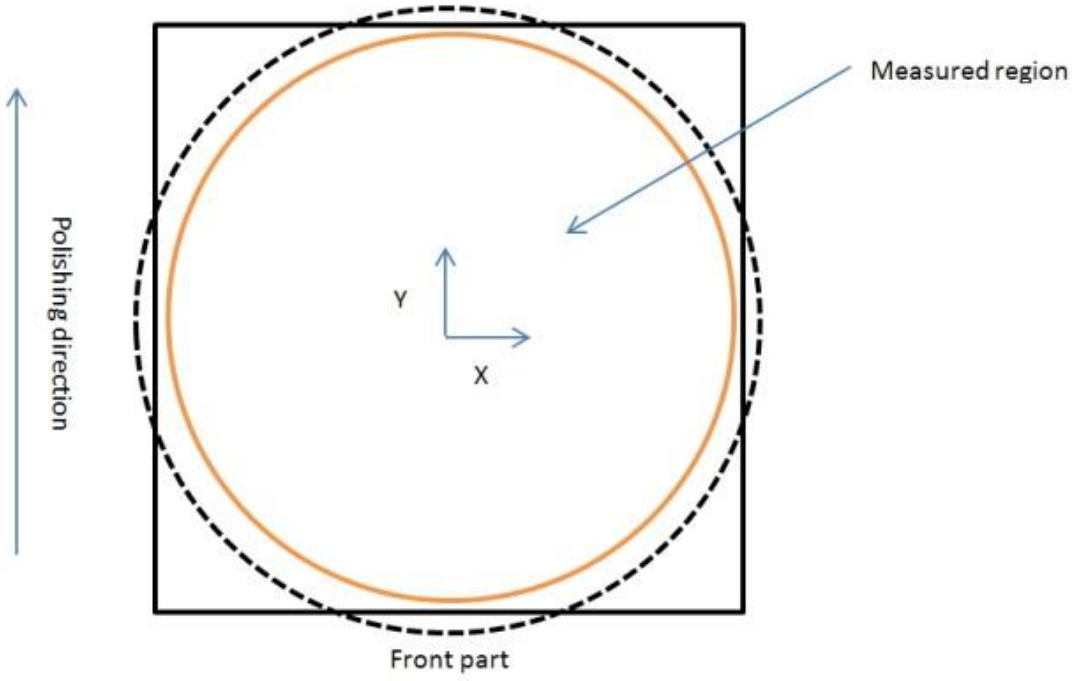

Figure 91: CMM measurement - Measured region

A raster scanning path was performed and data points were recorded every 10mm in X and Y directions. The Z positions were best fitted to a fixed best fit radius of curvature (2950) to obtain surface form accuracy (P_t). The data points obtained after grinding process are shown in Figure 92.

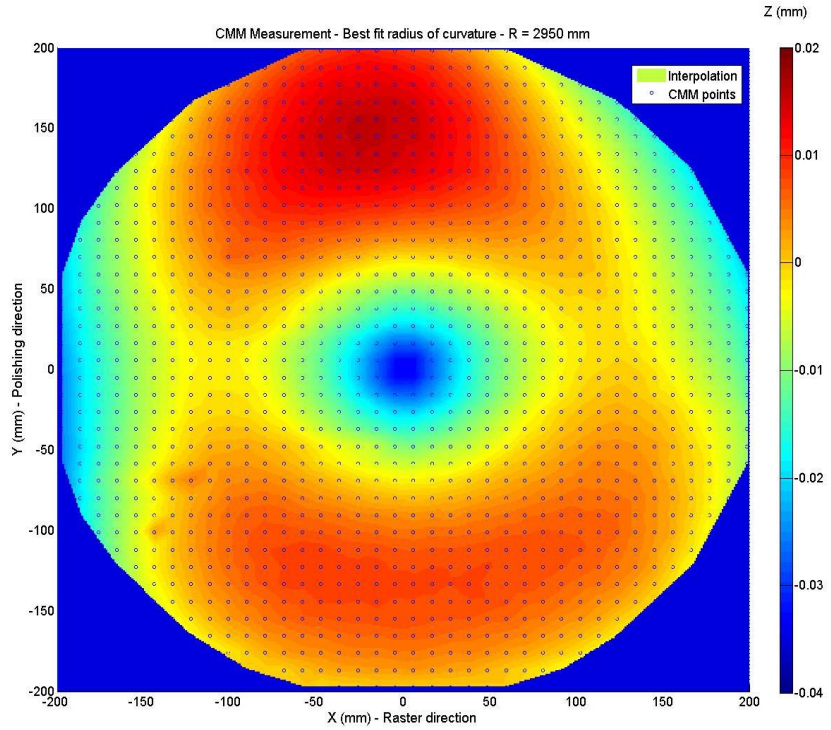

Figure 92: Data points obtained from CMM after grinding process

The form accuracy was 40µm with an astigmatism effect in the Y direction. The central region form error was due to the spiral grinding tool path employed (section 3.2.4.3). The rotary table reached a maximum rotation speed leading to a reduction in grinding forces and resulting in a change in Z position between the tool and the part.
The data points obtained after robot neutral polishing are shown in Figure 93.

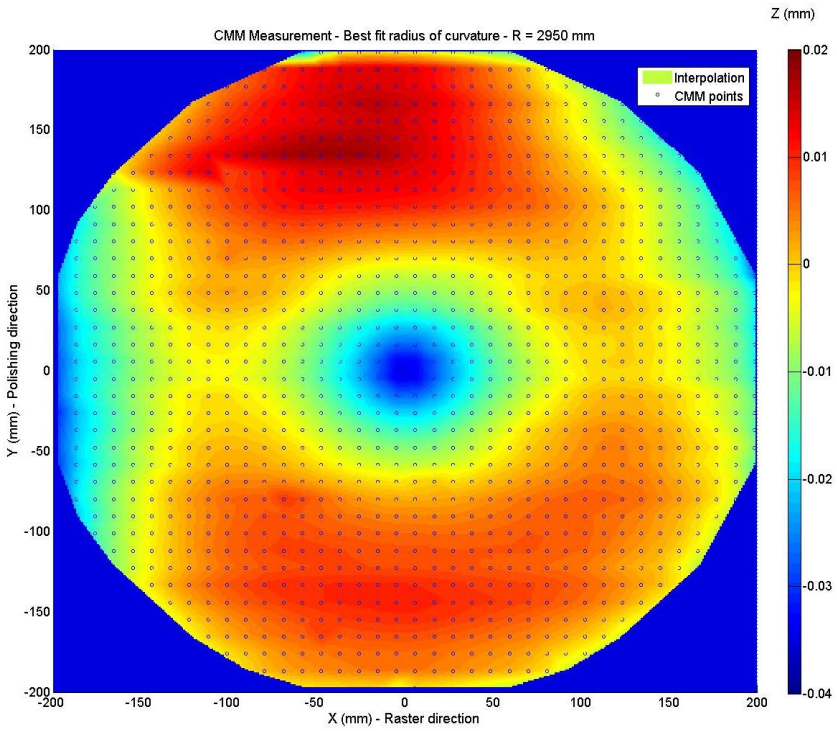

Figure 93 : Data points obtained from CMM after robot neutral polishing process

The surface form error was maintained below 40μm after robot neutral polishing. Some additional form errors could be observed in the polishing direction. These could be limited to the repeatability of the probing that was used to generate the robot tool path using the bespoke Matlab software (see Section 4.2). The Talysurf profilometer was employed to investigate details edge effects as well as grinding and polishing grooves.
The part was placed under the optical tower and tested using the Zygo interferometer. The fringes obtained as shown in the section of A9.9. Due to the form accuracy and polishing raster lines, an interferometry measurement was not possible. This was mainly due to the missing central region (high slope error) and the high fringes density obtained. This should be resolved by additional polishing operations to correct the surface form error or by re-grinding this part to a higher precision.

5. Discussion

5.1 Calibrations

Calibrations of the polishing force and probing technology are significant because they would affect the surface quality of the polished part.

Figure 38 shows the calibration of the force measurement platform, the sensor's average repeatability was within ±8N. It would make a difference of ±50 µm in the Z position below the touch point according to Equation 4.3.1.1. These values are within the targeted repeatability of the polishing system.

During the polishing process, the total force recorded corresponded to the applied force as well as the polishing slurry and tool rotation forces which accounted for an additional 30-40N (Figure 39 and 58). The calculated polishing force employed was the total recorded force excluding the effect of the polishing slurry and the tool rotation.

Figure 40 and Figure 41show the calibration of the probing technique, the probing results for a given probe length were repeatable but varied by over 50 µm for different positions in X and Z coordinates. Georgiou (2011) investigated that the industry FUNUC robot arm had the following characters: the repeatability of X coordinate was good at 25 µm and the repeatability of Z coordinate ranged from 16 µm to 56 µm. The position error in Z coordinate had a maximum inaccuracy of ±100 µm over 1000mm robot coordinate.

5.2 Polishing tools and material removal rate

5.2.1 Polishing tool

Figure 94 shows the connection between Z position below touch point and force of polyurethane tool and pitch tool.

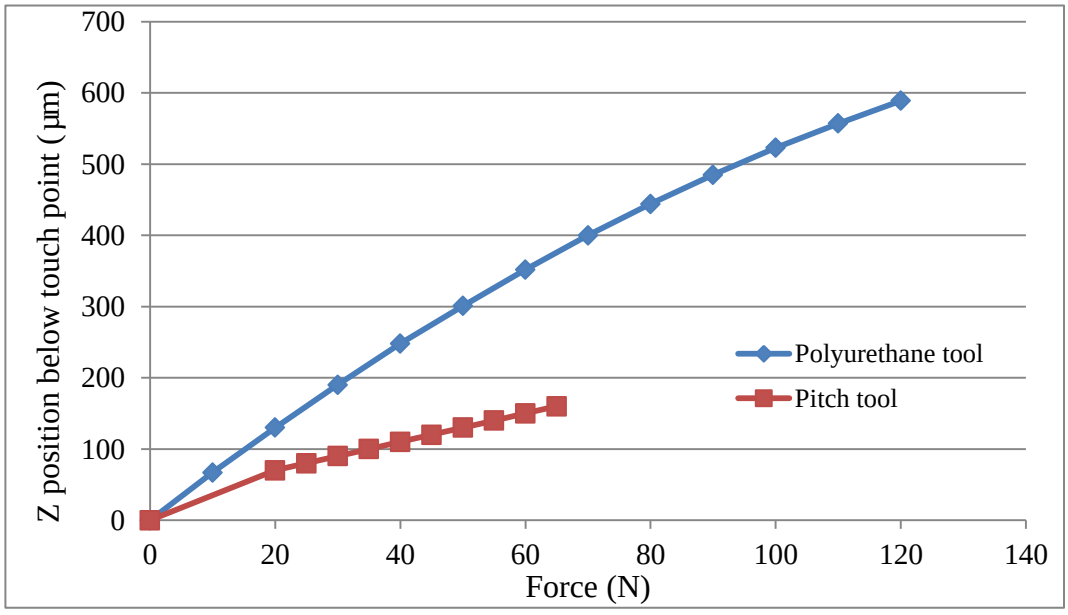

Figure 94: Connection between Z position below touch point and force of polishing tool

The pitch tool, Gugolz Polishing Pitch (No. 73), was stiffer than the polyurethane tool,

LP-66 polyurethane pad, employed in this project.
Actions, such as selecting softer specification of the Gugolz Polishing pitch, testing different temperature and time set in the oven to heat the pitch or burying the cerium oxide inside the pitch polishing tool, should be taken to modify the pitch tool which may help to realize the objective 2 of the project to improve the surface roughness.

5.2.2 Polishing pressure

After comparison of the spots polished by polyurethane tool with different angles in the section of 4.4.1, the maximum tool angle which produced the most symmetric size was 3.5 degree. Figure 95 shows the polishing pressure of polyurethane tool on contact area.

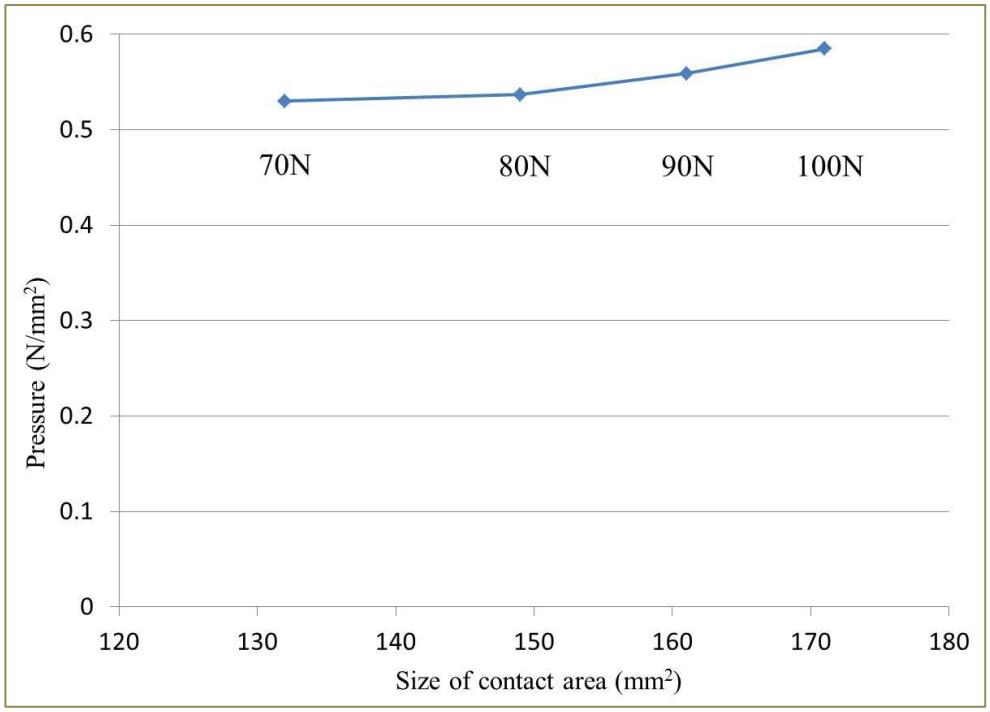

Figure 95: Pressure of polyurethane tool on contact area – 3.5 degree

The pressure increased with the increasing of polishing force however this is not linear as these results in a growing contact area. The calculated polishing pressure for a 100N force was 0.585N/mm^2. The pressure was similar with the pressure used for polishing grooves (0.55N/mm^2) (see the calculation in section 4.5.4). However, the pressure is higher than the pressure (0.1N/ mm^2) used for polishing ELT segments but similar to the pressure employed for EEM to CNC polishing glass (introduced in section 2.4.3).

A limitation of maximum MRR was the maximum available spindle torque which prevented employment larger size polishing tool for larger size spots. The size of a standard polishing tool employed on Zeeko machines is 80mm radius (Walker et al., 2004). The method to increase the polishing contact area would be to use larger polishing tool requiring a spindle with a higher torque.

5.2.3 Preston coefficient

The Preston coefficient derived from the experimented work was 0.97 x 10^{-13} m^2/N (shown in section 4.5.4). The result is in the order of 10^{-13} m^2/N which coincides with the result of Ong and Venkatesh (1998). They polished pyrex glass with 1 μm grain size cerium oxide powder with a polyurethane pad (the polishing pad and the wafer surface were modelled as statistically distributed hemispheres) and found a Preston coefficient of 3.313 x 10^{-13} m^2/N. Fiedler (1995) explained that the Preston coefficient for different kinds of glass-polishing was similar providing comparable chemistry was employed.

5.3 Robot polishing 100mm square sample

5.3.1 Volume of material removed

Equation 5.3.1.1 shows the calculation of the volume of material removed from the ground fused silica after robot polishing, where V_f is the volume of removed material, S_f is the size of the fused silica sample, D_f is the removed depth.

$$V_f = S_f \times D_f \qquad \text{(Equation 5.3.1.1)}$$

As can be seen from the ground fused silica sample half of whose surface was polished, the surface profile (P_t) was 21.5 μm (see Figure 68 in section 4.6.2.1) which equalled to the removed depth (D_f). Then, V_f = (100mm x 100mm) x 21.5x10^{-3} mm =215mm^3.
Similar to polishing the lapped sample (see Figure 65 in section 4.6.1.3), the surface roughness achieved the requirement after one polishing run with the volume of 36mm^3 fused silica removed. More polishing runs and polishing times were employed to remove the grinding cusps on the surface.

5.3.2 Material removal rate

Equation 5.3.2.1 shows the calculation of the material removal rate of polishing fused silica (MRR_{1f}), where V_f means the volume of removed fused silica and t_f means the time of polishing fused silica.

$$MRR_{1f} = V_f / t_f \qquad \text{(Equation 5.3.2.1)}$$

Then, MRR_{1f} =215mm^3 / (125mm x125mm / (5mm/s x 1mm))/6 = 1.15 x 10^{-2} mm^3/s.
Comparing the result with the material removal rate of ULE which was 1.97 x 10^{-3} mm^3/s (see section 4.5.3), the material removal rate is 5.8 times higher than ULE.

5.3.3 Edge effect

Figure 65 (in the section of 4.6.1.4) showed the edge effect of the 100mm square robot neutral polished part. The regions (1) and (2) showed the edge roll-off and the region (3) showed the tool effect after polishing.
The compensation of the tool effect in the third region was shown in Table 28 which was half the value in the compensation of the tool effect summarized from the form accuracy of the polished grooves in Figure 61. Therefore, it could be concluded that the compensation worked from the form accuracy of the polished ground part in Figure 72.
The compensation of the edge roll-off in this project is to lift the polishing tool for a

smaller spot size and a lower polishing pressure near the edge therefore removing less material. Jones et al (2007) employed smaller spot sizes near edges to minimize the edge effect whereas larger spot sizes were employed away from the edge to remove material quicker.

5.3.4 Raster line from polishing

Figure 96 to Figure 98 show the form of the polished surfaces (lapped and ground) after robot polishing.

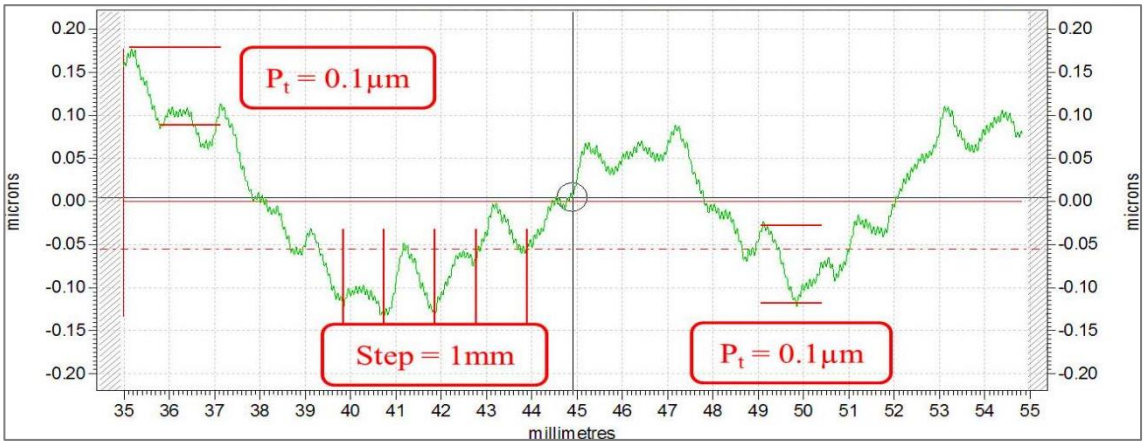

Figure 96: The form of the lapped sample after 7 robot polishing runs

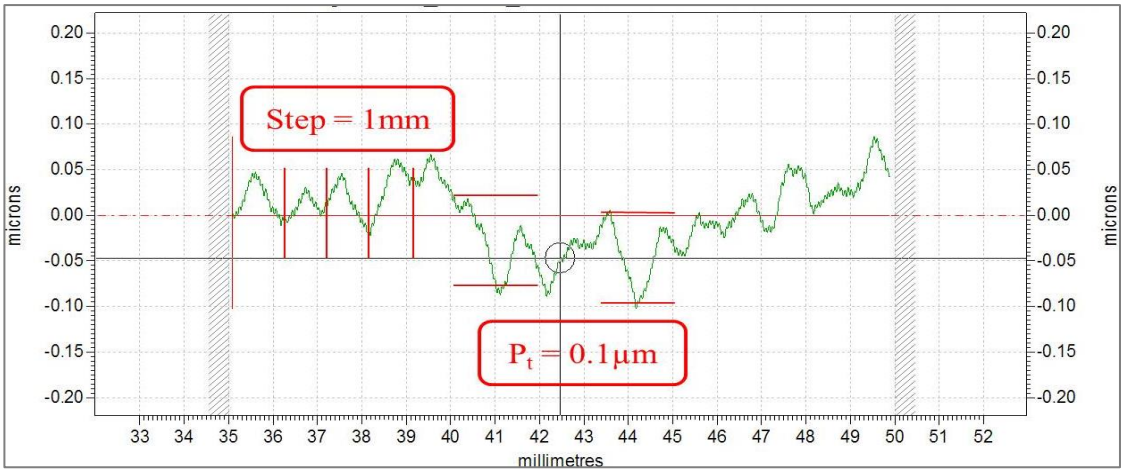

Figure 97: The form of the ground part after 6 robot polishing runs – side1

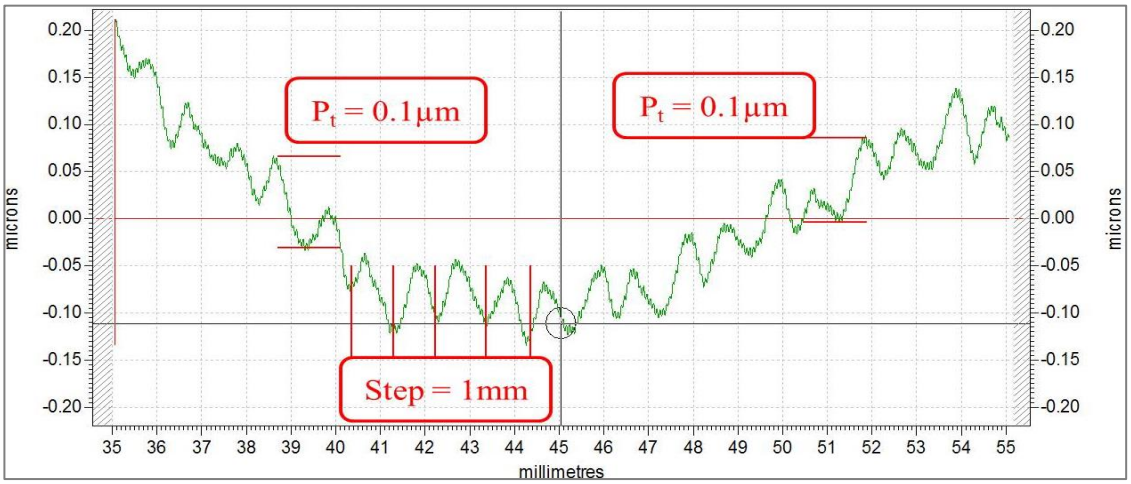

Figure 98: The form of the ground part after 6 robot polishing runs – side 2

It can be seen from the charts that the step of the polishing grooves was 1mm and the surface profile (P_t) of the polishing lines was about 0.1 μm.

According to Equation 2.2.3.1, $P_t = f^2/8R$, which is the calculation of the surface profile for rigid tool. For this project, f = 1mm, R =200mm, then, P_t =1mm^2/ (8 x 200mm) =0.6 μm.

The reasons for the difference of the surface profile measured and calculated may include: 1) the radius of the polishing tool increased when it was pressed on the surface of the sample; 2) the polished groove did not have symmetric geometry.

Figure 99 shows the cross section of the grooves polished using the polyurethane tool.

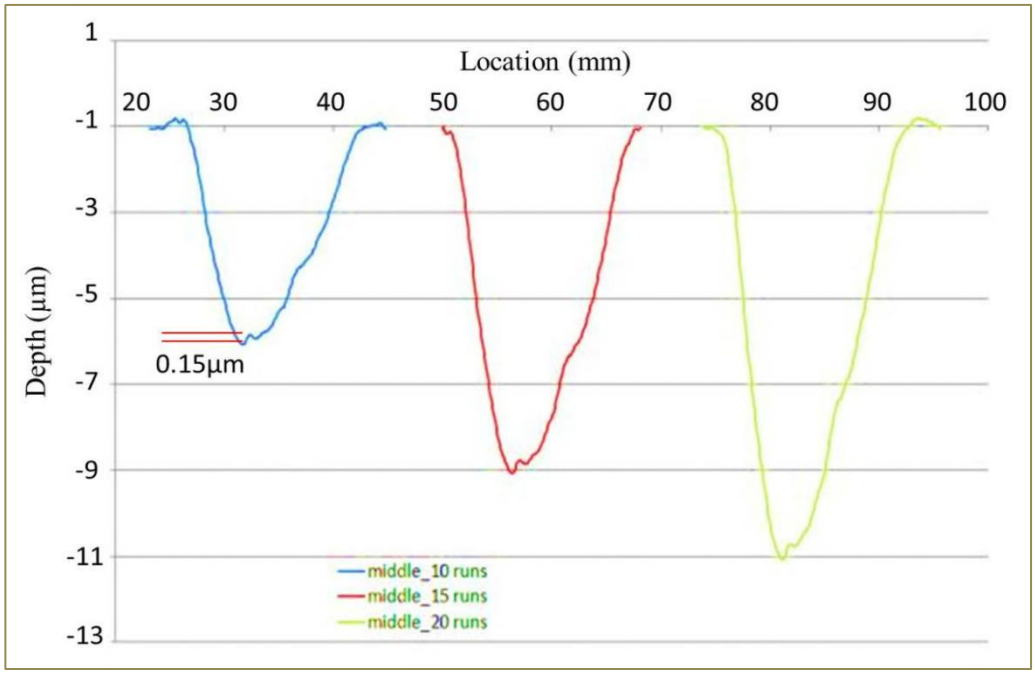

Figure 99: Cross section of the grooves polished by polyurethane tool

The height of the small groove in the bottom of the groove after 10 runs polishing was about 0.15 μm. The surface profile (P_t) should be about 0.1 μm after 6 runs or 7 runs polishing which coincides with the results measured in Figure 92 to Figure 94.

5.4 Robot polishing 400mm square component

5.4.1 Polishing time

Messner et al., (2007) employed the MRF polishing technology with Q-22-950F polishing machine and the raster polishing tool path to polish an 840mm diameter fused silica component which was pre-polished to a vertex radius of 2295mm by the SOML. The total polishing time spent was 256 hours to improve the root mean square (RMS) residual error from 5.1 µm to 0.51 µm.

According to equation 4.7.3.1(in section 4.7.3), the time used for polishing one run of an 840mm diameter component employing robot neutral polishing used in this project would be: T_1=3.14 x 450^2 mm^2/ (10mm/s x 1mm) = 63585s=17.6h. The total polishing time for 9 robot polishing runs would be 159 hours. However, this polishing does not improve the surface profile which may increase polishing time due to the necessity of convergence.

5.4.2 Edge effect

Figure 100 shows the form accuracy of the part near the edge before polishing. There was no edge roll off before polishing process.

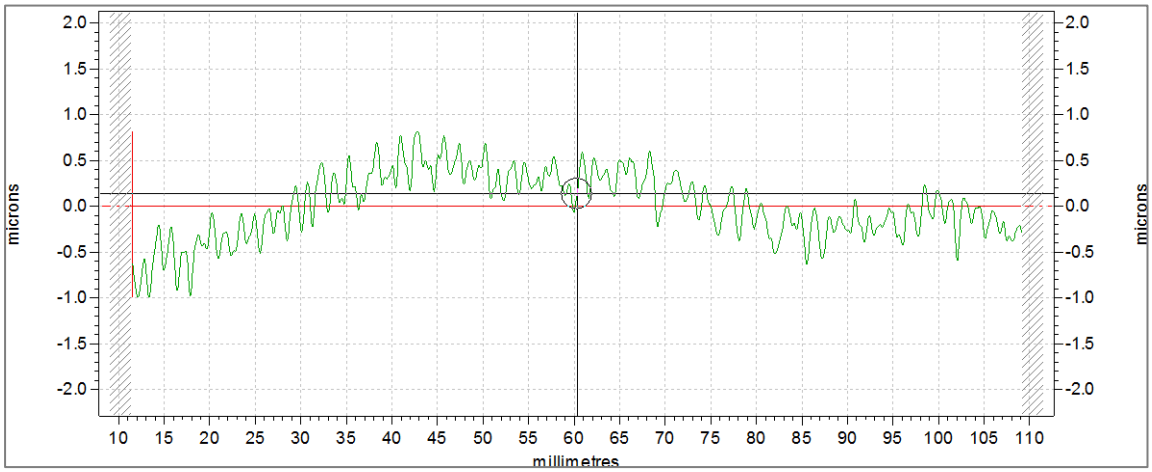

Figure 100: Form accuracy before polishing - vertical polishing direction (direction 12-16)

Figure 101 and Figure 102 show the edge roll-off of the robot neutral polished part for both the direction parallel and vertical to the polishing direction.

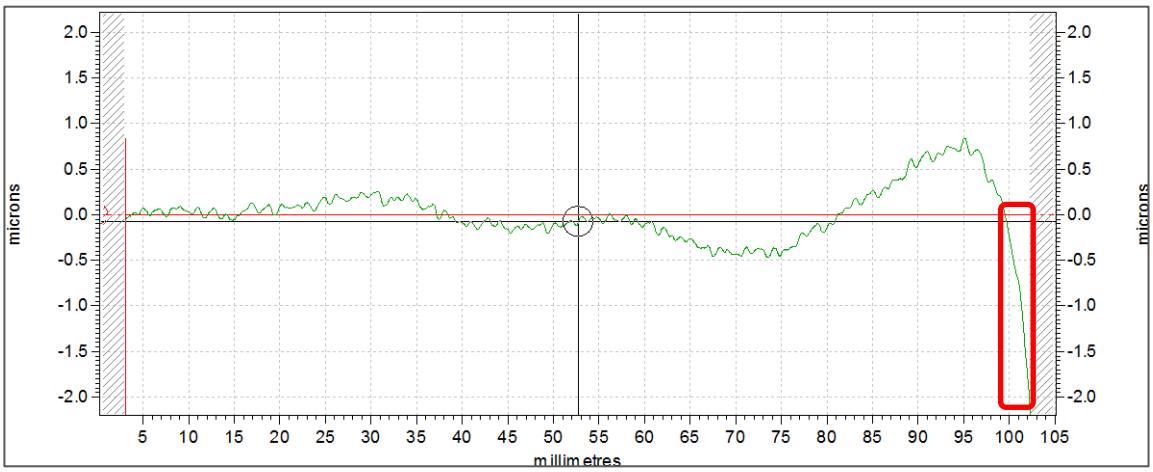

Figure 101: Edge roll-off of robot neutral polished 400mm square part - parallel polishing direction (direction 2-6)

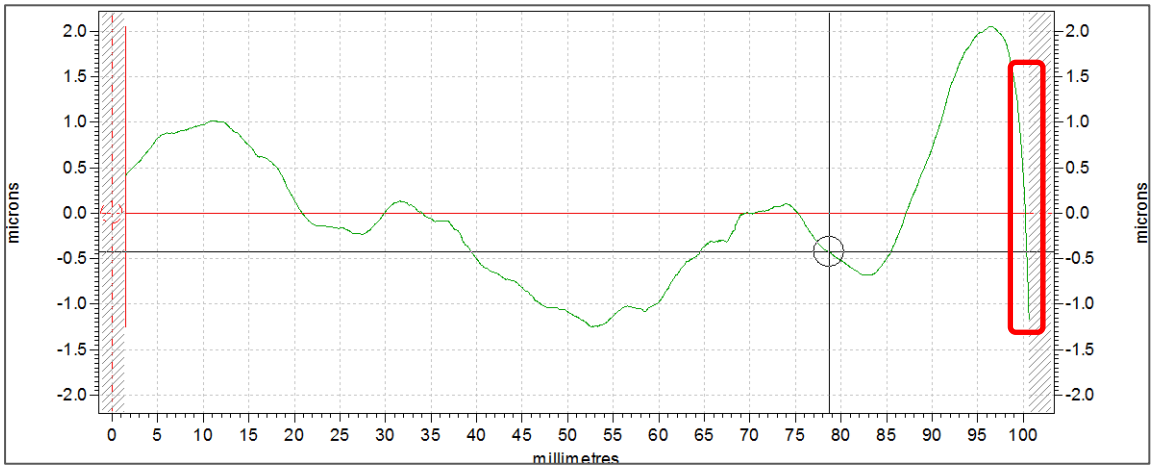

Figure 102: Edge roll-off of robot neutral polished 400mm square part - vertical polishing direction (direction 12-16)

The compensation of the edge roll-off parallel the polishing direction in this project is to lift the polishing tool so that a smaller spot size and a lower polishing pressure were employed near the edge to remove less material. The tool path is shown in Figure 103.

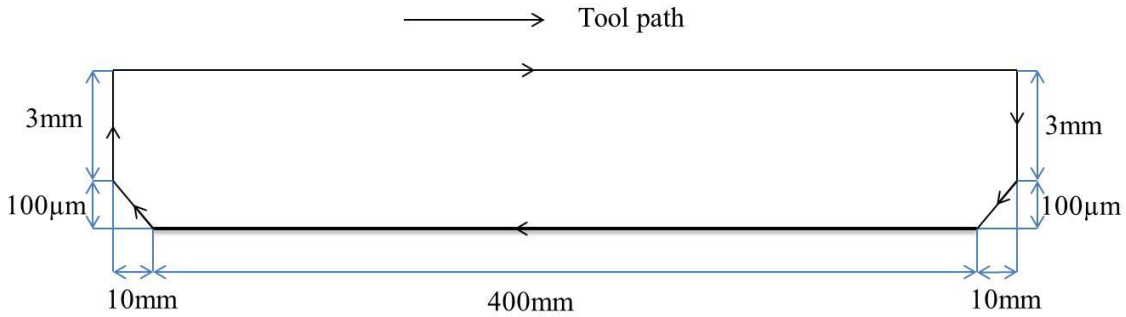

Figure 103: Tool path of polishing 400mm square part to compensate the edge roll-off

The polishing tool was lifted by 100 µm at the point 10mm away from the edge higher than the Z coordinate at the edge.

5.4.3 Raster line from polishing

Figure 104 shows the polishing lines left on the surface of the polished 400mm square part due to the raster polishing feed rate which was 1mm.

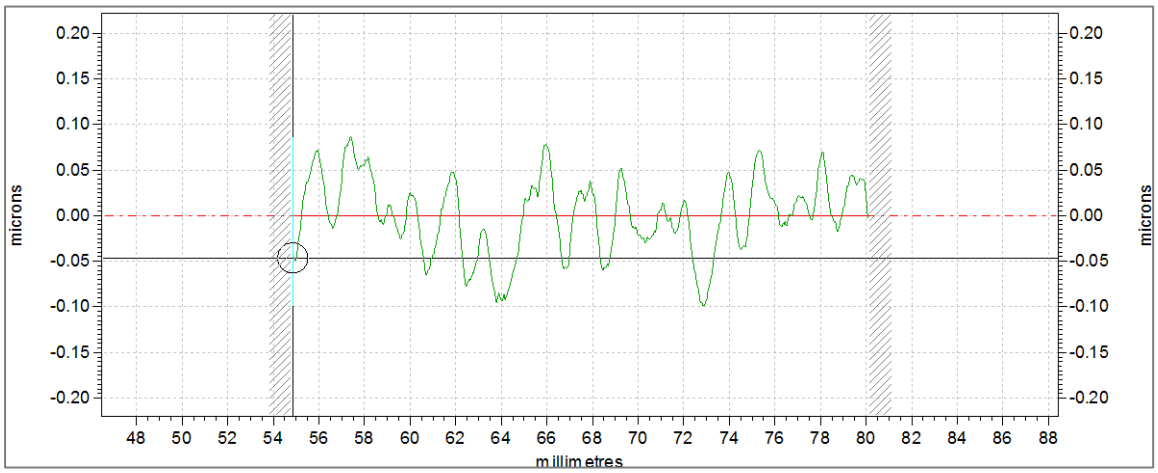

Figure 104: Polishing lines of the 400mm part after 9 runs polishing (vertical to polishing direction)

It can be seen from the plot that the step of the grooves was 1mm from 65mm to 72mm because of the unobvious small grooves. The step of the grooves was 2mm in the other areas.

Franse (1990) explained different grooves in precision-machining are caused by various feed rate, overlap and vibrations, this is shown in Figure 12-d) in the section of 2.2.3. The step of polishing lines in Figure 99 for the 1mm feed rate could be caused by overlap and the limitation of the repeatability the robot arm used in this project.

5.5 Pitch polishing tool

The roughness of the pitch polished spots on the surface of robot neutral polished sample had no significant improvement with the 9 µm diameter cerium oxide. Therefore, reducing sizes of cerium oxide may be necessary. Tesar and Fuchs (1991) used an average cerium oxide particle size of 0.78 µm to polish Fused silica. Ong and Venkatesh (1998) polished one pyrex glass with 1 µm grain size cerium oxide powder on a polyurethane pad; After 3 minutes' polishing, the roughness of part was improved from 74.3nm to 8.7nm and then decreased to 14.7nm. Eminess technologies (2004) produced the cerium oxide employed for polishing fused silica, zerodur and glass whose size is between 0.55 µm to 3.2 µm. Suratwala et al. (2008) carried tests of polishing with 0.5 µm cerium oxide slurry on polyurethane or pitch pads.

6. Conclusions

In summary:

- The surface profile (P_t) and roughness (R_a) of the 100mm square lapped sample were achieved to within 6μm and 10nm respectively with robot neutral polishing which fulfilled objective 1.2 of the project.

  The roughness (R_a) of the 100mm square ground part was improved to within 10nm which conformed to objective 1.1 of the project. However, the surface profile (P_t) degraded to over 2μm which was caused by the following reasons: first, the surface profile (P_t) of the ground sample was not 1μm but 2-3μm; second, the edge effect of the part after polishing made the surface profile worse.

  The roughness (R_a) of the 400mm square part was improved to within 6nm after robot neutral polishing which fulfilled objective 1.1 of the project.

  A pitch tool was developed and initial polishing experiments were carried out. Surface roughness (R_a) measured was similar to polyurethane polishing. Therefore, additional works, such as using smaller cerium oxide particles or different pitch, are necessary to achieve object 2.2 of this project.

- Time used of polishing 400mm square part:

  The total time to achieve the surface roughness required was 20 hours which corresponds to 4 runs polishing. The total time spent to remove the grinding cusp was 45 hours which spent 9 runs polishing. The total time could be reduced if the cusps generated by grinding process are smaller after grinding.

- Raster polishing lines were left on the surface of robot neutral polished samples for both 100mm square part and 400mm square part. These were of a magnitude of 0.1μm (P_t) which was generated by the form error of the polyurethane tool employed.

7. Further works suggestions

The following works are suggested to be done in the future to improve the robot polishing system.

- Pitch polishing of robot neutral polished parts:

  To obtain a more symmetric spot size and an improved surface roughness, additional tests of polishing spots and grooves with various tool angles, polishing pressures, polishing times and sizes of cerium oxide should be carried out.
  To check the degree of pitch tool wear, the 100mm square robot neutral polished samples and the 400mm square larger robot neutral polished part should be polished. This would provide information about the roughness (R_a) and surface profile (P_t) improvement during a short and a long time pitch polishing period

- To obtain higher torque capability, the current spindle should be modified so that larger polishing tool size could be employed to increase contact area between the polishing tool and the sample.

- Polishing Silicon Carbide parts with a rotary table:

  Based on the Preston coefficient and reported material removal rate of SiC, the polishing process is expected to be significantly longer than ULE. In order to speed up this process, a rotary table should be designed and a spiral polishing strategy should be implemented. The polishing tool moves from the edge to the centre of the round part at a given tool angle, speed and feed rate while the table rotates at a fixed speed.
  In addition, a new kind of polishing slurry, diamond, should be prepared and spots as well as grooves should be polished to obtain a symmetric spot size and to calculate the material removal rate.

- Polishing a random tool path strategy to avoid raster polishing lines:

  To eliminate polishing raster lines, the eccentric tool technique or random tool path generated using a dedicated software should be investigated. Tests should be carried out to check the difference in surface texture condition after robot polishing employing the random tool path and the raster tool path.

8. References

Abrasifs Grains et Poudres , (2013), “Polyurethane”, P1, Technical Data.

Arrasmith, S. R., Kozhinova, I. A., Gregg, L. L., Shorey, A. B., Romanofsky, H. J., Jacobs, S. D., Golini, D., Kordonski, W. I., Hogan, S. and Dumas, P. (1999), "Details of the polishing spot in magnetorheological finishing (MRF) ", SPIE 3782: Optical Manufacturing and Testing III, ed. H. P. Stahl, pp. 92-100.

Brecher, C., Tuecks, R., Zunke, R., and Wenzel, C. (2010), "Development of a force controlled orbital polishing head for free form surface finishing", Production Engineering, Vol. 4, no. 2, pp. 269-277.

Boostec industries, (2012), 9th International Conference on Space Optics, Ajaccio, see http://www.congrexprojects.com/custom/icso/2012/presentations/015_Bougoin.pdf -accessed 17/02/14.

Budget Estimates, FY2014, "Public Benefits of the FY14 NASA Budget", See http://www.nasa.gov/pdf/740427main_NASAFY2014SummaryBriefFinal.pdf -accessed 09/02/14.

Choi, W., Abiade, J., Lee, S. M., and Singh, R. K. (2004), "Effects of slurry particles on silicon dioxide CMP", Journal of the Electrochemical Society, Vol. 151, no. 8, pp. 512-522.

Coorstek, (2012), "Ultrasic direct sintered and puresic cvd silicon carbide for optical applications". Coorstek Amazing Solutions, Silicon Carbide Optics.

Dierickx, P., Enard, D., Merkle, F., Noethe, L., and Wilson, R. N. (1990), "8.2 metre primary mirrors of the VLT", Tyson Robert K. and Schulte in den Baumen J. (eds.), Proc. SPIE 1271, in: Adaptive Optics and Optical Structures, Vol. 1271, Hague, Neth, Publ by Int Soc for Optical Engineering, Bellingham, p266.

Dunn, C. R., and Walker, D. D. (2008), "Pseudo-random tool paths for CNC sub-aperture polishing and other applications.", Optics Express, Vol. 16, no. 23, pp. 18942-18949.

DynaFiz, (2013), see http://action.zygo.com/acton/attachment/4246/f-0122/1/-/-/-/-/DynaFiz_specs.pdf -accessed 19/02/14.

Eminess technologies, (2014), see http://www.eminess.com/products/polishing_slurries/cerium_oxide - accessed 04/08/14.

Evans, C. J., Paul, E., Dornfield, D., Lucca, D. A., Byrne, G., Tricard, M., Klocke, F., Dambon, O., and Mullany, B. A. (2003), "Material removal mechanisms in lapping and polishing", CIRP Annals - Manufacturing Technology, Vol. 52, no. 2, pp. 611-633.

Export Regulations of International Traffic in Arms, (2006) , See http://counsel.cornell.edu/ITAR/ITAR-summary.html -accessed 28/01/14.

Fabbrizzi, F., and Mariani, A. (1986), "Lightweight Metal Mirror for the Giotto Multicolour Camera.", SPIE Vol.701 Ecoosa 86, Florence, p8.

Fiedler, K.H., (1995), "Processing: grinding and polishing", in: B. Neuroth (Ed.), The Properties of Optical Glass, Springer-Verlag, Berlin, pp. 245–262.

Fisba Optik, (2004), "FST 10 system User Manual", FST 10 - 1.01-01.00.E.

Franse, J. (1990), 'Manufacturing techniques for complex shapes with submicron accuracy', Reports on Progress in Physics 53(8), Vol. 53, pp. 1049–1094.

Georgiou. C. A., (2011), "Thermal Performance of a Multi-Axis Smoothing Cell", MSc thesis, School of Applied Sciences, Cranfield University.

Geyl, R., and Cayrel, M. (1999), "REOSC contribution to VLT and Gemini.", Proc. of SPIE - The International Society for Optical Engineering, Vol. 3739, pp. 40-46.

Gillman, B. E., and Tinker, F. (1999), "Fun facts about pitch & the pitfalls of ignorance.", Proc. SPIE 3782, Optical Manufacturing and Testing III, p72.

Goela, J. S., Desai, H. D., Taylor, R. L., and Olson, S. E. (1995), "Thermal stability of CVD-SiC lightweight optics", Ealey Mark A. (ed.), in: Silicon Carbide Materials for Optics and Precision Structures, Vol. 2543, San Diego, p38.

Goodman, W. A., and Tanaka, C. (2009), "Recent achievements using chemical vapor composite silicon carbide (CVC SiC)", Optical Materials and Structures Technologies IV, Vol. 7425, San Diego, CA.

Guo, J., Suzuki, H., Morita, S., Yamagata, Y., and Higuchic, T. (2013), "A real-time polishing force control system for ultraprecision finishing of micro-optics.", Precision Engineering Vol.37, pp.787– 792.

Hexagon metrology, (2014), see http://www.leitz-metrology.com/Leitz-PMM-F-30201016_544.htm -accessed 19/02/14.

Hobbs, T. W., Edwards, M., and VanBrocklin, R. (2003), "Current fabrication techniques for ULE® and fused silica lightweight mirrors", Goodman W.A. (ed.), in: Optical Materials and Structures Technologies, Vol. 5179, San Diego, CA, p1.

Hoeness, H. W., Mueller, R., Rodek, E. W., and Siebers, F. B. (1988), "Monolithic mirror substrates of the 8-m class and lightweight mirror substrates manufactured from the glass ceramic zerodur", SPIE Vol.1013, Optical Design Methods, Applications, and Large Optics, p205.

Hrdina, K. (1999), "Production and properties of ULE glass with regards to EUV masks". The International workshop on Extreme Ultraviolet Lithography,

October 10-13.

Jones, A., Mooney, J. T., and Tricard, M. A. (2007), “Recent Advances in MRF®Finishing of Large Optics” presented to: Technology Days in the Government Mirror Development.

Kim, D.W., and Burge, J.H. (2010), "Rigid conformal polishing tool using non-linear visco-elastic effect.", Optical Express, Vol. 18, no. 3.

Kim, D. W., Park, W. H., Kim, S. W., and Burge, J. H. (2009), “Parametric modeling of edge effects for polishing tool influence functions,” Optics Express 17(7), pp.5656–5665 .

Komanduri, R., Lucca, D. A., and Tani, Y. (1997), "Technological advances in fine abrasive processes", CIRP Annals - Manufacturing Technology, Vol. 46, no. 2, pp. 545-596.

Krödel, M. R., Luichtel, G., and Volkmer, R. (2006), "The Cesic® ceramic optics of the GREGOR telescope.", Optomechanical Technologies for Astronomy, Vol. 6273 I, Orlando, 62730Q.

Li, Y., Hou, J., Xu, Q., Wang, J., Yang, W., and Guo, Y. (2008), "The characteristics of optics polished with a polyurethane pad.", Optics Express, Vol. 16, no. 14, pp. 10285-10293.

Lubliner, J., and Nelson, J. E. (1980), "Stressed mirror polishing - 1. A technique for producing nonaxisymmetric mirrors.", Applied Optics, Vol. 19, no. 14, pp. 2332-2340.

Leuven, (2005), see https://www.mech.kuleuven.be/micro/facilities/Talysurf -accessed 19/02/14.

Luo, J. F. (2003), "Integrated modeling of chemical mechanical planarization/polishing (CMP) for integrated circuit fabrication: from particle scale to die and wafer scales". PhD dissertation, University of California, Berkeley.

Martin, H. M., Angel, J. R. P., Burge, J. H., Cuerden, B., Bavison, W. B., Johns, M., Kingsley, J. S., Kot, L. B., Lutz, R. D., Miller, S. M., Shectman, S. A., Strittmatter, P. A. and Zhao, C. (2006), "Design and manufacture of 8.4 m primary mirror segments and supports for the GMT", Optomechanical Technologies for Astronomy, Vol. 6273 I, Orlando, 62730E.

Matson, L. E., and Mollenhauer, D. (2003), "Advanced materials and processes for large, lightweight, space-based mirrors.", 2003 IEEE Aerospace Conference, Vol. 4, Big Sky, pp.1681-1697.

Measurement specialties, LVDT, "The LVDT: construction and principle of operation", see http://meas-spec.com/downloads/Principles_of_the_LVDT.pdf -accessed 17-02/14.

Messner, W., Hall, C., Dumas, P., Hallock, B., Tricard, M., Donohue, S., Miller, S. (2007), "Manufacturing meter-scale aspheric optics", Proc. of SPIE Vol. 6671, Optical Manufacturing and Testing VII, 667106-1.

Meller Optics, Inc. (2013), “Meller Gugolz Polishing Pitch Presents Abrasives Efficiently To Optics”, published on: Surface finishing.com. See http://www.surfacefinishing.com/doc/meller-gugolz-polishing-pitch-abrasives-efficiently-optics-0001 -accessed 23/01/14.

Meller Optics, Inc. (2014), “Gugolz Polishing Pitch”. See http://www.melleroptics.com/shopping/shopdisplayproducts.asp?id=14 – accessed 23/01/14.

Millimar, LVDT, see http://www.buellkft.hu/elemek/1177/millimar--1301--1318--fly--en--2005-11-18.pdf -accessed 19/02/14.

Mori, Y., Ikawa, N., Okuda, T., and Yamagata, K. (1976), "Numerically Controlled Elastic Emission Machining.", Technology Reports of the Osaka University, Vol. 26: pp. 283-294.

Morian, H. F., and Machkh, R. (1998), "Zerodur for lightweight secondary/tertiary mirrors", Stepp L.M. (ed.), in: Advanced Technology Optical/IR Telescopes VI, Proc. SPIE 3352, Kona, p140.

Moses, E. I., Campbell, J. H., Stolz, C. J., and Wuest, C.R. (2003), "The National Ignition Facility: The World's Largest Optics and Laser System." Proc. SPIE 5001, Optical Engineering at the Lawrence Livermore National Laboratory, p1.

Ng, K. Y., and Dumm, T. (2012), "Advancements in lapping and polishing with diamond slurries", 27th International Conference on Compound Semiconductor Manufacturing Technology, CS Mantech 2012, Boston, MA.

Ong, N. S., and Venkatesh, V. C. (1998), "Semi-ductile grinding and polishing of Pyrex glass.", Journal of Materials Processing Technology, Vol. 83, pp. 261–266.

Opto Tech, see http://www.optotech.de/uk/precision/spheres/polishing/spk-150-cnc-hpp/ -accessed 12/02/14.

Pileri, D., and Krabbendam, V. L. (1995), "Hobby-Eberly primary mirror fabrication", Proc. SPIE 2536, Optical Manufacturing and Testing, San Diego, p344.

Rhodia, (2012), "Cerium oxide GPS Safety Summary", see http://www.solvay.com/en/binaries/Cerium_dioxide_GPS_rev0_Sept12_RHD-139543.pdf -accessed 17/02/14.

Rososhansky, M., and Xi, F. F. (2011), "Coverage based tool-path planning for automated polishing using contact mechanics theory.", Journal of Manufacturing

Systems, Vol. 30, pp.144-153.

Seifert, A. (2007), "New products for synchrotron application based on novel surface processing developments", Synchrotron Radiation Instrumentation: 9th International Conference on Synchrotron Radiation Instrumentation, Vol. 879, Daegu, p459.

Sein, E., Toulemont, Y., Safa, F., Duran, M., Deny, P., De Chambure, D., Passvogel, T., and Pilbratt, G. (2002), "A F 3.5 M SiC telescope for HERSCHEL mission", Mather J.C. (ed.), in: IR Space Telescopes and Instruments, Vol. 4850, Waikoloa, p606.

Suratwala, T., Steele, R., Feit, M., Wong, L., Miller, P., Menapace, J., Davis, P. (2008), "Effect of Rogue particles on the sub-surface damage of fused silica during grinding/polishing", Journal of Non-Crystalline Solids. Vol. 354, pp. 2023-2037.

Tesar, A. A., and Fuchs, B. A. (1991)， "Removal rates of fused silica with cerium oxide/pitch polishing", Proc. SPIE 1531, Advanced Optical Manufacturing and Testing II, pp. 80-90.

Tobin, W. (1987), "Foucault's invention of the silvered glass reflecting telescope and the history of his 80-cm reflector at the Observatoire de Marseill.", Vistas in Astronomy, Vol.30,pp. 153-184.

Tonnellier, X., Comley, P., Peng, X.Q., and Shore, P. (2013), "Robot Based Sub-Aperture Polishing for the Rapid Production of Metre-Scale Optics".

Tonnellier, X., (2009), "Precision grinding for rapid manufacturing of large optics". PhD thesis, School of Applied Sciences, Cranfield University.

Tsuno, K., Irikado, H., Oono, K., Ishida, J., Suyama, S., Itoh, Y., Ebizuka, N., Eto, H., Dai, Y., Lin, W., Suzuki, T., Omori, H., Yui, Y. Y., Kimura, T., and Tange, Y. (2005), "New-Technology Silicon carbide (NT-SiC): demonstration of new material for large lightweight optical mirror", Komar G.J., Wang J. and Kimura T. (eds.), in: Enabling Sensor and Platform Technologies for Spaceborne Remote Sensing, Proc. SPIE 5659, Honolulu, p138.

Tsuwa, H., Ikawa, N., Mori, Y., Sugiyama, K. (1979), "Numerically Controlled Elastic Emission Machining". Annals of CIRP, 28/1: pp.193-197.

Ultra precision, Dynafiz, see http://www.ultraprecision.org/location/zygo-laser-interferometer/ -accessed 19/02/14.

Ultra precision, Leitz CMM, see http://www.ultraprecision.org/location/co-ordinate-measuring-machine/ -accessed 19/02/14.

Ultra precision, Microphase interferometer, see http://www.ultraprecision.org/location/fisba-optik-microphase-interferometer/ -accessed 19/02/14.

Ultra precision, Talysurf, see http://www.ultraprecision.org/location/surface-profilerform-talysurf/ -accessed 19/02/14.

Walker, D.D., Beaucamp, A.T.H., Bingham, R.G., Brooks, D., Freeman, R., Kim, S.W., King, A., McCavana, G., Morton, R., Riley, D., Simms, J. (2002), “The Precessions process for efficient production of aspheric optics for large telescopes and their instrumentation”, Proc. SPIE Astronomical Telescopes and Instrumentation Meeting, Hawaii, Vol.4842, pp.73-84

Walker, D., Brooks, D., King, A., Freeman, R., Morton, R., McCavana, G., Kim, S. (2003), "The 'Precessions' tooling for polishing and figuring flat, spherical and aspheric surfaces", Optics Express, Vol. 11 Issue 8, pp.958-964.

Walker, D.D., Beaucamp, A.T.H., Brooks, D., Doubrovski, V., Cassie, M., Dunn, C., Freeman, R., King, A., Libert, M., McCavana, G., Morton, R., Riley, D., and Simms, J. (2004), "Recent development of precessions polishing for larger components and free-form surfaces.", Proc. of SPIE Vol. 5523, Bellingham, p281.

Walker, D. D., Beaucamp, A., Dunn, C., Evans, R., Freeman, R., Morton, R., Wei, S., and Yu, G. (2008), "Active control of edges and global microstructure on segmented mirrors.", Advanced Optical and Mechanical Technologies in Telescopes and Instrumentation, Vol. 7018, Marseille, 701812.

Zhang, Y., Yuan, Z., and Zhou, Y. (2014), "Gelcasting of silicon carbide ceramics using phenolic resin and furfuryl alcohol as the gel former", Ceramics International . Vol. 40, Issue 6, pp.7873–7878.

Zhou, H., Zhang, C. R., Cao, Y. B., and Zhou, X. G. (2006), "Lightweight C/SiC mirrors for space application", Zhang Y., Jiang W. and Cho M.K. (eds.), Proc. SPIE 6148, 2nd International Symposium on Advanced Optical Manufacturing and Testing Technologies: Large Mirrors and Telescopes, Xian,6148L.

9. Appendices

9.1 Calibration of force measurement platform

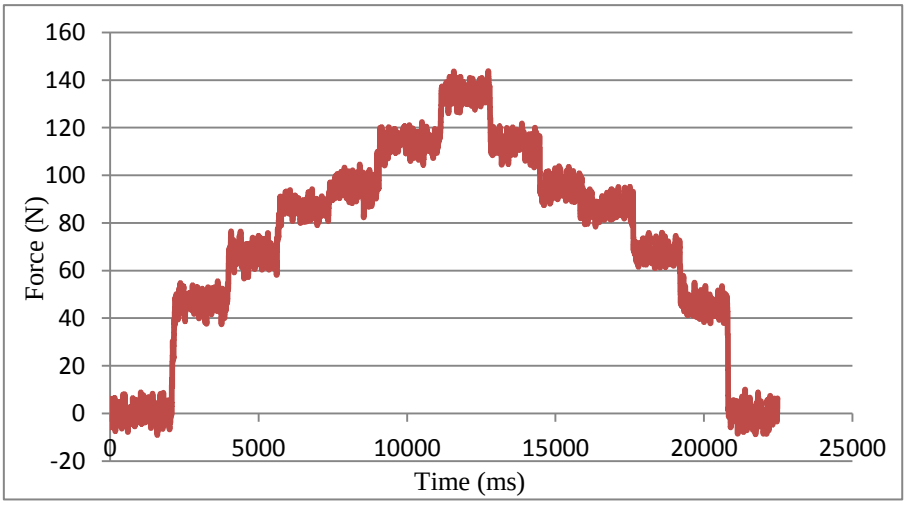

Figure 105: Loading and unloading for force measurement validation – second run

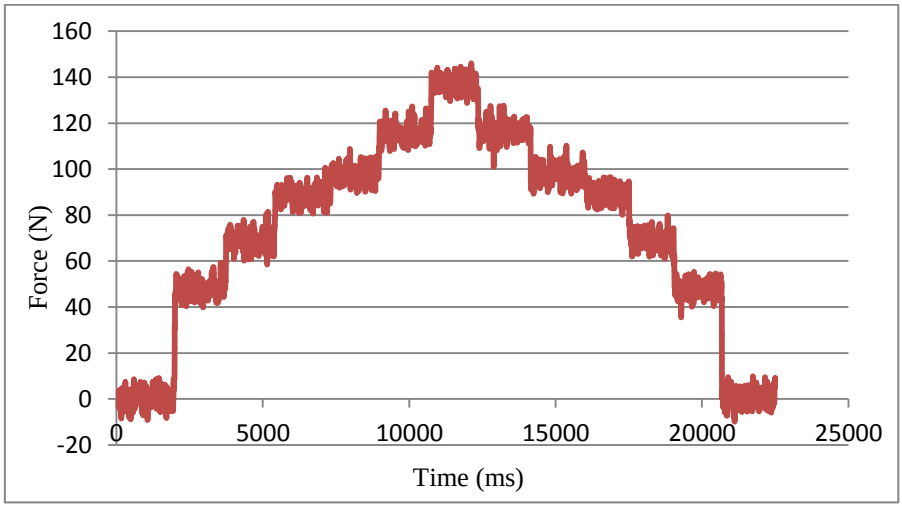

Figure 106: Loading and unloading for force measurement validation – third run

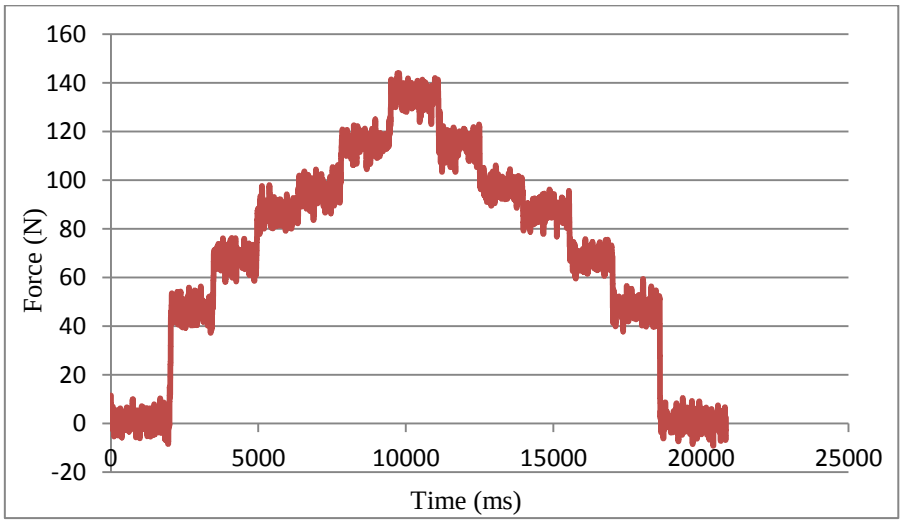

Figure 107: Loading and unloading for force measurement validation – fourth run

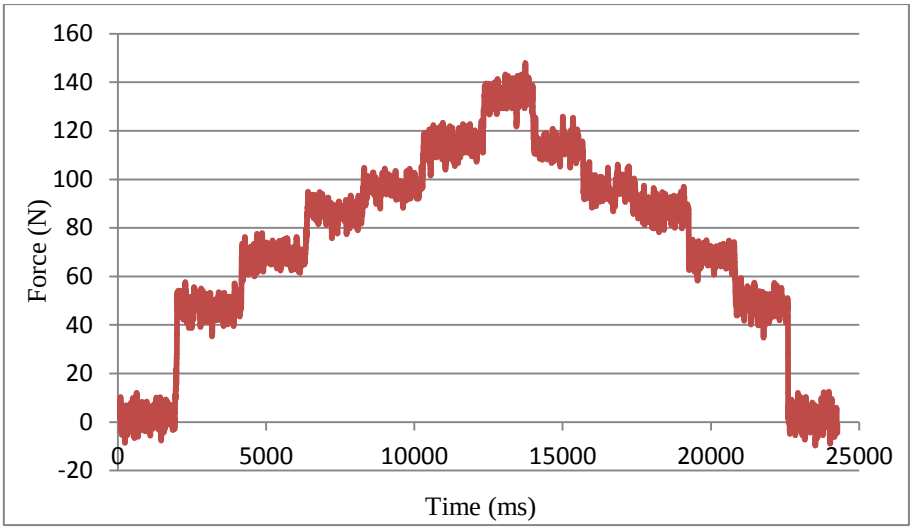

Figure 108: Loading and unloading for force measurement validation – fifth run

9.2 Connection between press depth and force of polyurethane tool

Table 29: Connection between press depth and force_3.5_Z1-2.1

Depth (um)	Force (N)	Force (N)	Force (N)	Average (N)
0	0	0	0	0
-50	7	5	5	6
-100	15	13	12	13
-150	24	20	18	21
-200	32	30	27	30
-250	42	40	38	40
-300	52	50	48	50
-350	62	59	58	60
-400	72	72	69	71
-450	83	81	82	82
-500	96	93	93	94
-550	107	105	106	106
-600	119	118	118	118

Note: The tool length was about 10mm shorter than the length of the probe

Table 30: Connection between press depth and force_3.5_Z1-2.2

Depth (um)	Force (N)	Force (N)	Force (N)	Average (N)
0	0	0	0	0
-50	9	6	5	7
-100	16	12	10	13
-150	24	19	17	20
-200	34	27	25	29
-250	43	38	35	39
-300	53	48	47	49
-350	63	60	57	60
-400	73	72	68	71
-450	84	82	80	82
-500	96	94	94	95
-550	109	107	106	107
-600	120	120	116	119

Note: The tool length was about 10mm shorter than the length of the probe

Table 31: Connection between press depth and force_3.5_Z1-1

Depth (um)	Force (N)	Force (N)	Force (N)	Average (N)
0	0	0	0	0
-50	8	5	4	6
-100	13	10	8	10
-150	18	15	14	16
-200	27	24	21	24
-250	35	31	28	31
-300	44	38	36	39
-350	52	48	46	49
-400	60	57	55	57
-450	70	68	67	68
-500	82	77	77	79
-550	93	90	88	90
-600	103	103	100	102

Note: The tool length was about 10mm shorter than the length of the probe

Table 32: Connection between press depth and force_3.5_Z2

Depth (um)	Force (N)	Force (N)	Force (N)	Average1 (N)	Force (N)	Force (N)	Force (N)	Average2 (N)
0	0	0	0	0	0	0	0	0
-50	9	6	5	7	10	7	5	7
-100	16	12	11	13	18	15	13	15
-150	25	21	18	21	27	24	21	24
-200	34	29	27	30	37	32	31	33
-250	43	37	37	39	46	44	40	43
-300	53	47	45	48	56	54	51	54
-350	63	60	59	61	67	64	62	64
-400	75	72	72	73	79	76	75	77
-450	84	83	81	83	90	88	88	89
-500	96	94	93	94	101	100	100	100
-550	109	106	105	107	112	112	111	112
-600	123	120	118	120	126	125	125	125

Note: The tool length was the same as the length of the probe

9.3 Measuring and modifying the concentricity of the pitch tool

Figure 102 shows the process of measuring and modifying the concentricity of the pitch tool.

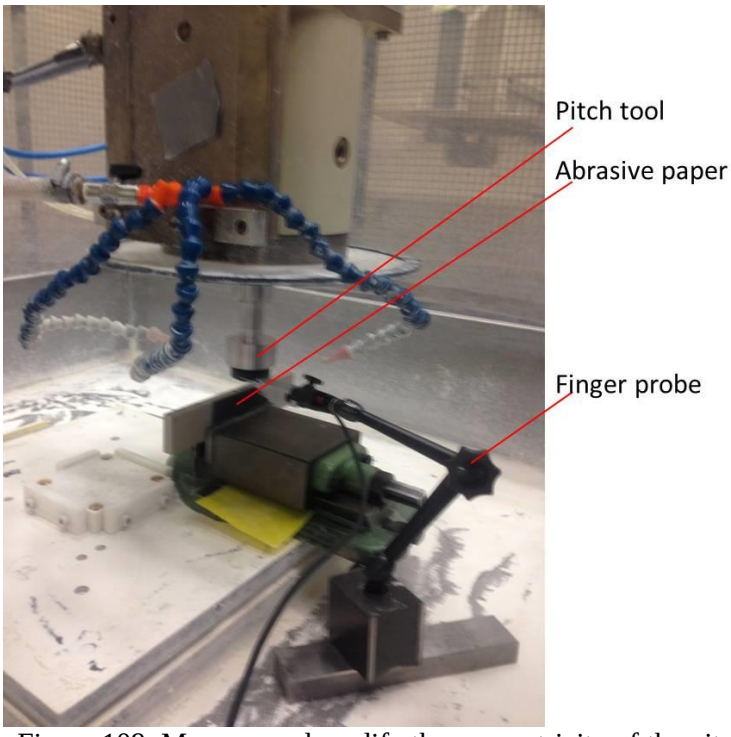

Figure 109: Measure and modify the concentricity of the pitch tool

The pitch tool shook badly when the concentricity and the precision of the tool were in a bad condition which would affect the polishing result. It is critical to modify the concentricity of the rotating pitch tool using an abrasive paper glued on a fixed plate and then check that the value of concentricity was within 200 μm using finger probe.

9.4Force of grooves polished by polyurethane tool

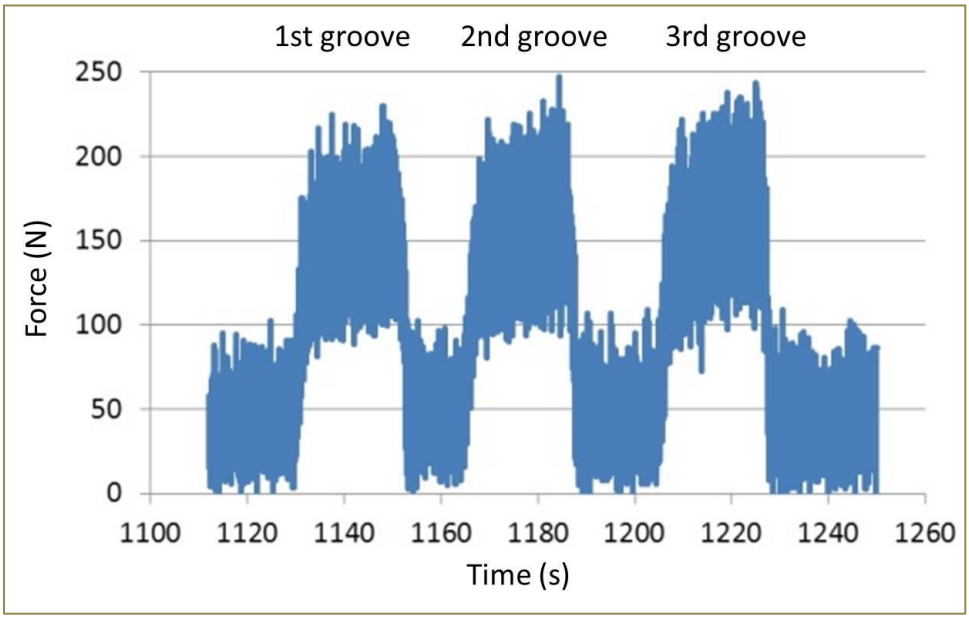

Figure 110: Force of polishing grooves - 5th run

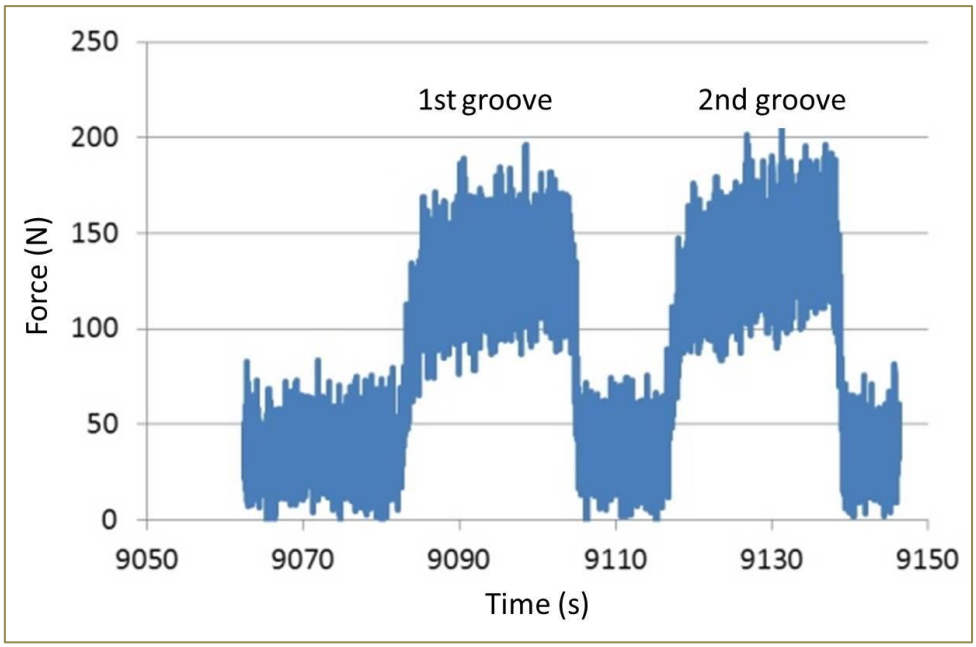

Figure 111: Force of polishing grooves - 11th run

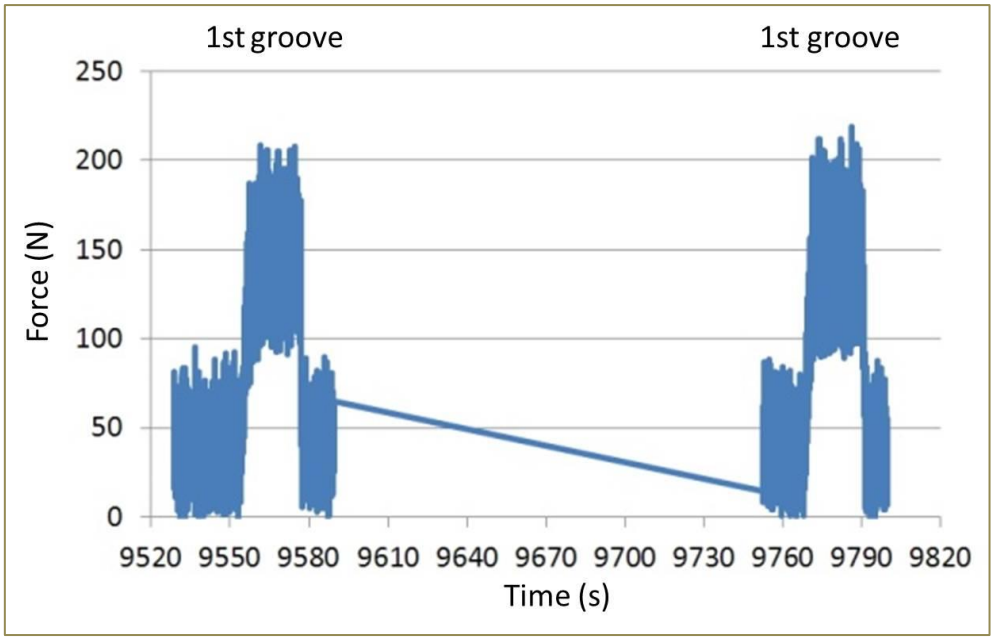

Figure 112: Force of polishing grooves - 16th and 20th runs

9.5 Edge effects of polished grooves

Table 33: Form accuracy of the grooves

P_t(μm) / mm	10 runs	15 runs	20 runs
2	5.9	8.9	11.7
5	5.9	8.8	11.1
8	5.6	8.4	10.3
11	5.6	8.3	10.0
14	5.6	8.3	10.0
30	5.6	8.7	9.9
50	5.4	8.0	10.3
70	4.9	7.9	10.4
86	4.4	6.5	11.7
89	4.1	6.3	10.5
92	3.8	6.1	8.7
95	3.7	6.0	8.3
98	4.2	6.8	10.5

9.6 Measurement of 100mm lapped sample before and after polishing

Table 34: Measurement result of lapped sample

Measurement direction	Pt (µm)	Ra (nm)
1	2.5685	238.3
2	2.3932	235.4
3	2.5462	236.0
4	2.2418	240.3

Table 35: Measurement after 1st run of robot polishing

Measurement direction	Pt (µm)	Ra (µm)
1	2.9615	0.0056
2	3.2260	0.0075
3	3.2318	0.0059
4	3.2042	0.0082
5	3.1746	0.0061
6	3.2382	0.0080
7	3.1708	0.0082

Table 36: Measurement after 7th run of robot polishing

Measurement direction	Pt (µm)	Ra (µm)
1	4.7452	0.0056
2	2.5996	0.0069
3	5.0908	0.0058
4	2.6211	0.0073
5	5.1420	0.0059
6	2.4899	0.0072
7	2.5621	0.0074

9.7 Measurement of 100mm ground samples before and after polishing

Table 37: Measurement result of ground sample- side 1

Measurement direction	P_t (µm)	R_a (µm)
1	1.7260	0.1115
2	2.2509	0.0731
3	2.0496	0.1092
4	2.7196	0.1129
5	1.4003	0.1074
6	2.9603	0.1092

Table 38: Measurement result of ground sample-side 2

Measurement direction	P_t (µm)	R_a (µm)
1	1.2657	0.0742
2	1.2086	0.0537
3	0.7968	0.0748
4	1.2380	0.0614
5	1.1146	0.0725
6	0.8894	0.0565

Table 39: Measurement result of ground sample after 6 runs robot polishing-side 1

Measurement direction	P_t (µm)	R_a (µm)
1	2.6241	0.0053
2	5.4609	0.0092
3	4.0107	0.0058
4	4.1453	0.0077
5	3.0533	0.0061
6	3.6005	0.0079

Table 40: Measurement result of ground sample after 6 runs robot polishing-side 2

Measurement direction	P_t (µm)	R_a (µm)
1	3.1413	0.0040
2	4.2507	0.0044
3	2.7745	0.0045
4	1.9784	0.0043
5	2.1200	0.0044
6	1.8500	0.0044

9.8 Measurement of 400mm ground sample before and after polishing

Table 41: Form accuracy and roughness of each measurement direction of 400mm square part

Measurement direction	Ground surface		4 runs robot polishing		9 runs robot polishing	
	P_t (µm)	R_a (µm)	P_t (µm)	R_a (µm)	P_t (µm)	R_a (µm)
0-2	3.5108	0.1735	3.3964	0.0049	3.1350	0.0039
1-3	2.6564	0.1857	1.5576	0.0054	1.0394	0.0044
2-6	1.4193	0.1920	1.2090	0.0036	3.2175	0.0031
0-12	1.6315	0.1650	3.4132	0.0052	3.8734	0.0048
11-13	1.4818	0.1774	2.3203	0.0058	2.7904	0.0050
12-16	1.8050	0.1914	2.9637	0.0039	3.3025	0.0035
0-22	3.8987	0.1652	2.8150	0.0039	2.3227	0.0053
21-23	1.3454	0.1771	0.8324	0.0042	1.5607	0.0057
22-26	2.8680	0.2038	1.7029	0.0045	1.8112	0.0034
0-32	3.2719	0.1720	2.2105	0.0046	1.9347	0.0055
31-33	1.6538	0.1894	1.3828	0.0052	3.1000	0.0056
32-36	1.3781	0.1886	6.9280	0.0034	3.3910	0.0035
0-42	4.3404	0.1664	1.5283	0.0056	3.3163	0.0045
41-43	1.6675	0.1869	1.2092	0.0054	1.7093	0.0048
42-44	1.2543	0.1976	1.0137	0.0042	1.5687	0.0032
0-46	3.6046	0.1669	1.0597	0.0056	3.5222	0.0049
45-47	2.0006	0.1974	3.6027	0.0062	2.3066	0.0053
46-48	1.3969	0.1935	1.2826	0.0040	2.4451	0.0036
0-50	3.5019	0.1746	2.3543	0.0045	1.5184	0.0054
49-51	1.2525	0.1915	1.8403	0.0046	3.1376	0.0058

50-52	1.1887	0.1909	2.5026	0.0034	4.6504	0.0037
0-54	3.4498	0.1665	2.5651	0.0050	2.0250	0.0053
53-55	1.2183	0.1900	1.1027	0.0056	2.0088	0.0058
54-56	1.2991	0.1966	2.2731	0.0035	3.9492	0.0038
4-5	2.8966	0.2353	3.7633	0.0053	4.8558	0.0058
14-15	1.0251	0.2238	2.6378	0.0061	6.6976	0.0070
24-25	2.3543	0.2327	4.2457	0.0059	4.8853	0.0051
34-35	2.0319	0.2280	2.4286	0.0046	2.8656	0.0053
7-8	0.7688	0.1924	2.6510	0.0030	3.4346	0.0025
9-10	1.1660	0.1832	1.3727	0.0030	3.5036	0.0025
17-18	0.9150	0.1965	1.7593	0.0031	2.8459	0.0027
19-20	0.9672	0.1832	1.7438	0.0029	2.5049	0.0026
27-28	0.9429	0.1969	3.6321	0.0024	3.3742	0.0028
29-30	1.0698	0.1827	1.6454	0.0024	2.7860	0.0027
37-38	0.7257	0.1911	7.6908	0.0028	2.5079	0.0028
39-40	0.8468	0.1836	4.6971	0.0039	2.4249	0.0027

9.9 Fringes obtained using the Zygo interferometer - 400mm square part

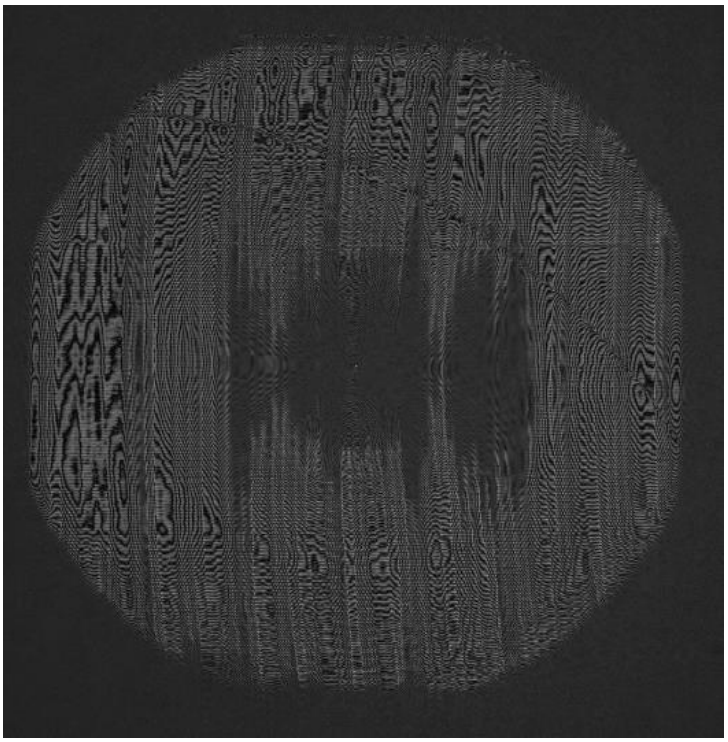

Figure 113: Fringes observed using the Zygo interferometer optical tower